THE GEOLOGICAL SOCIETY
OF AMERICA®

Formation of the crater suevite sequence from the Chicxulub peak ring: A petrographic, geochemical, and sedimentological characterization

Pim Kaskes[1,2,†], Sietze J. de Graaff[1,2,§], Jean-Guillaume Feignon[3,§], Thomas Déhais[1,2,§], Steven Goderis[1,§], Ludovic Ferrière[4,§], Christian Koeberl[3,§], Jan Smit[5,§], Axel Wittmann[6,§], Sean P.S. Gulick[7,8,§], Vinciane Debaille[2,§], Nadine Mattielli[2,§], and Philippe Claeys[1,§]

[1]*Research Unit: Analytical, Environmental & Geo-Chemistry, Department of Chemistry, Vrije Universiteit Brussel, AMGC-WE-VUB, Pleinlaan 2, 1050 Brussels, Belgium*
[2]*Laboratoire G-Time, Université Libre de Bruxelles, ULB, Av. F.D. Roosevelt 50, 1050 Brussels, Belgium*
[3]*Department of Lithospheric Research, University of Vienna, Althanstrasse 14, A-1090 Vienna, Austria*
[4]*Natural History Museum, Burgring 7, A-1010 Vienna, Austria*
[5]*Department of Earth Sciences, Vrije Universiteit Amsterdam, De Boelelaan 1085, 1081 HV Amsterdam, Netherlands*
[6]*Eyring Materials Center, Arizona State University, Tempe, Arizona 85287, USA*
[7]*Institute for Geophysics & Department of Geological Sciences, Jackson School of Geosciences, University of Texas at Austin, Austin, Texas 78758, USA*
[8]*Center for Planetary Systems Habitability, University of Texas at Austin, Austin, Texas 78712, USA*

ABSTRACT

This study presents a new classification of a ~100-m-thick crater suevite sequence in the recent International Ocean Discovery Program (IODP)-International Continental Scientific Drilling Program (ICDP) Expedition 364 Hole M0077A drill core to better understand the formation of suevite on top of the Chicxulub peak ring. We provide an extensive data set for this succession that consists of whole-rock major and trace element compositional data (n = 212) and petrographic data supported by digital image analysis. The suevite sequence is subdivided into three units that are distinct in their petrography, geochemistry, and sedimentology, from base to top: the ~5.6-m-thick non-graded suevite unit, the ~89-m-thick graded suevite unit, and the ~3.5-m-thick bedded suevite unit. All of these suevite units have isolated Cretaceous planktic foraminifera within their clastic groundmass, which suggests that marine processes were responsible for the deposition of the entire M0077A suevite sequence. The most likely scenario describes that the first ocean water that reached the northern peak ring region entered through a N-NE gap in the Chicxulub outer rim. We estimate that this ocean water arrived at Site M0077 within 30 minutes after the impact and was relatively poor in rock debris. This water caused intense quench fragmentation when it interacted with the underlying hot impact melt rock, and this resulted in the emplacement of the ~5.6-m-thick hyaloclastite-like, non-graded suevite unit. In the following hours, the impact structure was flooded by an ocean resurge rich in rock debris, which caused the phreatomagmatic processes to stop and the ~89-m-thick graded suevite unit to be deposited. We interpret that after the energy of the resurge slowly dissipated, oscillating seiche waves took over the sedimentary regime and formed the ~3.5-m-thick bedded suevite unit. The final stages of the formation of the impactite sequence (estimated to be <20 years after impact) were dominated by resuspension and slow atmospheric settling, including the final deposition of Chicxulub impactor debris. Cumulatively, the Site M0077 suevite sequence from the Chicxulub impact site preserved a high-resolution record that provides an unprecedented window for unravelling the dynamics and timing of proximal marine cratering processes in the direct aftermath of a large impact event.

INTRODUCTION

The Chicxulub impact event on the northern Yucatán Peninsula in México occurred ~66 million years ago and marks one of the most catastrophic events in the history of life on Earth (e.g., Smit and Hertogen, 1980; Alvarez et al., 1980; Hildebrand et al., 1991; Schulte et al., 2010; Renne et al., 2013). The global aftermath of this hypervelocity impact was characterized by rapid climate change leading to the Cretaceous-Paleogene (K-Pg) boundary mass extinction (e.g., Smit and Hertogen, 1980; Alvarez et al., 1980; Schulte et al., 2010). It has been hypothesized that the ejection of fractured, molten, and vaporized Yucatán target rock, together with impactor debris, into the stratosphere triggered severe environmental stress (e.g., Kring, 2007; Artemieva and Morgan, 2017; Hull et al., 2020). To better understand how this enormous impact-induced energy release disrupted the global Earth system ~66 million years ago, it is crucial to gain insights into the nature and composition of the different source materials from the crater region. This can be established by studying in detail the petrology, geochemistry, and emplacement mechanisms of the sequence of rocks deposited by the impact that is found today within and in close proximity to the ~200-km-diameter-sized Chicxulub impact structure (i.e., proximal impactites).

Suevite is a common type of proximal impactite found within or around impact structures that records important information about which part of the target stratigraphy underwent shock metamorphism, brecciation, melting, and vaporization as a result of the impact. Suevite is defined as a polymict impact breccia with a particulate or clastic matrix containing lithic and

---

Pim Kaskes http://orcid.org/0000-0002-2605-6366

[†]Corresponding author: pim.kaskes@vub.be.

[§]sietze.de.graaff@vub.be; jean-guillaume.feignon@univie.ac.at; thomas.dehais@vub.be; steven.goderis@vub.be; ludovic.ferriere@nhm-wien.ac.at; christian.koeberl@univie.ac.at; j.smit@vu.nl; axel.wittmann@asu.edu; sean@ig.utexas.edu; vinciane.debaille@ulb.be; nadine.mattielli@ulb.be; phclaeys@vub.be.

GSA Bulletin; https://doi.org/10.1130/B36020.1; 16 figures; 1 table; 1 supplemental file.

© 2021 The Authors. Gold Open Access:
This paper is published under the terms of the CC-BY license.

Downloaded from http://pubs.geoscienceworld.org/gsa/gsabulletin/article-pdf/doi/10.1130/B36020.1/5365526/b36020.pdf
by Arizona State University user

mineral clasts in all stages of shock metamorphism including cogenetic melt particles, which are in a glassy or crystallized state (Stöffler and Grieve, 2007). Some authors have linked the term "suevite" to specific formational processes (e.g., Grieve et al., 2010; Osinski et al., 2016), but in this manuscript the term suevite remains purely descriptive and represents an impact melt bearing polymict breccia with a clastic groundmass. Based on extensive research at the Ries crater in Germany, which is the type locality for suevite, suevite occurs in three different geological settings with respect to a crater structure. These are defined as crater suevite (deposited inside the crater rim), outer suevite (outside of the crater rim as part of the ejecta blanket), and dike suevite (within parautochthonous crater basement or ejected crystalline megablocks) (Stöffler, 1977; Stöffler and Grieve, 2007; Stöffler et al., 2013).

Crater suevite represents, in general, the upper part of a proximal impactite sequence and thereby records the evolution of the filling of a crater in the direct aftermath of the impact (French, 1998; Stöffler et al., 2013). However, the general emplacement mechanisms of suevite remain the topic of considerable debate, as they likely strongly differ from crater to crater due to variability in target rock and paleoenvironment (e.g., a marine versus a continental target), can vary laterally and vertically throughout the buildup of an impactite sequence, and are a complex product of magmatic, (shock) metamorphic, and sedimentary processes (e.g., Ormö et al., 2007; Stöffler et al., 2013). In this study, we aim to unravel the formation of crater suevite from the Chicxulub impact structure by investigating in detail the petrography, geochemistry, and sedimentology of unique drill core material collected by the recent Expedition 364 (Morgan et al., 2016, 2017), organized under the auspices of the International Ocean Discovery Program (IODP) and International Continental Scientific Drilling Program (ICDP). In 2016, during this expedition, the offshore part of the Chicxulub peak ring (Fig. 1) was sampled, and a continuous ~100-m-thick sequence of crater suevite, overlying granitoid basement, and impact melt rock (Fig. 2A; Morgan et al., 2016) was obtained. Here, we present whole rock major and trace element compositional data (n = 212), high-resolution major element mapping results, and petrographic data supported by quantitative digital image analysis of this suevite core material. This extensive data set results in a revised classification of the suevite peak ring sequence (Figs. 2B–2C) and offers new insights into the complex infill history of the Chicxulub impact structure in the first moments after the impact.

GEOLOGICAL SETTING

Depositional scenarios of suevite are highly dependent on the characteristics of the target stratigraphy, the presence or absence of (sea) water, and impactor-specific conditions (including impactor size, impact angle, and resulting energy; e.g., Artemieva et al., 2013). For Chicxulub, the impactor is constrained as a CM

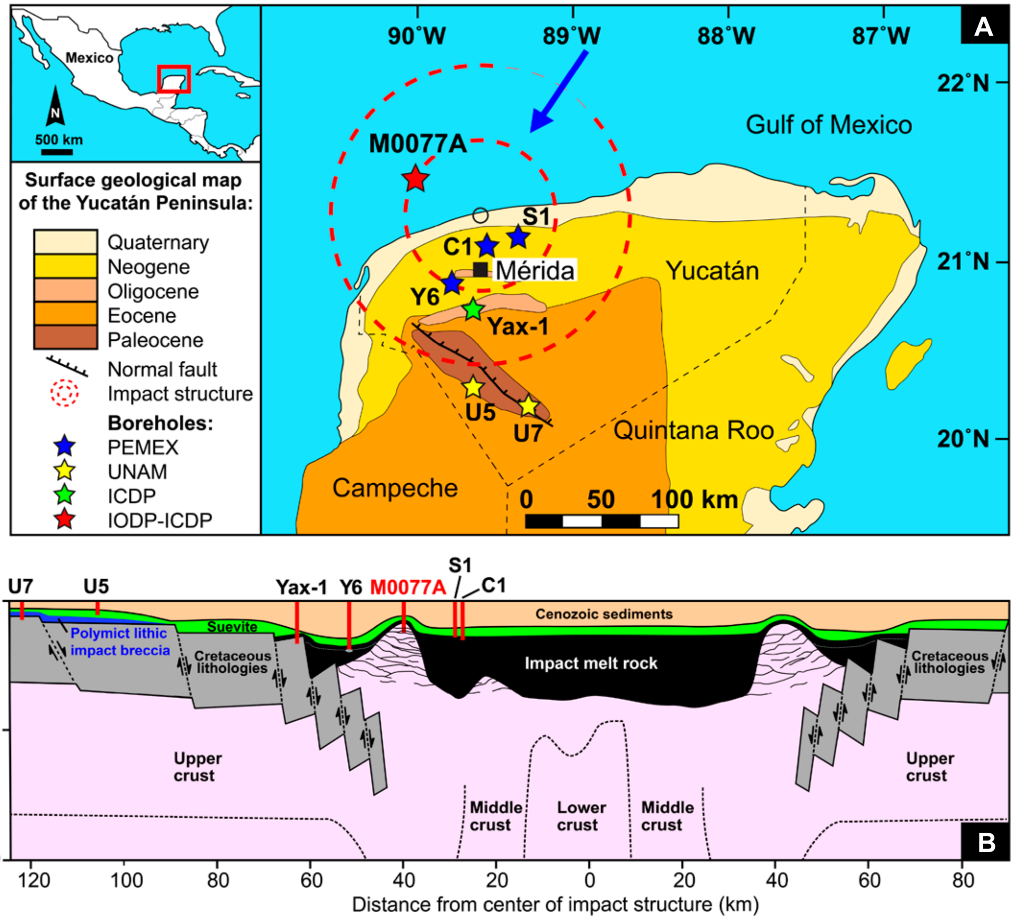

Figure 1. (A) Simplified surface geological map of the northern part of the Yucatán Peninsula in México with the location of the buried Chicxulub impact structure and the drill cores that collected impact melt-bearing impactites (modified from Rebolledo-Vieyra and Urrutia-Fucugauchi, 2004; and Kring, 2005). The red circles indicate the position of the outer rim and peak ring of the Chicxulub impact structure. The blue arrow indicates a gap in the outer rim of the Chicxulub structure and shows a potential pathway for water re-entering the crater after formation (Gulick et al., 2008, 2019). (B) Schematic geological cross section through the Chicxulub impact structure with the interpreted sequence of crustal rock, impact melt rock, suevite (in green), polymict lithic impact breccia (in blue), and post-impact Cenozoic sediments (modified from Sharpton et al., 1996; Claeys, 2006; Gulick et al., 2008; Vermeesch and Morgan, 2008; and de Graaff et al., 2021). PEMEX—Petróleos Mexicanos; UNAM—Universidad Nacional Autónoma de México; ICDP—International Continental Scientific Drilling Program; IODP–ICDP—International Ocean Discovery Program–International Continental Scientific Drilling Program.

Downloaded from http://pubs.geoscienceworld.org/gsa/gsabulletin/article-pdf/doi/10.1130/B36020.1/5365526/b36020.pdf
by Arizona State University user

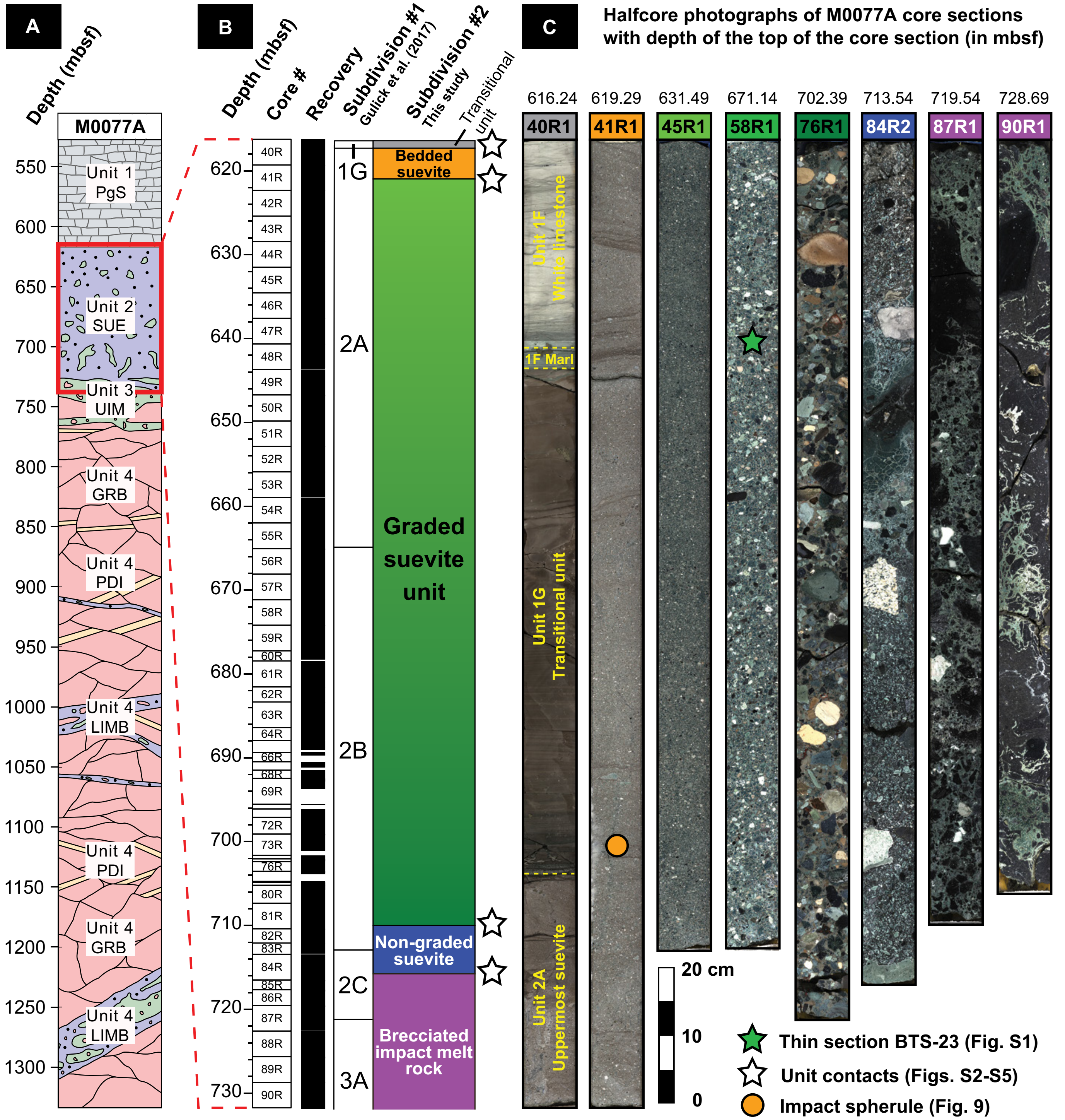

Figure 2. (A) Overview of the International Ocean Discovery Program (IODP) and International Continental Scientific Drilling Program (ICDP) Expedition 364 M0077A drill core with the main four lithological units from Morgan et al. (2016, 2017). PgS—Paleogene marine sediments; SUE—suevite; UIM—upper impact melt rock unit; LIMB—lower impact melt rock-bearing unit (following de Graaff et al., 2021); GRB—pre-impact granitoid basement; PDI—pre-impact dikes. (B) Stratigraphy of the impactite sequence between cores 40 and 90 (~616.5–732 m below sea floor [mbsf]) with the degree of core recovery and the initial subdivision of the sequence by Gulick et al. (2017) (Unit 1G; 2A-2C; 3A). Adjacent, a new subdivision of this sequence is shown with three suevite units, based on the extensive petrographic, geochemical, and sedimentological examination of this study. The unit contacts, indicated here with white asterisks, are shown in more detail in Figs. S2–S5 (see footnote 1). (C) Composite halfcore photographs with representative core sections of the suevite and impact melt rock units investigated. In addition, the stratigraphic positions of thin section BTS-23 (selected for digital image analysis; Fig. S1 [see footnote 1]), from the middle part of the graded suevite unit, and a Chicxulub impact spherule (Fig. 9) within the bedded suevite unit are highlighted.

Downloaded from http://pubs.geoscienceworld.org/gsa/gsabulletin/article-pdf/doi/10.1130/B36020.1/5365526/b36020.pdf
by Arizona State University user

or CO type carbonaceous chondrite (Shukolyukov and Lugmair, 1998; Trinquier et al., 2006; Quitté et al., 2007; Goderis et al., 2013), and the most recent estimation calls for a projectile ~17 km in diameter that impacted at a steep angle of 45–60° from the northeast (Collins et al., 2020). The impact on Yucatán took place in a marine setting with variable water depths. At the Chicxulub impact site, the average water depth has been estimated to have been 600 m (Gulick et al., 2008), but significant deepening toward the north down to ~2 km (Gulick et al., 2008) and shallower marine conditions toward the south of the impact site have been proposed (Ocampo et al., 1996; Pope et al., 2005). The target stratigraphy consisted of a ~3-km-thick Mesozoic carbonate-evaporite platform overlying Paleozoic and Precambrian crystalline and metamorphic basement (López-Ramos, 1975; Morgan et al., 2016; Zhao et al., 2020).

However, detailed knowledge about the Yucatán target stratigraphy is hampered by the rapid burial of the Chicxulub impact structure and the surrounding region by a thick succession of up to ~1 km of Cenozoic sediments (López-Ramos, 1975). Consequently, there is an overall absence of exposures with pre-impact sedimentary and crystalline lithologies on the Yucatán Peninsula. The most proximal outcrops in which pre-impact material is preserved (including carbonate clasts and shocked quartz) are the K-Pg ejecta-bearing deposits of the Albion Formation on top of the Barton Creek Formation dolomite near the border of the Mexican province of Quintana Roo and northern Belize, which is ~350 km SE of the crater center (Ocampo et al., 1996; Pope et al., 2005). Outcrops of crystalline basement that are potentially linked to the Maya Block underneath Yucatán are situated even further away in the Chiapas Massif Complex near the México-Guatemala border, which is ~700 km SW of the crater center (Ortega-Gutiérrez et al., 2018). In addition, the Chicxulub structure has only been drilled on a few occasions (Hildebrand et al., 1991; Dressler et al., 2003; Kring et al., 2017), and the limited material recovered during these drillings makes it challenging to accurately document the impactites and basement within an impact structure of this size.

A total of only six drill cores are currently available that have preserved and sampled Chicxulub suevite (Fig. 1). In the 1950s and 1960s, Petróleos Mexicanos (PEMEX) first drilled three onshore exploration wells in the Chicxulub structure (Chicxulub 1: C1, Yucatán 6: Y6, Sacapuc 1: S1), and suevitic material was only collected and preserved from the latter two cores (López-Ramos, 1975; Ward et al., 1995; Sharpton et al., 1996). The total thickness of the suevite succession in the Y6 core, located ~50 km SW of the crater center on the inner edge of the annular trough adjacent to the peak ring, is estimated to be 250 m (Sharpton et al., 1996). Based on a limited and non-continuous sample set, Claeys et al. (2003) subdivided the suevite in the Y6 core into three units. The lowermost unit was interpreted to be early fall-back material or ground-surged material that formed during the collapse of the transient cavity. The middle suevite was interpreted as a typical fall-back suevite, whereas the upper unit was considered to represent late fall-back material that settled through the water column or was intensively reworked after crater inundation (Claeys et al., 2003). The S1 core, obtained ~30 km SE of the crater center, is much less characterized, and only a single suevite sample from this core (S1-N18 at 1365–1368 m depth) has been described in the literature (Sharpton et al., 1996). This sample displayed many petrographic similarities to N14 in Y6 (Sharpton et al., 1996), which was classified as "middle suevite" by Claeys et al. (2003).

In the mid-1990s, the Universidad Nacional Autónoma de México (UNAM) drilled a series of shallow onshore wells in the ejecta blanket outside of the Chicxulub structure and penetrated units of impact melt-free to impact melt-rich polymict impact breccia (Urrutia-Fucugauchi et al., 1996, 2014). In the UNAM-5 (U5) core, which was located 105 km from the crater center, a 172-m-thick suevite unit was identified with abundant basement clasts and silicate melt fragments. At 126 km from the crater center in the UNAM-7 (U7) core, a 126-m-thick suevite sequence, interpreted to have settled out of the turbulent ejecta plume, was deposited on top of a ballistically emplaced "Bunte Breccia-like" lithic breccia deposit rich in evaporite clasts but lacking melt fragments (Rebolledo-Vieyra et al., 2000).

In 2002, ICDP carried out the onshore Yaxcopoil-1 (Yax-1) drilling 60 km SW of the crater center and drilled into shallow slump blocks beneath the outer annular trough of the Chicxulub structure (Dressler et al., 2003; Urrutia-Fucugauchi et al., 2004). This drill core recovered a ~100 m succession of suevite-like impactites, which were subdivided into six units (Stöffler et al., 2004): upper and lower sorted suevite, upper suevite, middle suevite, brecciated impact melt rock, and lower suevite. How these units formed remains debated, but most authors agree with a model that started with ground surging at the base of the ejecta curtain, which was followed by continued collapse of the ejecta plume and aquatic reworking at the top (Dressler et al., 2004; Goto et al., 2004; Kring et al., 2004; Stöffler et al., 2004; Tuchscherer et al., 2004; Wittmann et al., 2007). The relatively thin impactite sequence in the Yax-1 core is underlain by slightly tilted Cretaceous carbonate-anhydrite megablocks (Fig. 1B; Dressler et al., 2003; Kenkmann et al., 2004; Belza et al., 2012), which indicate pronounced slumping (i.e., terrace zone formation) at the inner rim into the annular trough. Due to this slumping, questions remain about the nature and true thickness of the impactite sequence and the dynamic formation of the Chicxulub impact structure (Kring et al., 2017).

A joint effort by the IODP and ICDP resulted in the successful Expedition 364 drilling in April-May 2016 on the Chicxulub peak ring, which is ~40 km NW of the crater center at Site M0077 in the Gulf of Mexico (Fig. 1; 21.45°N, 89.95°W) (Morgan et al., 2016). This drilling expedition was primarily aimed at investigating the nature and composition of peak ring rocks, to understand the formational mechanisms of peak rings, to constrain how rocks are weakened during impact events, to study the post-impact hydrothermal circulation, and to obtain a better understanding of the biotic and climatic consequences of the impact (Morgan et al., 2017). From a depth of 505.7–1334.7 m below sea floor (mbsf), an 829-m-long drill core was extracted from Hole M0077A (hereafter named M0077A), which is situated on a depression on the northern peak ring (Morgan et al., 2016). Subdivided into four lithostratigraphic units (Morgan et al., 2017), this drill core consists of a 112-m-thick interval of Paleogene hemipelagic and pelagic sediments (Unit 1A-G), a 104-m-thick unit of suevite (Unit 2A-C), a 25-m-thick body of upper impact melt rock (Unit 3A-B), and 588 m of granitoid basement (Unit 4) intruded with (pre-) impact dikes and intercalated with a lower impact melt rock-bearing unit (LIMB according to de Graaff et al., 2021) (Fig. 2). Compared to previous Chicxulub drill cores, IODP-ICDP Expedition 364 recovered a continuous sequence of proximal impactites and—in contrast to solely granitoid clasts in breccia units in other cores—the first continuous section of uplifted granitoid basement from the Chicxulub impact structure (Feignon et al., 2020). The M0077A suevite succession from Unit 2 yields an intact contact with both the underlying impact melt body (Unit 3A) as well as the transitional interval (Unit 1G) above, which contains the K-Pg platinum group element anomaly (Goderis et al., 2021). Cumulatively, this sequence represents the thickest (~130 m) and most proximal K-Pg boundary section obtained to date that records the immediate aftermath of the Chicxulub impact event with unprecedented detail and resolution (Gulick et al., 2019).

The M0077A suevite sequence from Unit 2 has already been the topic of previous works,

Downloaded from http://pubs.geoscienceworld.org/gsa/gsabulletin/article-pdf/doi/10.1130/B36020.1/5365526/b36020.pdf
by Arizona State University user

which focused primarily on geophysical properties (Christeson et al., 2018) and the description of macroscopic features of the unit, including observations of hydrothermal features (Kring et al., 2020) and digital image analysis (Osinski et al., 2020), geological line logging (Gulick et al., 2019; Ormö et al., 2021), and supervised machine learning clast analysis of halfcore photographs (Gulick et al., 2019). These studies highlighted the high porosity of Unit 2, the high degree of hydrothermal alteration, and the moderately to well-sorted nature of the suevite. The sorting of these suevites was interpreted to have been caused by melt-water interactions similar to explosive phreatomagmatic processes (Gulick et al., 2019; Osinski et al., 2020) and by a powerful resurge back into the crater (Gulick et al., 2019; Ormö et al., 2021). The bulk geochemistry of the M0077A suevite sequence and the compositional variability of the different suevite components (clast types and groundmass) throughout the succession remain relatively poorly studied to date (see preliminary work compiled by Gulick et al., 2017) and are therefore a main focus of this study. By integrating compositional, microtextural, and sedimentological data to constrain the variability of the target lithologies involved, we aim to classify, characterize, and resolve the complex formation of the M0077A suevite sequence.

SAMPLES AND ANALYTICAL METHODS

Rock samples (~20 cm^3) of the M0077A suevite sequence were collected during three different sampling campaigns: the post-cruise sampling party at the MARUM-Bremen Core Repository in Germany (September 2016), an additional sampling campaign at MARUM (December 2017), and a final sampling campaign at the College Station-Texas Core Repository in the USA (October 2018). Samples were pre-selected based on the halfcore photographs (available at http://publications.iodp.org/proceedings/364/364title.html; accessed May 2021), an initial classification by Gulick et al. (2017), and an overview of clast identifications based on Ormö et al. (2021). We performed a high-resolution, multi-proxy analysis of samples from Unit 2 and incorporated samples of the overlying Unit 1G (transitional unit) and the underlying impact melt rock (Unit 3A). The sample set includes 170 samples of representative bulk suevite material extended with material from the underlying and overlying units at a high spatial resolution of, on average, 0.7 m over the 115.5-m-thick interval (cores 40.1–90.3, ~616.5–732 mbsf, with a maximum stratigraphic distance of 3.4 m between two samples) with 32 samples of specific suevite clast types. Supplementary Table S1[1] lists the samples (for both bulk assemblages and specific clast types) characterized in this study and the various analytical techniques that were carried out on each of these. Sample nomenclature used in this study corresponds to Core#_Section#_Top(cm)_Bottom(cm) to highlight the exact interval sampled, where the centimeter notation indicates the distance from the top of the corresponding core section.

Optical and Scanning Electron Microscopy

In total, 135 polished thin sections were prepared, of which 103 represent bulk assemblages and 32 represent individual suevite clast types. All thin sections were examined under plane-polarized light (PPL) and cross-polarized light (XPL) using a Zeiss (Carl Zeiss GmbH, Jena, Germany) Axioscope 5 TL/RL polarizing microscope equipped with a Zeiss Axiocam 208 camera at Vrije Universiteit Brussel, Belgium (VUB). Special attention was paid to the microtextures of various clast and groundmass types, the abundance and type of (micro)fossils, possible shock metamorphic features, such as planar deformation features (PDFs) in quartz grains, and reaction rims around specific clasts. Micrometer-sized features that could not easily be identified using basic optical microscopy were visualized by means of backscattered electron (BSE) images using a JEOL JSM-IT300 (JEOL Ltd., Tokyo, Japan) scanning electron microscope equipped with an energy dispersive X-ray spectrometer (SEM-EDS) at VUB. The petrographic observations were verified by comparing the results with an existing bulk powder X-ray diffraction data set from Gulick et al. (2017), which provided percentages of mineral groups (calcite, quartz, feldspar, zeolite, smectite, mica, pyroxene, and other minerals) present throughout the sequence.

Major Element Mapping and Spot Analysis

Qualitative to semiquantitative EDS mapping of small areas (up to 2 × 2 mm in size) of a limited number of major elements (Na, Mg, Al, Si, Cl, K, Ca, Ti, Mn, and Fe) was also carried out on a selection of thin sections at the VUB. The EDS mapping was performed on a JEOL JSM-IT300 with an acceleration voltage of 15.0 kV, a resolution of 768 × 1024 pixels, and a pixel dwell time of 2000–5000 μs. Element maps were created with the software AZtec (Oxford Instruments Nanotechnology Tools Ltd., Abingdon, UK).

The major element oxide (Na_2O, MgO, Al_2O_3, SiO_2, K_2O, CaO, TiO_2, Cr_2O_3, MnO, and FeO) composition of the suevite groundmass was determined using quantitative wavelength dispersive X-ray spectrometry (WDS) analyses on a JEOL Hyperprobe JXA 8530F field-emission gun electron microprobe analyzer (EMPA) at the Central Research Laboratories of the Natural History Museum in Vienna, Austria. The groundmass in five suevite samples, covering the entire stratigraphic range, was analyzed using a defocused beam on 100-μm-diameter spots. Per sample, 10 EMPA points were analyzed to obtain a representative data set for the groundmass composition. Operating conditions included an accelerating voltage of 15.0 kV, a beam current of 20 nA, and a counting time of 10s on peak and 5s on background positions for all element Kα lines. The total uncertainty associated with the EMPA major element analysis is estimated to be on the order of 5%–15% relative standard deviation (RSD) (Goderis et al., 2020). To allow comparison of the EMPA data with those of other techniques, all results were normalized to 100% to exclude volatiles, and FeO was recalculated as total ferric iron ($Fe_2O_3^T$).

To cover larger and more representative sample areas of suevite assemblages, we performed energy-dispersive micro-X-ray fluorescence (μXRF) scanning of 133 polished thin sections and 185 polished thick sections. For this, an M4 Tornado benchtop μXRF surface scanner (Bruker nano GmbH, Berlin, Germany) equipped with a Rh tube as the X-ray source and two XFlash 430 Silicon Drift detectors was used at VUB. This technique makes it possible to obtain high-resolution elemental distributions by scanning flat sample surfaces in a rapid, non-destructive, and cost-efficient way (de Winter and Claeys, 2017; Kaskes et al., 2021). The μXRF mapping was performed using both detectors at maximized X-ray source energy settings (50 kV and 600 μA, without any filter). The measurements were carried out under near vacuum conditions (20 mbar) with a spot size and spatial resolution of 25 μm and an integration time of 1 ms per pixel. This approach resulted in qualitative multi-element maps and semiquantitative single-element heatmaps (Kaskes et al., 2021), in which the highest X-ray intensity for the elements' Kα-line corresponds to the pixel with the highest possible RGB value (i.e., 255).

In addition, the bulk and clast-specific major element compositions of polished thick sections was quantified using the Bruker M4 software by extracting spectra based on polygons of desired subareas in the μXRF maps. After manual

---

[1] Supplemental Material: Figures S1–S7 and Tables S1 and S2. Please visit https://doi.org/10.1130/GSAB.S.14699964 to access the supplemental material, and contact editing@geosociety.org with any questions.

Downloaded from http://pubs.geoscienceworld.org/gsa/gsabulletin/article-pdf/doi/10.1130/B36020.1/5365526/b36020.pdf
by Arizona State University user

inspection of the spectra and assigning all visible peaks to the correct elements, the Standardless Fundamental Parameter method (Sherman, 1955) was applied to quantify a normalized bulk composition. This quantification technique was employed because of the large heterogeneities within the suevite samples in terms of distinct phases such as carbonate clasts and felsic or mafic silicate clasts. To validate this approach, the bulk concentrations were compared with bulk powder XRF (e.g., from Gulick et al., 2017) and inductively coupled plasma-optical emission mass spectrometry (ICP-OES) measurements from the same intervals. Based on a comparison with these bulk powder techniques, as outlined in Kaskes et al. (2021), the concentrations of most major element oxides (Na_2O, MgO, Al_2O_3, SiO_2, K_2O, and CaO) of thick sections of these heterogeneous impactites are accurate within 10% RSD. Additional repeated μXRF measurements of U.S. Geological Survey reference material basalt glass BCR-2G resulted in a reproducibility for all reported major elements of <1%–10% RSD and for trace elements on the order of 2%–15% RSD (Kaskes et al., 2021).

Thin sections are not suitable for such a quantification due to their limited thickness of 30 μm, which generates secondary fluorescence from the underlying glass substrate because X-rays are not fully attenuated in the sample (Haschke, 2014; Kaskes et al., 2021). However, μXRF maps of thin sections are still useful to detect and visualize the distribution of major elements (Wouters et al., 2017; Kaskes et al., 2021). In this study, we use qualitative μXRF maps of Mg, Al, Si, S, K, Ca, Ti, Mn, and Fe, because they are, in general, linked to distinct phases in the suevite and can, therefore, aid in the petrographic interpretation and be used for digital image analysis.

Digital Image Analysis

Semi-automated digital image analysis methods have previously been used to quantitatively analyze and characterize, in a time-efficient manner, proximal impactites based on cut and polished hand specimens (Chanou et al., 2014) and scans or optical microphotographs of polished thin sections (Pittarello and Koeberl, 2013). These types of analyses produce quantitative petrographic parameters such as clast versus matrix ratios, degree of sorting, modal distributions of distinct mineral phases, particle parameters (e.g., orientation, length, width, area, perimeter), and shape parameters (e.g., roundness, sphericity, and aspect ratio) (Wittmann et al., 2007). These parameters are powerful proxies for obtaining a better understanding of the mode of transport, hydrodynamic behavior, and deposition of the different suevite components.

In this study, the Image Analysis Module in the Zeiss ZEN3.1 Pro software was used to segment, classify, and quantitatively characterize the different clast types within the suevite samples (Kaskes et al., 2021). We used μXRF element maps of five representative thin sections throughout the suevite stratigraphy for digital segmentation. This segmentation was done to allow verification of the petrographic clast identifications with compositional data and to overcome problems of misidentifications based on color, which can be caused by diagenetic and hydrothermal alteration instead of associations with true target lithology components. The image analysis workflow is visualized with thin section BTS-23 in Fig. S1 (see footnote 1). Firstly, RGB-colored μXRF maps of thin sections, occasionally edited in the M4 Bruker software to enhance RGB contrast, were imported into the software and scaled based on their resolution (25 μm per pixel). Secondly, a classification was made of the different clast types and the groundmass present in the sample. We mainly used Ca μXRF heatmaps (Fig. S1E) as a basis for the segmentation, as in those maps there is a large contrast between carbonate clasts (high in Ca content and high RGB values), groundmass (some Ca, intermediate RGB values) and non-carbonate clasts (little to no Ca and low RGB values) in these maps. Subsequent segmentation took place with automatic selection of phases in a designated sample frame on the μXRF map. This segmentation was based on maximum and minimum thresholding of RGB values (0–255) and with a minimum particle area threshold of 0.05 mm^2. We also applied the “fill holes” option to exclude secondary structures within—mainly—impact melt particles. Interactive manual segmentation was only carried out when the contrast between clast and groundmass or between different clasts was not high enough or when clasts consisted of multiple compositionally distinct mineral phases. After careful digital segmentation, a first map was produced for three components: carbonate clasts, non-carbonate clasts, and groundmass (Fig. S1F). Based on detailed petrography, the carbonate and non-carbonate clasts were manually regrouped into seven distinct groups (Fig. S1G), following the groups described in the Results section.

After this second segmentation step, an extensive clast-specific data set was produced. The image analysis software exports the following output measurements for each clast: *(filled) area* (mm^2), *convex area* (mm^2), *length of major and minor axis of the best-fit ellipse* (mm), *aspect ratio* (ratio between the major and minor ellipse axis length), *perimeter* (mm), *roundness* (a value 0–1 based on (4π area)/(convex perimeter)^2), *sphericity* (perfect circle equals 1), and *convexity* (convex perimeter/perimeter). It is also possible to select whether a particle at the edge of a sample touches the selected sample frame. This is useful to ensure that particles that are cut off by the outline of the sample are not incorporated in the shape parameter database, as their morphologies are incomplete and hence inaccurate. However, as these particles are still part of the investigated sample area, they are incorporated in the calculation of the modal abundances of classes and are also included in determining the degree of sorting using cumulative area and perimeter fractions (Chanou et al., 2014). Subsequently, the SUM-classes export function in the ZEN 3.1 Pro software provided the total count of the clasts of one particular group, the cumulative area percentage, and average values for the particle parameters stated above (Fig. S1H). Based on these parameters, the modal abundances of the different components were calculated with their main particle characteristics. Repeated processing of μXRF maps in the image analysis software resulted in uncertainties in the modal abundances of <10%, which was followed by verification of these modal abundances with a petrographic study of the associated thin section.

Bulk Major and Trace Element Analysis

Fifty-eight representative samples from the M0077A suevite sequence and adjoining units were selected for whole-rock, powder-based major and trace element analysis using facilities in two independent laboratories. Thirty-one samples were analyzed by means of ICP-OES and Inductively Coupled Plasma–Mass Spectrometry (ICP-MS), with sample preparation taking place in a Class 1000 clean laboratory, at the Laboratoire G-Time of the Université Libre de Bruxelles, Belgium (ULB). Twenty-seven samples were measured by means of glass bead-based X-ray fluorescence (bulk XRF) and instrumental neutron activation analysis (INAA) at the Department of Lithospheric Research at the University of Vienna, Austria. Before crushing, weathered surfaces, alteration veins, and large clasts (>1 cm in diameter) that could affect the average assemblage composition were carefully removed using a diamond board table saw. Samples were washed with Milli-Q water in an ultrasonic bath before subsamples of ~10 cm^3 were crushed using an agate mortar and pestle and powdered using a Fritsch Pulverisette-5 agate planetary ball mill at VUB or a vibratory disc mill Retsch RS200 at the University of Vienna.

Subsequent preparation of these homogenized powders and procedures for alkaline fusion based ICP-OES and ICP-MS analyses at ULB followed the methodology outlined in de Graaff et al. (2021). Repeated measurements of the U.S.

Downloaded from http://pubs.geoscienceworld.org/gsa/gsabulletin/article-pdf/doi/10.1130/B36020.1/5365526/b36020.pdf
by Arizona State University user

Geological Survey (USGS) reference material BHVO-2 (n = 18) and BCR-2 (n = 5) yielded a reproducibility for all reported major elements on the order of <1%–8% relative standard deviation (RSD) and for all reported trace elements on the order of <1%–10% RSD.

Glass bead-based bulk XRF analyses were carried out on an X-ray spectrometer PHILIPS PW2404 at the University of Vienna using a super-sharp end-window tube with a Rh-anode following the methodology outlined in Nagl and Mader (2019). For loss on ignition determination, powders (3 g) were heated to 1050 °C in a muffle furnace for a 3 h period and then weighed. The major element concentrations were determined using calibration curves established by reference materials SG-1A, TDB-1, BHVO-2, and JH-1 (Nagl and Mader, 2019). Accuracy and precision values (in wt%) were 0.6 for SiO_2 and Fe_2O_3, 0.3 for Al_2O_3, 0.2 for Na_2O, 0.07 for MgO and CaO, 0.03 for TiO_2 and K_2O, 0.02 for P_2O_5, and 0.01 for MnO.

Trace element concentrations based on bulk XRF on pressed powder pellets were obtained by using the intensities at peak and background positions as measured on blank specimens for interpolating background intensity at the peak position (Nisbet et al., 1979). Selected major (Na, K, and Fe) and other trace element concentrations were determined by INAA. Dried rock powders (100–150 mg) were sealed in small polyethylene vials and irradiated for 8 h in the 250 kW Triga Mark-II reactor at the Atominstitut (Vienna, Austria). After a cooling period of up to five days, the subsamples, with international geological reference materials ACE, ALL, and SDO-1, were measured in three counting cycles according to the half-lives of the nuclides in the Gamma Spectrometry Laboratory at the University of Vienna (Mader and Koeberl, 2009). Replicate analysis (n = 15) of GSR1–6 (for bulk XRF) and ACE, ALL, and SDO-1 (all for INAA) yielded a reproducibility for trace elements on the order of ~2–15% RSD.

Due to the large variation in loss on ignition among the different lithologies studied, and to be able to directly compare with other techniques such as μXRF and EMPA, the bulk major element oxide data from ICP-OES and bulk XRF were recalculated and normalized on a volatile-free (H_2O- and CO_2-free) basis, with iron expressed as total ferric iron ($Fe_2O_3^T$). All μXRF, ICP-OES, ICP-MS, bulk XRF, INAA, and EMPA results (samples and reference materials) are reported in Table S2 (see footnote 1).

RESULTS

In this section, we describe the petrographic and geochemical components (types of clasts and groundmass) that constitute the M0077A suevite. Subsequently, the general trends of these components throughout the suevite sequence are described based on petrography and digital image analysis, followed by the stratigraphic trends in bulk major and trace element geochemistry. The observations are listed chronologically from the base (core 90_3; ~732 mbsf) to the top (core 40_1; ~616.5 mbsf) of the investigated core sequence.

Petrography and Geochemistry of Suevite Components

Suevite Clast Types

After detailed petrographic analysis, seven different groups of clasts were identified within the M0077A suevite sequence, namely: vitric melt clasts, microcrystalline melt clasts, felsic basement clasts, mafic basement clasts, silica mineral clasts, primary carbonate clasts, and reacted carbonate clasts. Figures 3–5 show representative thin section overviews of these seven clast types. Table 1 displays the average major element composition of these clast groups based on μXRF mapping results. These clast types form the basis for the digital image analysis shown in Fig. S1.

Impact melt clasts. Silicate impact melt particles (Fig. 3) form the major clast component throughout the M0077A suevite sequence. Two different types were distinguished (Figs. 3A–3B). Vitric melt clasts are very abundant and represent ~40%–70% of the clast population volume depending on the stratigraphic position. The second group comprises the abundant microcrystalline melt clasts, which constitute ~10%–45% of the suevite clast population volume. The vitric melt clasts are characterized by a glassy appearance, a color in plane-polarized light that varies from yellow-green to orange-brown, and a color in cross-polarized light that ranges from yellow-orange to dark-gray. The vitric melt clasts are generally altered, holohyaline clasts that display abundant devitrification throughout the sequence, which is visible as Mg- and Fe-rich smectitic and palagonitic rims around the clasts. Vesicles are often filled with sparry calcite (Figs. 3C and 3E). Rarely, tiny (<30 μm) quartz grains are visible as partially digested clasts in the glassy microtexture. The μXRF-based geochemical compositions of vitric melt clasts (Table 1) indicate that the majority of the analyzed clasts have low total alkali element ($Na_2O + K_2O$) and SiO_2 contents of 0.4–3.3 wt% and 34.6– 53.3 wt%, respectively. The Fe_2O_3 (13.3–39.3 wt%) and MgO (6.6–12.0 wt%) contents are high compared to those of other suevite clast types.

Microcrystalline melt clasts are impact melt rock clasts that are characterized by microcrystalline textures (Figs. 3D and 3F) and a variable degree of entrained clasts. The fine-grained material in these impact melt clasts is dominated by euhedral to subhedral acicular plagioclase laths (in general, 10–30 μm in length, ~75 vol%) and equant clinopyroxene microlites (5–15 μm in length, ~20 vol%) with occasional equant iron oxide minerals (<10 μm in size, <5 vol%). The fine-grained material exhibits varying degrees of alteration to phyllosilicates, which often results in areas with poorly preserved microlites. Microcrystalline melt clasts range in color under PPL from red-brown to dark-brown-black, but this depends highly on the entrained clast content, as both clast-poor and clast-rich microcrystalline melt clasts have been identified throughout the suevite sequence. The entrained clasts within this melt clast type are highly variable in size (from 50 μm to 100 μm up to several millimeters) and can be either isolated entrained minerals (predominantly quartz and K-feldspar) or crystalline basement clasts (mainly granitoid, occasionally gneiss, and rarely dolerite) (Figs. 3G–3H). The geochemistry is variable, but due to the incorporation of mostly felsic components and the generally less severe alteration than in vitric melt clasts, most microcrystalline melt clasts have higher total alkali contents ($Na_2O + K_2O$ of 1.2–8.7 wt%) and higher SiO_2 contents (50.8–67.6 wt%) than vitric melt clasts (Table 1). The Al_2O_3 contents show less variation (11.9–16.8 wt%), but the CaO (4.5–18.7 wt%) and Fe_2O_3 (3.8–13.5 wt%) contents vary significantly from one clast to another.

Crystalline basement clasts. The crystalline basement clasts can be either magmatic or metamorphic in origin and are subdivided into felsic basement clasts and mafic basement clasts (Fig. 4). Petrographically, these clast types strongly resemble the crystalline lithologies described by de Graaff et al. (2021) and Feignon et al. (2020) from Unit 4 in the M0077A core. Both clast types are encountered as isolated clasts or in some rare cases as large, isolated minerals (e.g., feldspar or quartz crystals >200 μm) within the suevite groundmass, or they can be incorporated as entrained clasts within microcrystalline melt clasts. In the latter case, we consider the clast to be part of the microcrystalline melt clast (e.g., as shown in Figs. 3G–3H). The felsic basement clasts are common but not abundant throughout the sequence; they compose <10 vol% of the clast population. They are commonly granitoids that range in size from 5 mm to 10 mm up to several centimeters and are often truncated by the thin section or drill core limits. The granitoid clasts show a wide variety in crystal size (100 μm–~4 cm) but exhibit a rather constant mineral composition of mostly anhedral quartz, K-feld-

Downloaded from http://pubs.geoscienceworld.org/gsa/gsabulletin/article-pdf/doi/10.1130/B36020.1/5365526/b36020.pdf
by Arizona State University user

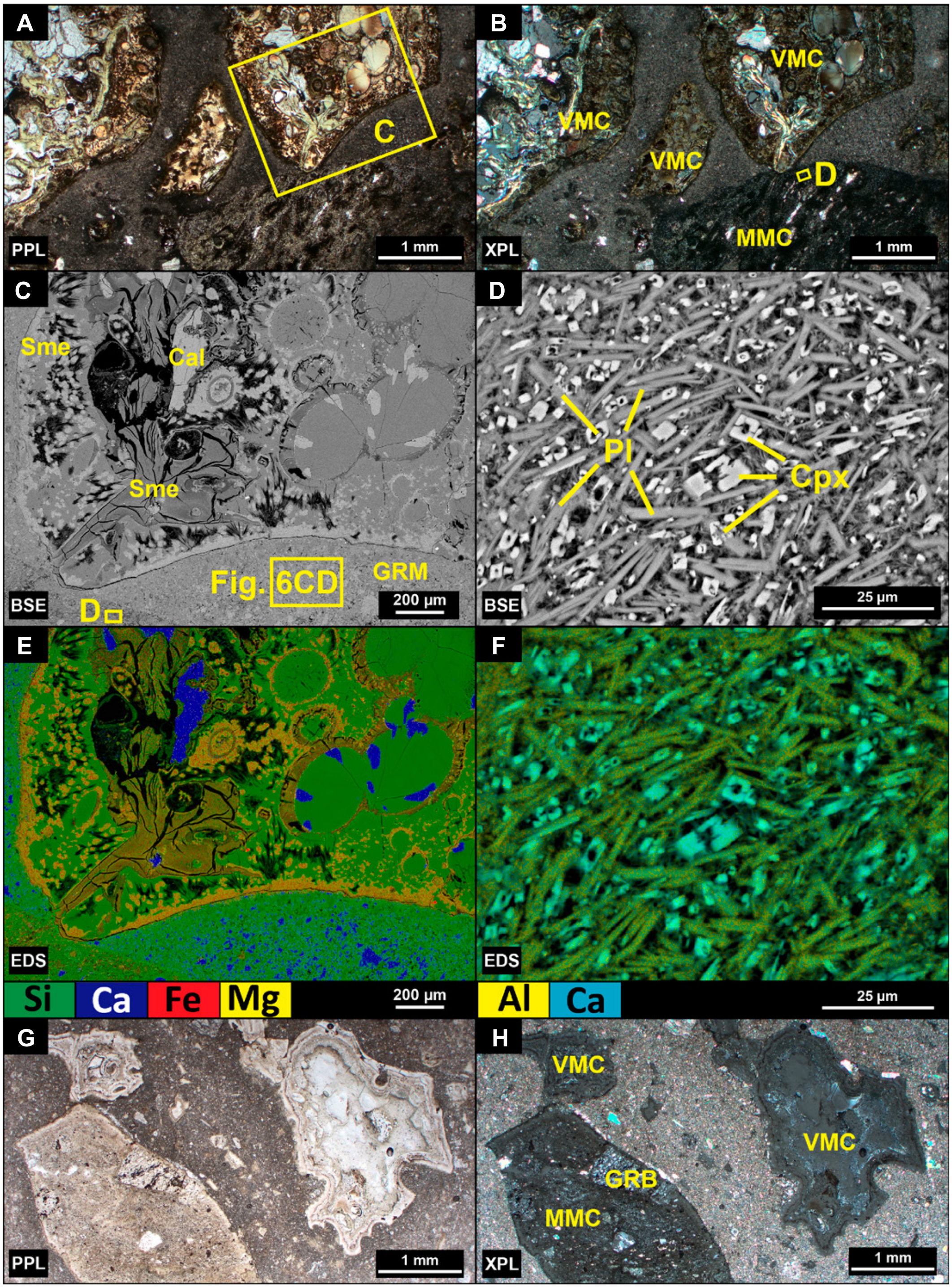

Figure 3. Representative thin section microphotographs, backscattered electron (BSE) images, and element mapping results of vitric impact melt clasts (VMC) and microcrystalline melt clasts (MMC) within the M0077A suevite sequence. (A–B) Plane-polarized light (PPL) and cross-polarized light (XPL) characteristics of both melt clast types in sample 59_2_74_76 (675.91 mbsf). (C–D) Backscattered electron (BSE) images of zoomed-in areas (positions marked in Figs. 3A–3B, respectively) show the glassy microtexture in a vitric melt clast and plagioclase laths and clinopyroxene crystals inside a microcrystalline melt clast. The enlarged area of the suevite groundmass, as shown as the BSE image in Figure 6C, is also indicated. (E–F) Qualitative energy dispersive X-ray spectrometer (EDS)-element maps of both regions of interests (as shown in Figs. 3C–3D) display the silicate glass phases, sparry calcite, and smectitic rim in the vitric melt clast and the chemical differences between the plagioclase and clinopyroxene microlite phases in the microcrystalline melt clast. (G–H) Vitric melt clasts and a clast-rich microcrystalline melt clast in sample 84_2_17_19 (713.71 mbsf). GRM—groundmass; Cal—calcite; Sme—smectite (group); Pl—plagioclase; Cpx—clinopyroxene; GRB—granitoid basement clast inside microcrystalline melt clast (mineral abbreviations from Whitney and Evans, 2010).

spar, and plagioclase (all varying between ~25 vol% and 40 vol%) and minor biotite (<5 vol%) (Figs. 4A–4B). Biotite is commonly replaced by chlorite, which is indicative of alteration of the granitoid clasts. Most granitoid clasts also appear deformed, which can be inferred from quartz grains that often show strong undulose extinction and quartz grains that are "toasted" with an orange brown appearance of the quartz grain that is interpreted to be linked to high post-shock temperatures (Fig. 4C; Whitehead et al., 2002; Ferrière et al., 2009b). However, other shock metamorphic features in the granitoid clasts, such as planar fractures and decorated PDFs in quartz and kink banding in biotite, were only occasionally observed. Up to three sets of PDFs are observed per grain (as seen under the optical microscope), but generally only one or two sets per grain are visible (Fig. 4D). This contrasts the more heavily shocked quartz grains in the granitoid basement from the M0077A core, which yield an average of 2.8 PDF sets per quartz grain (Feignon et al., 2020). The granitoid clast data plot close to the granitic compositional field (Table 1) with some exceptions that are most probably linked to alteration. Two geochemical outliers (sample 73_1_19_21, 699.28 mbsf; and sample 87_2_15_19, 720.87 mbsf) exist that show relatively low SiO_2 (60.6 wt% and 52.1 wt%, respectively), high

Downloaded from http://pubs.geoscienceworld.org/gsa/gsabulletin/article-pdf/doi/10.1130/B36020.1/5365526/b36020.pdf
by Arizona State University user

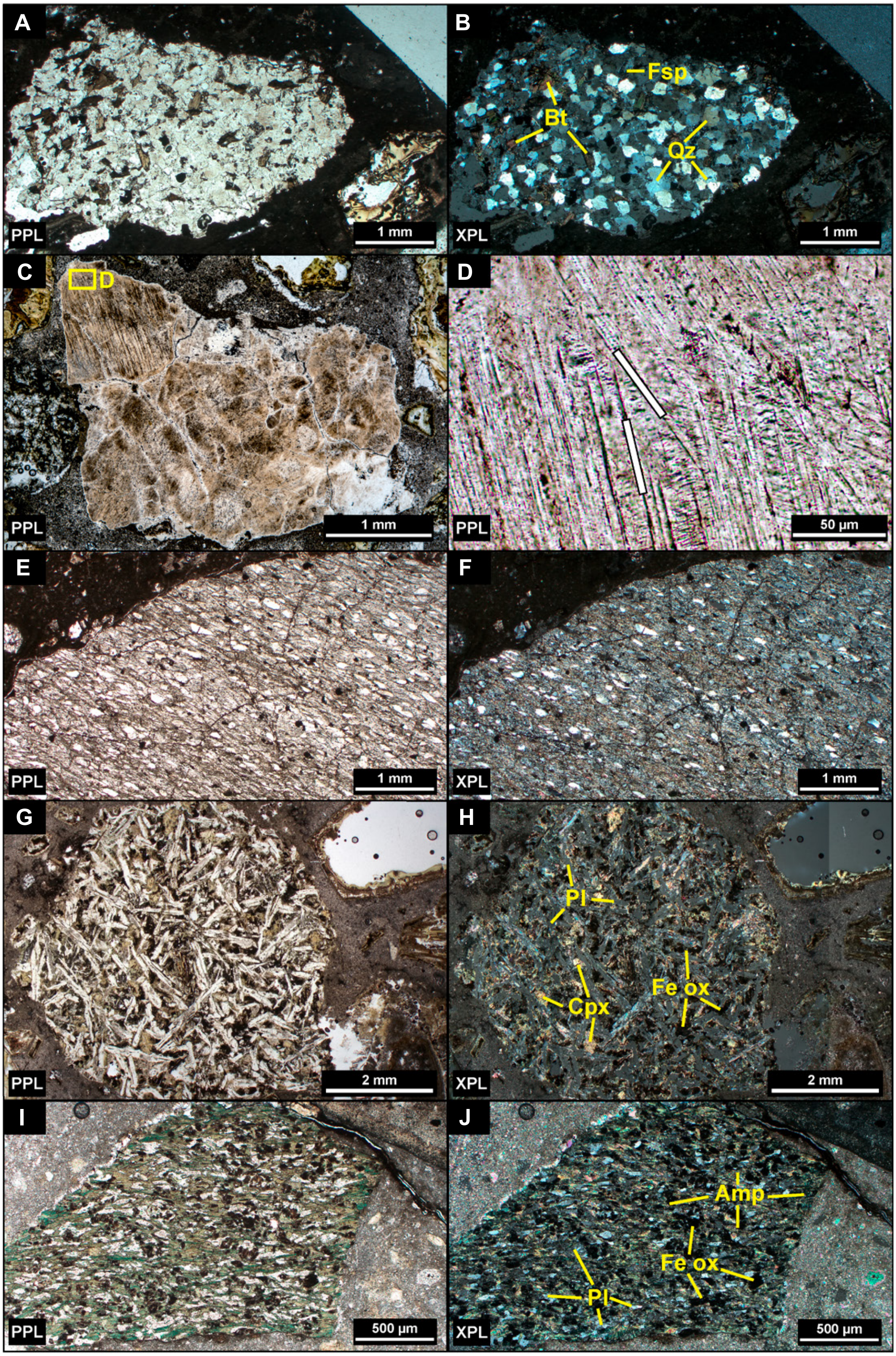

Figure 4. Representative thin section microphotographs of (A–F) felsic basement clasts and (G–J) mafic basement clasts within the M0077A suevite sequence. (A–B) Granitoid clast in sample 62_1_49_51.5 (682.03 mbsf). (C) Shocked and toasted polycrystalline quartz grain derived from the felsic basement within sample 49_1_64_66.5 (644.33 mbsf). (D) Enlarged area of this quartz grain (position indicated in Fig. 4C) with two main orientations of planar deformation features (PDFs) indicated. Additional PDF sets are visible under the universal stage microscope. (E–F) Felsic gneiss clast in sample 67_1_15_17.5 (690.61 mbsf). (G–H) Porphyritic dolerite clast with large, elongated plagioclase laths with clinopyroxene and iron oxides in between (sample 56_2_95_97.5; 667.20 mbsf). (I–J) Amphibolite clast in sample 84_2_17_19 (713.71 mbsf). Bt—biotite; Qz—quartz; Fsp—feldspar; Pl—plagioclase; Cpx—clinopyroxene; Amp—amphibole; Fe ox—iron oxide mineral (mineral abbreviations from Whitney and Evans, 2010). PPL—plane-polarized light; XPL—cross-polarized light.

CaO (12.5 wt% and 12.8 wt%), and intermediate to high Fe_2O_3 (3.9 wt% and 8.9 wt%) contents (Table S2). When excluding these two outliers, the granitoid clast samples display high SiO_2 (66.3–74.8 wt% with, on average, 71.2 wt%) and high total alkali (3.4–9.9 wt%) content and relatively low values of MgO (0.2–2.9 wt%) and Fe_2O_3 (0.9–4.6 wt%).

Felsic gneisses, also classified as felsic basement clasts, are rare (<2 vol%) and are mostly present in the lower and middle part of the suevite sequence. The gneiss clasts are charac-

Downloaded from http://pubs.geoscienceworld.org/gsa/gsabulletin/article-pdf/doi/10.1130/B36020.1/5365526/b36020.pdf
by Arizona State University user

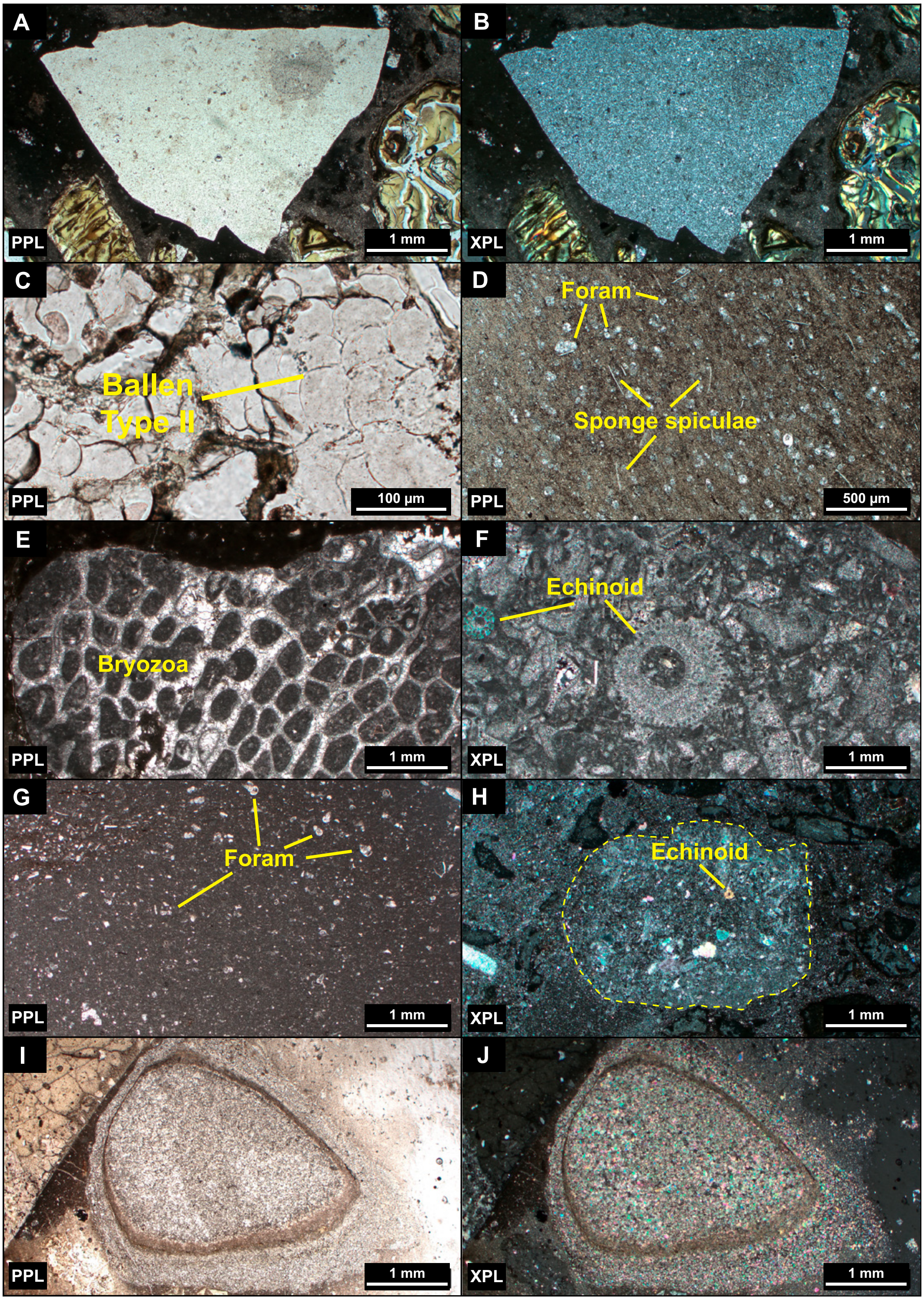

Figure 5. Representative M0077A suevite thin section microphotographs of (A–D) silica mineral clasts and (E–J) clasts derived from the carbonate sedimentary cover. (A–B) Angular silica mineral clast with characteristic "salt and pepper" texture, which is composed of microcrystalline quartz (sample 58_1_30_32; 671.44 mbsf). (C) Ballen quartz type II (Ferrière et al., 2009a) in a silica mineral clast in the basal suevite (81_1_67_69; 708.01 mbsf). (D) Rare chert clast with abundant foraminifera and fossilized spicules of sponges (sample 63_1_7_9.5; 683.41 mbsf). (E–H) Wide range of different primary, fossil-rich carbonate clasts: (E) bryozoan boundstone (65_1_36_38; 688.27 mbsf), (F) echinoid-rich rudstone (63_1_137_140; 684.71 mbsf), (G) foraminifera-rich wackestone (65_1_81_84; 688.72 mbsf), and (H) echinoid-bearing packstone (84_3_27_29.5; 715.09 mbsf). (I–J) Reacted carbonate clast with recrystallized calcite and a melt-corona rim (60_1_45_47; 677.69 mbsf). PPL—plane-polarized light; XPL—cross-polarized light.

terized by preferentially oriented quartz crystals (0.1–0.5 mm, ~50 vol%), mica minerals, which are predominantly biotite (<100 µm in size, ~25 vol%) and in some cases accompanied by porphyroblasts of K-feldspar (0.2–1 mm, ~20 vol%), and a minor fraction of iron oxide minerals (<5 vol%) (Figs. 4E–4F). Compositionally, they are similar to the granitoid clasts except for a lower CaO content, with, on average, 1.5 wt% CaO for the gneiss clasts versus 7.2 wt% for the granitoid clasts.

Mafic basement clasts are also rare (<5 vol%) and mostly present in the lower and middle part of the suevite sequence. They occur as predominantly dolerite and amphibolite clasts, which display varying degrees of alteration. The dolerite clasts can be both equigranular and porphyritic in texture. The porphyritic dolerites (Figs. 4G–4H) are characterized by sub- to euhedral elongated, tabular plagioclase laths (0.3–1.5 mm in length, ~60 vol%), equant clinopyroxene (0.1–0.5 mm in size, ~20 vol%), and equant iron oxide minerals (0.1–0.5 mm in size, ~20 vol%). The equigranular dolerite clasts yield the same mineral assemblage but with smaller crystal sizes

Downloaded from http://pubs.geoscienceworld.org/gsa/gsabulletin/article-pdf/doi/10.1130/B36020.1/5365526/b36020.pdf
by Arizona State University user

TABLE 1. MEAN NORMALIZED MAJOR ELEMENT CONCENTRATIONS OF M0077A SUEVITE COMPONENTS AND BULK ASSEMBLAGES

Component	n	SiO_2	TiO_2	Al_2O_3	$Fe_2O_3^T$	MnO	MgO	CaO	Na_2O	K_2O	P_2O_5	S
Clast types												
Vitric melt clasts	11	44.69	1.61	10.06	25.62	0.23	9.16	6.73	1.08	0.69	b.d.l.	0.14
Microcrystalline melt clasts	12	53.54	0.95	13.71	7.04	0.09	3.87	12.72	4.27	3.26	0.02	0.52
(Felsic) granitoid clasts	8	67.46	0.55	11.76	3.53	0.05	1.94	7.17	3.82	3.06	0.01	0.63
(Felsic) gneiss clasts	2	68.72	0.74	12.71	6.05	0.06	1.40	1.47	5.21	3.38	b.d.l.	0.25
(Mafic) dolerite clasts	3	48.89	1.00	13.78	13.25	0.22	10.89	6.18	3.59	1.60	0.04	0.55
(Mafic) amphibolite clasts	3	52.63	1.36	13.83	14.01	0.20	5.21	8.76	1.96	1.91	b.d.l.	0.13
Silica mineral clasts	4	99.24	b.d.l.	0.31	b.d.l.	0.01	b.d.l.	0.30	b.d.l.	0.03	b.d.l.	b.d.l.
Primary carbonate clasts	6	7.68	0.21	1.53	0.46	1.11	1.09	86.69	0.19	0.62	0.28	0.13
Reacted carbonate clasts	9	5.37	0.13	1.35	1.12	1.31	1.46	88.39	0.34	0.10	0.31	0.13
Groundmass												
40_2_0_3 (617.67 mbsf)	10	49.30	0.14	14.12	0.59	0.08	0.89	25.09	3.78	5.99	n.m.	n.m.
48_1_22_24 (640.86 mbsf)	10	71.29	0.12	8.88	0.17	0.04	0.19	12.76	2.21	4.32	n.m.	n.m.
59_2_74_76 (675.93 mbsf)	10	58.82	0.09	15.95	0.40	0.03	0.54	12.26	4.07	7.83	n.m.	n.m.
67_1_15_17.5 (690.61 mbsf)	10	54.92	0.10	13.15	3.26	0.07	5.62	19.63	1.58	1.65	n.m.	n.m.
82_1_35_38.5 (710.74 mbsf)	10	55.47	0.17	6.24	3.70	0.09	5.74	25.91	2.06	0.60	n.m.	n.m.
Bulk assemblages												
Paleogene sediments: core 40_1(616.52–616.58 mbsf)	5	18.00	0.34	5.07	5.93	0.59	1.84	65.98	0.52	0.88	0.34	1.13
Transitional unit: core 40_1(616.58–617.33 mbsf)	17	4.62	0.10	1.35	2.14	0.96	1.91	83.85	0.12	0.13	0.28	0.82
Suevite: core 40_1 - 41_2 (617.33–620.88 mbsf)	22	34.64	0.57	8.79	3.80	0.24	3.06	40.53	5.80	2.84	0.09	0.40
Suevite: core 41_2 - 48_2 (620.88–642.00 mbsf)	40	49.54	0.68	11.25	6.51	0.14	4.14	19.99	4.45	3.15	0.04	0.16
Suevite: core 48_2 - 60_1 (642.00–678.06 mbsf)	56	50.25	0.69	11.69	7.16	0.14	5.14	18.04	3.68	3.37	0.05	0.10
Suevite: core 60_1 - 81_3 (678.06–710.01 mbsf)	55	45.85	0.66	10.84	6.95	0.17	6.65	24.01	3.00	1.93	0.05	0.25
Suevite: core 81_3 - 84_3 (710.01–715.60 mbsf)	14	35.75	0.67	8.85	6.05	0.17	5.79	38.26	3.33	1.22	0.09	0.43
Brecciated impact melt rock: core 84_3 - 90_3 (715.60–731.69 mbsf)	47	50.83	0.75	13.07	5.73	0.14	3.94	18.15	4.03	3.21	0.06	0.42

Notes: All major element data are expressed as averaged wt% based on volatile-free normalization. Clast data are derived from micro-X-ray fluorescence (μXRF) mapping. Groundmass data from electron microprobe analyzer (EMPA) defocused spot analysis. Whole-rock data are based on bulk XRF, inductively coupled plasma-optical emission mass spectrometry (ICP-OES), and μXRF mapping. n.m.—not measured; b.d.l.—below detection limit. $Fe_2O_3^T$ is total iron.

(<0.5 mm in length) and stronger signs of alteration. The dolerite clasts are mafic in composition with, in general, low SiO_2 (44.9–52.6 wt% with, on average, 48.9 wt%) and K_2O (1.2–1.8 wt%) contents, high Fe_2O_3 (9.9–17.7 wt%) and MgO (6.0–15.4 wt%) contents, and variable Na_2O contents (0.9–7.0 wt%).

The amphibolite clasts show clear metamorphic textures of bands of relatively fine-grained, preferentially oriented amphibole minerals (green in PPL, 100–300 μm in length, ~50 vol%), subhedral plagioclase (50–200 μm in length, ~25 vol%), and equant iron oxide minerals (50–100 μm in size, ~25 vol%) (Figs. 4I–4J). The amphibolite clasts have a similar composition as the dolerites, except that they have slightly higher SiO_2 contents (up to 57.5 wt%) and significantly lower MgO contents (3.9–6.1 wt%).

Mineral and sedimentary clasts. Mineral clasts and carbonate sedimentary clasts (Fig. 5) form another major component of the suevite assemblage (~10–35 vol%). No siliciclastic sedimentary clasts (e.g., siltstone or sandstone) or evaporite clasts (e.g., anhydrite, gypsum, halite) have been detected in the 132 thin sections investigated. Silica mineral clasts are common but not abundant (<10 vol%) and consist almost purely of SiO_2 (with, on average, 99.2 wt%) with only a minor fraction of Al_2O_3 and CaO (both ~0.3 wt%). They are characterized by textures composed of microcrystalline SiO_2 that can be petrographically recognized by a speckled "chert-like salt and pepper" texture (Figs. 5A–5B), which is different from the texture in quartz grains found in crystalline basement clasts. The microcrystalline silica mineral clasts show occasional ballen silica textures that range from Type II to Type V (Ferrière et al., 2009a; Fig. 5C). True chert was also identified based on fossil content of silicified foraminifera and elongated sponge spiculae (Fig. 5D); however, they are extremely rare in the sequence, as only three chert clasts have been found in the 132 thin sections studied.

Carbonate clasts are abundant (~10–25 vol%) and found in the entire suevite sequence. These clasts are subdivided in primary carbonate clasts and reacted carbonate clasts based on the preservation of primary depositional features such as bedding and (micro) fossils. If such characteristics could be recognized and a carbonate rock classification was possible (Dunham, 1962), these clasts were considered to be part of the primary carbonate clast group. Following this classification, a large range is observed in the different types of carbonate rocks, which vary from boundstones (Fig. 5E) and rudstones (Fig. 5F) to micrite-dominated wackestones (Fig. 5G) and packstones (Fig. 5H). Fossils that are present include bryozoans and radiolitid rudist bivalves up to several centimeters in size as well as other types of bivalves, gastropods, echinoids, larger benthic foraminifera (e.g., orbitoids and miliolids), and <100 μm small planktic foraminifera. If carbonate clasts did not retain primary fossils and depositional features, they were classified as reacted carbonate clasts. Generally, this clast group displays recrystallized calcite, which ranges from microcrystalline (<100 μm) sub- to anhedral blocky calcite to euhedral sparry calcite (100 μm to several millimeters). The reacted carbonate clasts often display concentric rings that are composed of Fe-bearing clay minerals (Figs. 5I–5J and S1). If crystallization features fill up vesicles in a non-carbonate clast, which is often the case for vitric melt clasts, the clast is not considered to be a reacted carbonate clast but is considered to be part of a heavily altered, non-carbonate clast. Both types of carbonate clasts yield similar geochemical compositions rich in CaO (~88 wt%) with a small fraction of SiO_2 (<10 wt%) and Al_2O_3 (1–2 wt%). Also, there is a pronounced enrichment in MnO (1–2 wt%) and P_2O_5 (~0.3 wt%) in both primary and reacted carbonate clasts in comparison to the other clast types (Table 1).

Based on granulometric line logging of M0077A halfcore photographs, Ormö et al. (2021) proposed a suevite clast classification with 17 distinct groups that included a red siltstone and red-orange quartzite clast category. Based on petrography and μXRF mapping, we identified one red siltstone clast as a primary carbonate clast (foraminifera-rich wackestone with 82.3 wt% CaO and 10.5 wt% SiO_2) and another red siltstone clast as a microcrystalline melt clast (dominated by a microlite-bearing microtexture with 51.9 wt% SiO_2). The red-orange quartzite clast has been petrographically identified as a reacted carbonate clast with recrystallized blocky calcite and a composition not expected from a quartzite (namely, 74.0 wt% CaO and 15.5 wt% SiO_2).

Suevite Groundmass

According to the definition by Stöffler and Grieve (2007), suevite is characterized by a particulate or clastic groundmass (Fig. 6). In general, we consider isolated particles <200 μm to

Downloaded from http://pubs.geoscienceworld.org/gsa/gsabulletin/article-pdf/doi/10.1130/B36020.1/5365526/b36020.pdf
by Arizona State University user

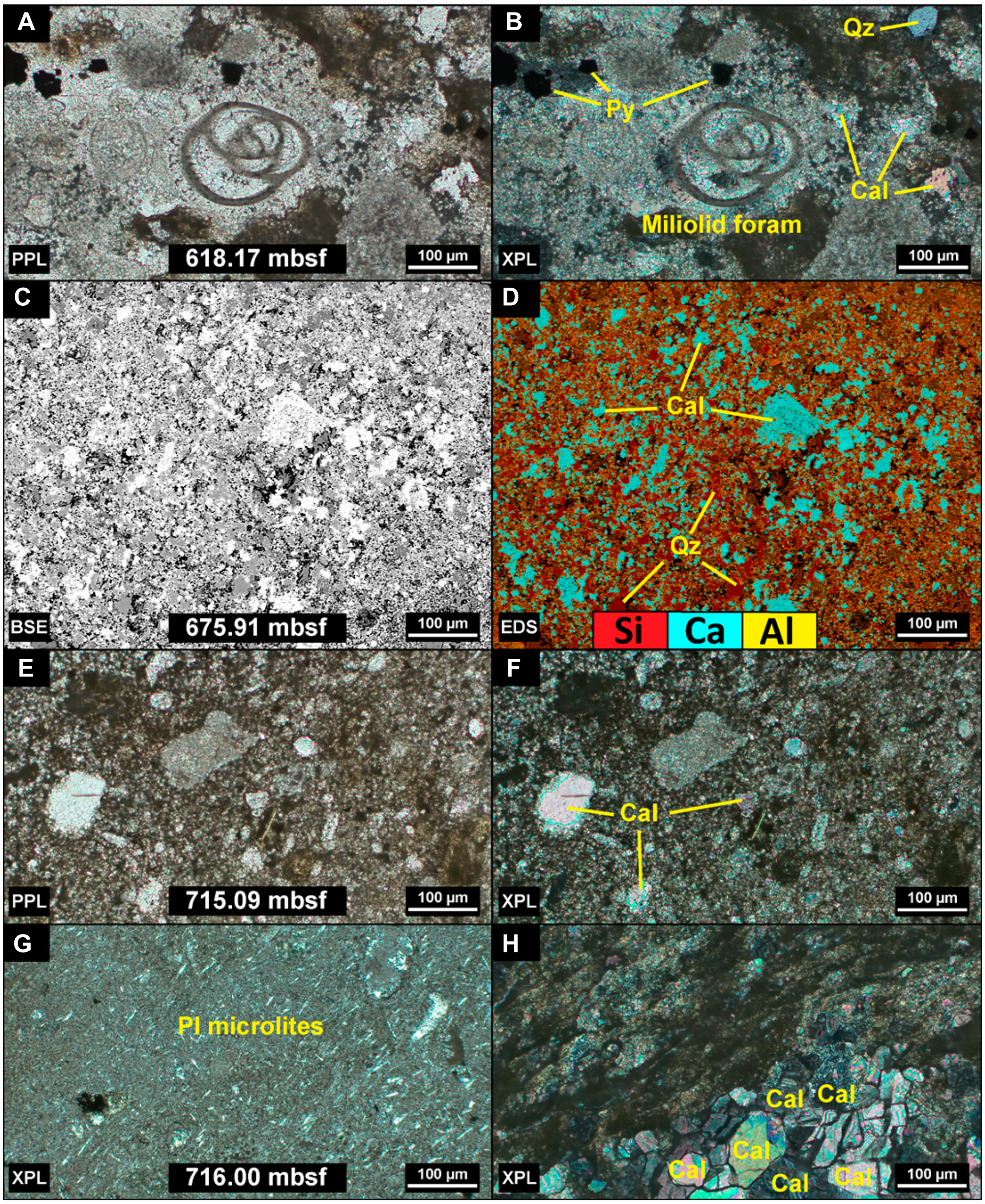

Figure 6. Petrography of the groundmass of the M0077A suevite sequence and the underlying impact melt rock unit. (A–B) Chaotic fine-grained, clastic groundmass near the top of the suevite sequence (sample 40_2_50_53; 618.17 mbsf) with an isolated benthic miliolid foraminifera, pyrite grains, and calcite. (C–D) Scanning electron microscope-backscattered electron (SEM-BSE) image and energy dispersive X-ray spectrometry (EDS) map of the fine-grained clastic groundmass within the middle part of the suevite stratigraphy (sample 59_2_74_76; 675.91 mbsf; see Fig. 3C for the position of this BSE image). It shows a mixture of calcite, quartz, and aluminosilicates. (E–F) Coarser clastic groundmass from the base of the suevite sequence rich in carbonate fragments (sample 84_3_27_29.5; 715.09). (G) Plagioclase microlites inside a melt matrix (sample 84_3_117.5_119.5; 716.00 mbsf). (H) Around the melt matrix in the same sample, schlieren textures are observed that contain large euhedral calcite crystals and dark bands composed of phyllosilicates. Cal—calcite; Pl—plagioclase; Qz—quartz; Py—pyrite; PPL—plane-polarized light; XPL—cross-polarized light.

be part of the groundmass and not of a separate clast group (as described in the previous paragraphs). The groundmass encompasses ~35–50 vol% of the suevite assemblage depending on stratigraphic position. The geochemical composition of the groundmass of five thin sections covering the entire stratigraphic range of the suevite sequence has been investigated by means of defocused EMPA analysis (Table 1). On average, the groundmass in the entire suevite sequence is dominated by SiO_2 (~49–71 wt%) with a major contribution of CaO (~12–26 wt%) and Al_2O_3 (~6–16 wt%) accompanied by a minor contribution of Na_2O (~2–4 wt%), K_2O (~1–8 wt%), MgO (~0.2–6 wt%), and Fe_2O_3 (~0.2–4 wt%). However, when looking in detail into variations versus depth, the groundmasses of the lower two samples (at 710.74 mbsf and 690.61 mbsf, respectively) have higher concentrations of mafic (Fe_2O_3 + MgO) components than the upper three samples (on average, 9.2 wt% vs. 0.9 wt%). The upper three samples (at 675.93 mbsf, 640.67 mbsf, and 617.67 mbsf, respectively) have higher concentrations of total alkalis in their groundmass (9.40 wt% versus 2.94 wt%). In addition, the groundmass of the uppermost sample (Figs. 6A–6B) and the groundmass of the lowermost sample are enriched in CaO in comparison with the other three thin sections (on average, 25.5 wt% versus 14.9 wt%; Table 1).

Microscopy coupled with EDS mapping reveals that the clastic suevite groundmass is composed of subangular to (sub)rounded carbonate, quartz, and aluminosilicate phases (Figs. 6C–6D). Depending on the degree of hydrothermal alteration, fibrous phyllosilicates and desiccation cracks are present in the groundmass, which obscures the clastic nature. The groundmass of the lowermost part of the suevite appears to be less sorted than other parts of the sequence, which is manifested by relatively large carbonate par-

Downloaded from http://pubs.geoscienceworld.org/gsa/gsabulletin/article-pdf/doi/10.1130/B36020.1/5365526/b36020.pdf
by Arizona State University user

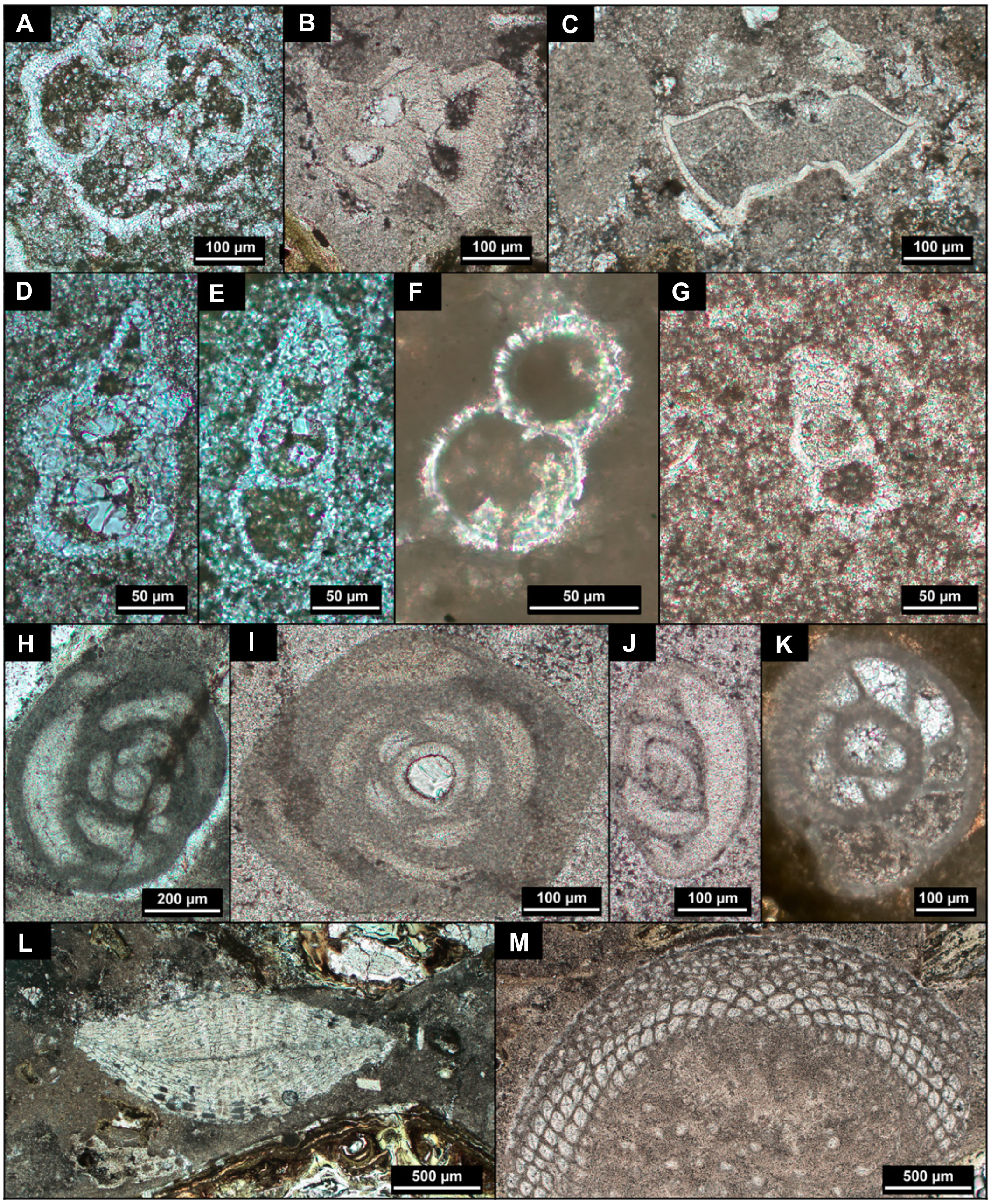

Figure 7. Plane-polarized light microphotographs of (A–G) Cretaceous planktic and (H–M) benthic foraminifera, which are found isolated in the clastic groundmass throughout the M0077A suevite sequence. (A) *Globotruncana linneana* (84_3_27_29.5; 715.09 mbsf). (B) *Globotruncana linneana* (56_2_95_97.5; 667.20 mbsf). (C) *Globotruncana stuarti* (40_2_0_3; 617.34 mbsf). (D) *Globotruncana linneana* (84_3_27_29.5; 715.09 mbsf). (E) *Heterohelix* sp. (84_3_27_29.5; 715.09 mbsf). (F) *Heterohelix* sp. (72_1_74_77; 697.83 mbsf). (G) *Heterohelix* sp. (67_1_15_17.5; 690.61 mbsf). (H) *Quinqueloculina* sp. (59_1_52_54; 674.71 mbsf). (I) Indeterminate miliolid (55_3_8_14; 664.50 mbsf). (J) *Quinqueloculina* sp. (49_3_56_58; 646.64 mbsf). (K) Indeterminate hyaline benthic foraminifera (64_2_8_10; 687.00 mbsf). (L) *Orbitoides* sp. (59_1_52_54; 674.71 mbsf). (M) *Omphalocyclus* sp. (48_1_22_24; 640.86 mbsf).

ticles of 100–150 μm surrounded by smaller silicate particles <50 μm in a sample at 715.09 mbsf (Figs. 6E–6F). This texture is also in strong contrast to the microcrystalline nature of the groundmass found in a thin section 0.9 m lower in the stratigraphy, which is composed of sparry calcite and zones of iron-rich altered glass that are indicative of impact melt rock with schlieren (Figs. 6G–6H).

Isolated Cretaceous foraminifera represent another important component of the suevite groundmass (Fig. 7) and are found throughout the entire suevite sequence. The planktic foraminiferal assemblage (Figs. 7A–7G; in general, 100–500 μm in size) comprises species such as *Globotruncana linneana* (lower Maastrichtian in age), *Globotruncana stuarti* (Maastrichtian), and *Heterohelix* spp. (Turonian to Maastrichtian in age) (Smit, 1982, and references therein). Larger benthic foraminifera (Figs. 7H–7M; in general, 300 μm up to several millimeters in size) range from miliolid foraminifera such as *Quinqueloculina* spp. to orbitoidal foraminifera such as *Omphalocyclus* sp. (Maastrichtian), and hyaline benthic species that are difficult to identify taxonomically are present as well (Alegret and Thomas, 2001, and references therein). Planktic foraminifera have been found throughout the entire suevite sequence; the lowest occurrence is in the lowermost studied suevite thin section 84_3_27_29.5 (715.09 mbsf; Figs. 7A, 7D–7E) and the highest occurrence is in the uppermost studied suevite thin section 40_1_110_111 (617.34 mbsf). To the contrary, benthic foraminifera have only been found from suevite thin section 73_1_19_21 (699.28 mbsf) upwards toward the top of the sequence (up to thin section 40_1_110_111; 617.34 mbsf).

Stratigraphic Trends of the Suevite Sequence

Petrography

Representative petrographic overviews of the M0077A suevite sequence and adjacent units are

Downloaded from http://pubs.geoscienceworld.org/gsa/gsabulletin/article-pdf/doi/10.1130/B36020.1/5365526/b36020.pdf
by Arizona State University user

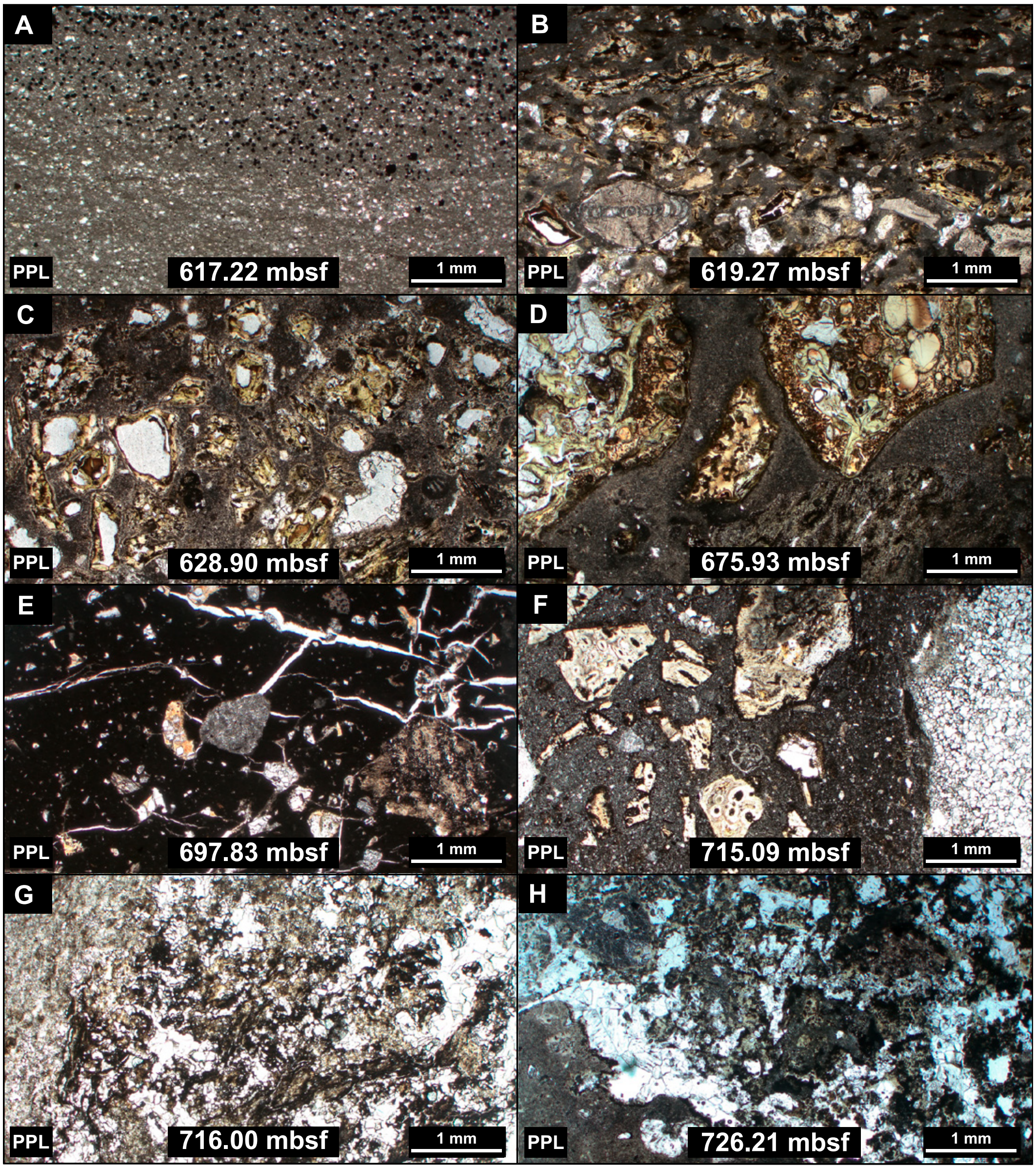

Figure 8. Representative petrographic overviews of different stratigraphic levels found within and adjacent to the M0077A suevite sequence. (A) Transitional unit characterized by horizontally bedded micrite to claystone that is alternated with pyrite levels (as shown here in sample 40_1_98_100 from depth 617.22 mbsf). (B) Uppermost suevite characterized by horizontal to cross bedded, fine-grained strata rich in vitric melt clasts and isolated foraminifera (40_3_23.5_27.5; 619.27 mbsf). (C) Suevite dominated by randomly oriented, small vitric melt clasts (44_1_46_48; 628.90 mbsf). (D) Coarser-grained suevite rich in vitric and microcrystalline melt clasts (59_2_74_76; 675.93 mbsf). (E) Suevite with heavily altered groundmass with open cracks (72_1_74_77; 697.83 mbsf). (F) Poorly sorted lowermost suevite with abundant foraminifera in a coarse, clastic, Ca-rich groundmass (84_3_27_29.5; 715.09 mbsf). (G) Brecciated impact melt rock sample 84_3_117.5_119.5 (716.00 mbsf) dominated by schlieren composed of Fe-rich bands and microcrystalline calcite. (H) Schlieren-rich impact melt rock sample similar to (G) but composed of larger euhedral calcite crystals (89_1_57_59; 726.21 mbsf). PPL—plane-polarized light.

shown in Figure 8 and are qualitatively described in detail below. The basal part of the investigated core sequence between cores 90_3 and 87_2 (~732–721.6 mbsf) is characterized as a clast-poor impact melt rock dominated by aphanitic black melt rock alternating with zones of green material that is designated as schlieren (Fig. 2C). The microtexture of the black melt rock is similar to the microcrystalline melt clasts described above, as it is also microcrystalline and mainly composed of small (<30 μm in length) plagioclase and clinopyroxene microlites with occasional iron oxide minerals. The green schlieren material comprises iron-rich phyllosilicates and crystalline (sparry) calcite that increases in crystal size toward the center of the schlieren bands (Figs. 7G–7H).

At core level 87_3_88 (~721.6 mbsf), a green, ~30-cm-thick zone is present that is poor in impact melt and dominated by sparry calcite. Above this interval, the lithology shows macroscopic characteristics resembling a polymict breccia, as it displays predominantly black angular clasts within a green groundmass with occasional carbonate and crystalline basement clasts (Fig. 2C). However, microscopically, this interval is fairly similar to the brecciated impact melt rock found between cores 90_3 and 87_2, because it shows the same mineralogy and microtextures but in different proportions. To illustrate this, the microtexture of sample 84_3_117.5_119.5 (716.00 mbsf) is dominated by microcrystalline sparry calcite, and this feature is similar to the texture found in sample 89_1_57_59 (726.21 mbsf) (Figs. 8G–8H). The only petrographic difference is that in the lower sample, the green schlieren zones are thinner, but the sizes of calcite crystals are larger. Hence, from 721.6 mbsf upwards the proportions of sparry calcite, carbonate clasts, and crystalline basement clasts increase at the expense of the black aphanitic impact melt rock.

At core level 84_3_78 (~715.6 mbsf), a clear transition in the nature of the impactite sequence is visible. On the halfcore photograph, the groundmass color changes abruptly from green to dark gray-brown, and abundant green-blue clasts of variable sizes (<0.5 cm–2 cm) appear (Fig. S2; see footnote 1). Petrographically, there is also a significant change observed between thin sections 84_3_117.5_119.5 (716.00 mbsf)

Downloaded from http://pubs.geoscienceworld.org/gsa/gsabulletin/article-pdf/doi/10.1130/B36020.1/5365526/b36020.pdf
by Arizona State University user

and 84_3_27_29.5 (715.09 mbsf) (Figs. 8F–8G). A sharp transition occurs from a sparry calcite and iron oxide-dominated crystalline microtexture (Figs. 6G–6H) to a poorly sorted clastic groundmass consisting of predominantly subrounded carbonate fragments (up to 150 μm in size) and abundant isolated foraminifera (Figs. 6E–6F). The clastic groundmass and abundant melt fragments suggest this lithology is a fine- to coarse-grained, groundmass-supported, poorly sorted suevite. This core interval does not show gradation as fine-grained zones (<0.5 cm sized clasts) alternate irregularly with zones of very coarse-grained material with granitoid and carbonate clasts >3 cm in diameter (e.g., in core 84_2 in Fig. 2C). The clasts are predominantly vitric melt clasts, microcrystalline melt clasts, and reacted carbonate clasts, although some primary carbonate clasts with recognizable fossils have been preserved (e.g., Fig. 5H). The foraminifera found in the groundmass are abundant (e.g., up to 15 individuals found in thin section 84_3_27_29.5), and although they are not that well-preserved due to a partial recrystallization to calcite, they are still taxonomically recognizable. The assemblage comprises solely planktic foraminifera such as *Globotruncana* sp. (Figs. 7A–7D) and *Heterohelix* sp. (Fig. 7E) and not benthic foraminifera.

At core level 81_3_2 (~710 mbsf), the poorly sorted suevite sequence is interrupted by a large (~90-cm-thick), dark, aphanitic impact melt rock body (Fig. S3; see footnote 1). Smaller dark melt bodies (10–60 cm) also occur in core 81_1 (708.16 mbsf) and core 80_2 (707.30 mbsf and 706.94 mbsf). This depth regime is dominated by coarse clasts (in general, 1–5 cm in size) that show a gradational fining-upward sequence and a texture that can be both clast-supported or groundmass-supported. This interval also displays a high degree of hydrothermal alteration, which is indicated by orange-red mineralization on the core sections. Furthermore, this section of the drill core suffered the highest core loss of the entire suevite sequence (encountered in cores 79-77, 74-73, 71-69, 67-65, and 60; Fig. 2B). The black to gray-brown groundmass shows fewer carbonate clasts than the suevite interval below ~710 mbsf and is often heavily altered to a phyllosilicate-dominated amorphous texture interspersed with desiccation cracks (Fig. 8E). Isolated foraminifera (both planktic and benthic) are much less common (five were found in 20 thin sections) and are also not recrystallized (e.g., Figs. 7F–7G and 7K). The clast population is diverse and dominated by vitric melt clasts, which are often heavily altered with vesicles filled with sparry calcite, microcrystalline melt clasts, reacted carbonate clasts, and primary carbonate clasts that are supplemented with more exotic clasts such as silica mineral clasts, felsic basement clasts, and mafic basement clasts.

The coarse-grained suevite gradually changes into a medium-grained, groundmass-supported suevite that shows less pervasive hydrothermal alteration. From core 60_1 upwards (~678 mbsf), the microtexture of the brown, clastic groundmass is less obscured by secondary phyllosilicate alteration and cracks (Figs. 8C–8D and 9D–9E). This depth interval does not show a uniform fining-upward trend such as visible in the depth regime ~710–678 mbsf. From cores 60_1–53_3 (~678–658 mbsf), the average clast size declines gradually and, in some cases, abruptly (e.g., at core level 55_3_8; 664.50 mbsf); however, from cores 53_3–48_3 (~658–642 mbsf), the clast size remains relatively constant. The clast population is diverse with a similar amount of vitric melt clasts and microcrystalline melt clasts and a minor fraction of felsic basement clasts, mafic basement clasts, silica mineral clasts, reacted carbonate clasts, and primary carbonate clasts. In core 48_2 (~642 mbsf), a general drop in clast size is apparent both on the halfcore photographs and in thin sections. From this depth upwards, the suevite is fine-grained and well-sorted (Fig. 8C), and it also shows a fining and more well-sorted trend toward the top of the suevite sequence. The groundmass and clast population are similar to those of the suevite interval between cores 60_1 and 48_2 with a predominance of both vitric and microcrystalline melt clasts, although these impact melt clasts are more regularly filled with sparry calcite.

In core 41_2 (~621 mbsf), the color of the halfcore photograph changes relatively abruptly from blue-gray into brown (Fig. S4; see footnote 1). Microscopically, this change is visualized as a sharp transition from a fine-grained, groundmass-supported suevite that displays an architecture of randomly oriented clasts (Fig. 8C) into a very fine-grained, groundmass- and clast-supported suevite that displays clear bedding (Fig. 8B). This texture is characterized as horizontal bedding and imbrication of clasts throughout the uppermost 3.7 m of the suevite sequence (~621–617.33 mbsf) and as cross-bedding in the uppermost 30 cm of the sequence. This suevite contains abundant isolated planktic and benthic foraminifera within its groundmass (Figs. 7C and 8B), with common (sparry) calcite cement and some pyrite grains (Figs. 6A–6B). Vitric melt clasts are the most common clast type in this interval, with a small fraction of silica mineral clasts, primary carbonate clasts, microcrystalline melt clasts, and felsic basement clasts. In addition, thin section sample 41_1_105_109 (620.34 mbsf) contains a unique, silicate glass impact spherule of 1.2 mm in diameter with a vesicle in its center (Figs. 9A–9C). Morphologically, this spherule is well-preserved, but SEM-EDS mapping revealed pronounced alteration to phyllosilicates (Fig. 9D). EDS X-ray intensity maps displaying the relative abundance of Si and Mg suggest that the spherule is surrounded by a rim of Si-rich palagonite and that the material in the center is replaced by Fe-Mg-rich smectite (Figs. 9E–9F).

At core level 40_1_109 (617.33 mbsf), a sharp stylolitized contact separates a light brown, fine-grained suevite from a dark brown, laminated, silty lithology (Figs. 2C and S5; see footnote 1). Only occasionally, rare and small (~10–100 μm in size) impact melt particles were observed in this interval (also see Bralower et al., 2020). However, this interval cannot be considered a suevite, as the host rock of these impact melt particles is a carbonate siltstone and not a polymict impact breccia with components that underwent all stages of shock metamorphism (Stöffler and Grieve, 2007). In addition, this micritic interval is characterized by levels of abundant pyrite crystals (5–100 μm in size) (Fig. 8A). The petrography and geochemistry of this "transitional interval" (617.33–616.58 mbsf; Unit 1G as defined by Gulick et al., 2017) and the overlying green marlstone (basal part of Unit 1F, 617.58–616.55 mbsf) have been described in detail in Goderis et al. (2021), Whalen et al. (2020), and Bralower et al. (2020).

Sedimentology

The qualitative petrographic descriptions above are supported by quantitative digital image analysis based on μXRF mapping of representative thin sections throughout the suevite stratigraphy (Fig. S6; see footnote 1). The results are displayed as quantitative clast group modal abundances, clast size distributions, and clast roundness distributions (all in Fig. 10) as well as sorting curves based on the cumulative area versus perimeter fraction and comparison with sediment sorting scales generally used in geology (Fig. 11). All of these parameters provide insights into the overall sedimentology of the suevite sequence, which—excluding the lowermost sample at a depth of 715.09 mbsf—shows, in general, a fining-, better sorted-, more groundmass supported- and more vitric, melt clast-dominated upward trend while retaining relatively constant roundness of the clasts.

The lowermost analyzed suevite sample (84_3_27_29.5; 715.09 mbsf; Fig. 10E) shows that the suevite assemblage consists of ~49 vol% groundmass, ~33 vol% vitric melt clasts, ~10 vol% microcrystalline melt clasts, and ~8 vol% other clasts, which are mostly reacted carbonate clasts). A unimodal clast size distribution is

Downloaded from http://pubs.geoscienceworld.org/gsa/gsabulletin/article-pdf/doi/10.1130/B36020.1/5365526/b36020.pdf
by Arizona State University user

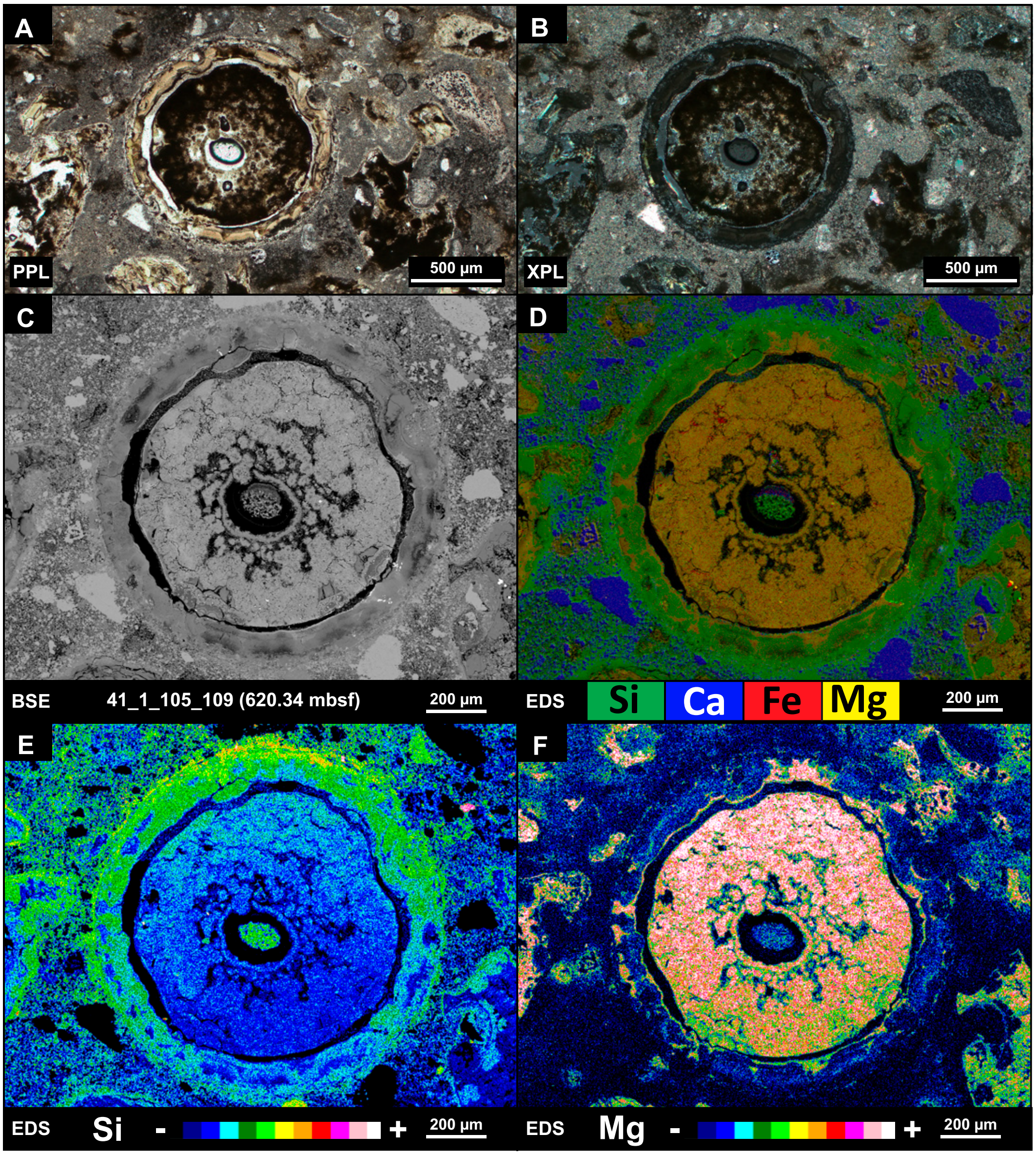

Figure 9. Petrography and geochemistry of a unique 1.2-mm-diameter impact spherule found near the top of the suevite sequence in sample 41_1_105_109 (620.34 mbsf). (A) plane-polarized light (PPL), (B) cross-polarized light (XPL), and (C) backscattered electron (BSE) overviews of the spherule. Energy dispersive X-ray spectrometer (EDS) mapping shows different alteration phases in the spherule based on (D) a qualitative Si-Ca-Fe-Mg multi-element map and semi-quantitative heatmaps that show the relative abundances of (E) Si and (F) Mg.

visible with a median clast size of 0.30 mm, but there is also a tail of some more coarse-grained material up to 6 mm in size. The carbonate clasts (reacted and primary) show more angular shapes (mean roundness of 0.48) than the non-carbonate clasts (vitric melt clasts, microcrystalline melt clasts, felsic basement clasts in this sample: on average, 0.63). The sorting curve of this unit is characterized by a slope of ~2.9 and a non-continuous distribution, which classifies it as a very poorly sorted suevite (Fig. 11B).

A suevite sample ~32 m higher in stratigraphy (63_1_7_9.5; 683.41 mbsf; Fig. 10D) shows 38 vol% groundmass and a wider diversity in clast types. Vitric melt clasts (~30 vol%), microcrystalline melt clasts (~15 vol%), reacted carbonate clasts, and primary carbonate clasts (both ~10 vol%) are dominant, but other more exotic clasts such as silica mineral clasts, felsic basement clasts, and mafic basement clasts (<10 vol%) are also present. The grain-size distribution is relatively broad (median grain size of 0.35 mm), and the sorting curve (slope of ~3.0) corresponds to a very poorly sorted nature (Fig. 11C). The non-carbonate clasts show a more angular shape (average roundness of 0.56) than is observed in the carbonate clasts from this interval (0.62).

A sample from the middle part of the suevite sequence (58_1_30_32; 671.44 mbsf; Fig. S1) displays ~37 vol% groundmass, a similar amount of vitric melt clasts and microcrystalline melt clasts (combined ~55 vol%), and a minor fraction (<8 vol%) of felsic basement clasts, mafic basement clasts, silica mineral clasts, reacted carbonate clasts, and primary carbonate

Figure 10. (A–E) Digital image analysis results for five intervals in the M0077A suevite sequence (617.67 mbsf, 640.86 mbsf, 671.44 mbsf, 683.41 mbsf, and 715.09 mbsf, respectively) with the modal clast-type distribution per analyzed area, the clast size distribution, and the roundness distribution. The suevite components are subdivided into groundmass (GRM), vitric melt clasts (VMC), microcrystalline melt clasts (MMC), felsic basement clasts (FBC), mafic basement clasts (MBC), silica mineral clasts (SMC), primary carbonate clasts (PCC), and reacted carbonate clasts (RCC). The total number of clasts (n) used in the particle analysis is shown; "m" stands for median clast size.

Downloaded from http://pubs.geoscienceworld.org/gsa/gsabulletin/article-pdf/doi/10.1130/B36020.1/5365526/b36020.pdf
by Arizona State University user

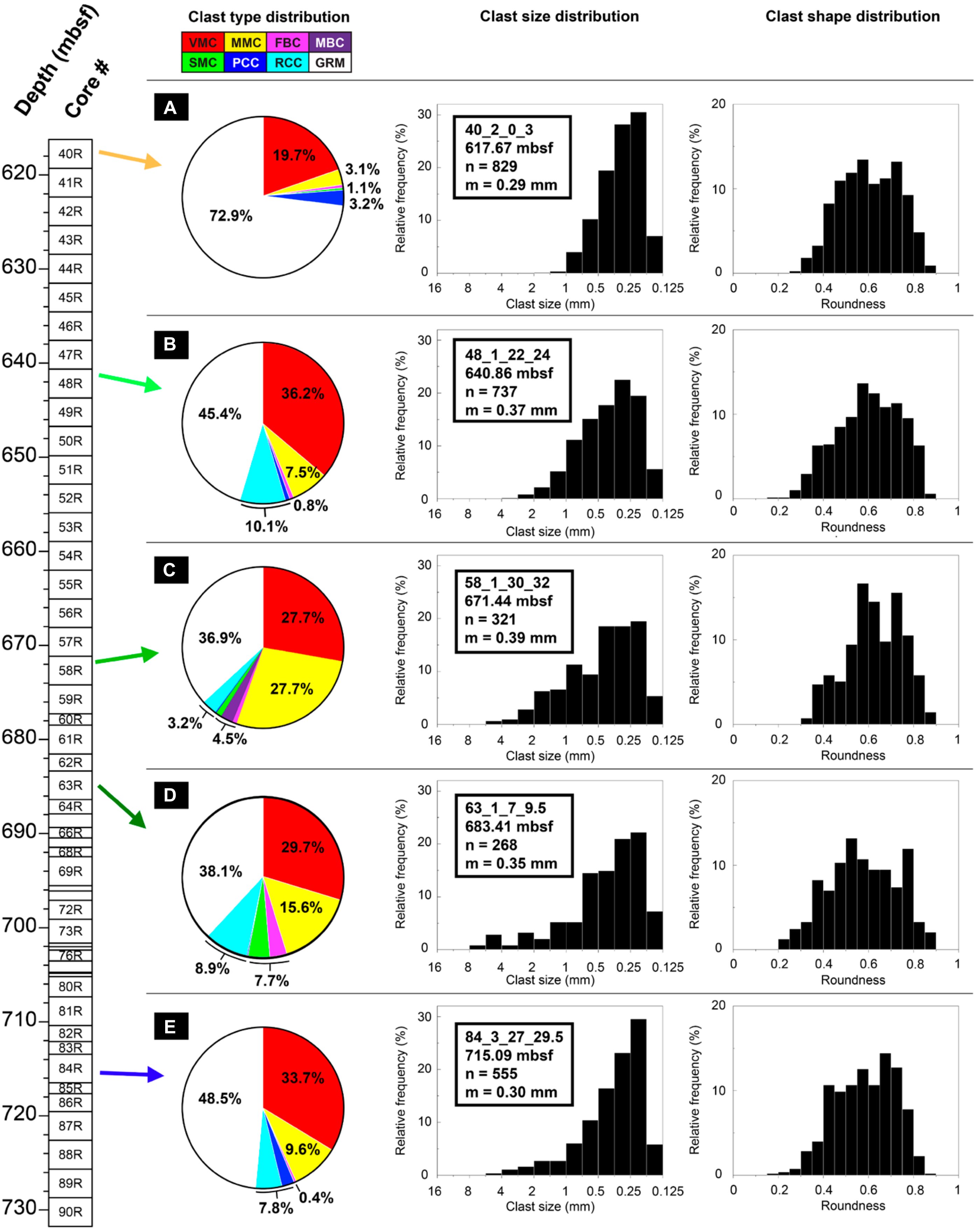

Downloaded from http://pubs.geoscienceworld.org/gsa/gsabulletin/article-pdf/doi/10.1130/B36020.1/5365526/b36020.pdf
by Arizona State University user

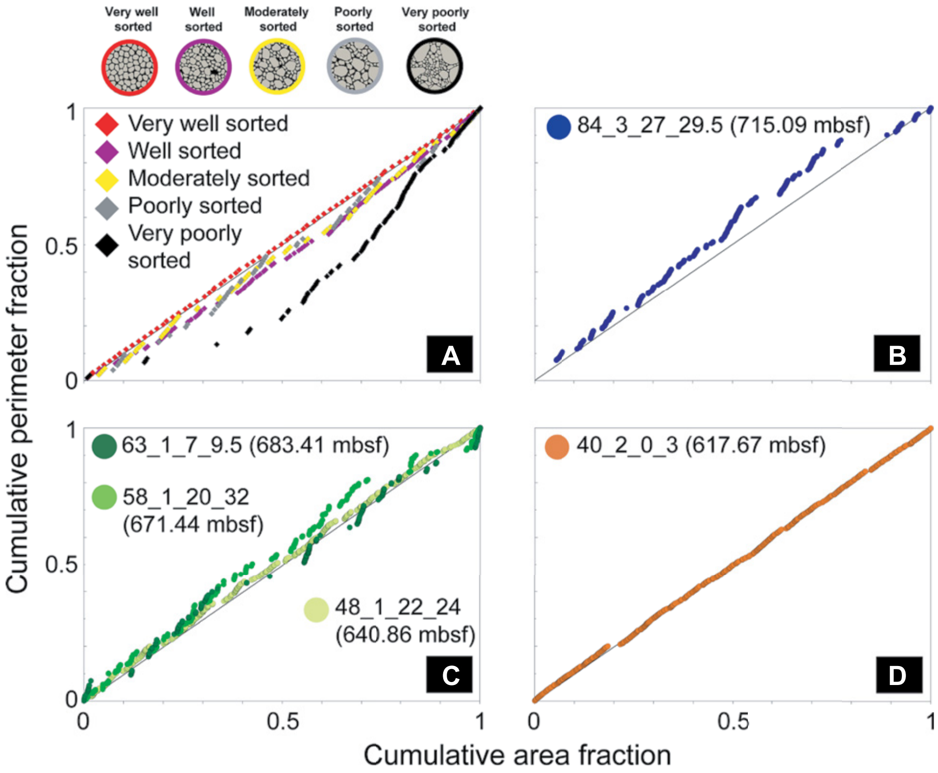

Figure 11. Sorting curves based on digital image analysis of the micro-X-ray fluorescence (µXRF) maps. (A) Five sorting curves (from very well sorted to very poorly sorted) are shown based on the cumulative area versus perimeter fraction (Chanou et al., 2014). These curves are derived from digital segmentation of schematic visualizations of a typical sorting scale used in geology. Very well sorted samples (in red) display a slope of ~1 and are characterized by a continuous linear distribution, whereas very poorly sorted samples (in black) show a discontinuous pattern and can reach slopes larger than ~2.5. (B–D) Image analysis-derived sorting curves of five representative M0077A suevite thin sections. For instance, basal suevite sample 84_3_27_29.5 has a maximum slope of 2.9, which points to a very poorly sorted nature. In general, the suevite sequence shows a trend of better sorting toward the top.

clasts (Fig. 10C). The relatively broad grain-size distribution shows a median grain-size of 0.39 mm and yields carbonate clasts that are slightly more angular than the non-carbonate clasts (mean roundness 0.59 versus 0.64). The sorting curve for this sample shows a slope of ~2 but a distribution that is more continuous than the samples described above. Hence, we classify this interval as a moderately to poorly sorted suevite (Fig. 11C).

Sample 48_1_22_24 (640.86 mbsf) shows a clast population that is less diverse than samples 63_1_7_9.5 and 58_1_30_32, as it is dominated by vitric melt clasts (~36 vol%), carbonate clasts (mostly reacted: ~10 vol%), microcrystalline melt clasts (~8 vol%), and a small fraction of other clasts (e.g., felsic basement clasts, <1 vol%) (Fig. 10B). The groundmass is quite abundant with ~45 vol%. The clast-size distribution is unimodal with a median grain-size of 0.37 mm. The carbonate clasts show slightly more angular shapes than the non-carbonate clasts (mean roundness of 0.55 versus 0.64). The cumulative perimeter versus area fraction shows that this interval is well sorted with an almost continuous pattern and a slope that is ~1.1 (Fig. 11C).

The uppermost analyzed suevite sample 40_2_0_3 (617.67 mbsf) shows an assemblage that is dominated by groundmass (~73 vol%) and vitric melt clasts (~20 vol%) (Fig. 10A). The large amount of groundmass may be partially linked to the segmentation procedure, which excludes clasts that have an area of <0.05 mm^2. The minor fraction (~7 vol%) consists of microcrystalline melt clasts, primary carbonate clasts, silica mineral clasts, and felsic basement clasts. The average roundness for carbonate and non-carbonate clasts in this sample is fairly similar (0.62 versus 0.59). This uppermost stratigraphic sample is the most fine-grained and best sorted within the analyzed sequence with a median clast size of 0.29 mm and a sorting distribution that shows a continuous pattern with a slope of ~1.0; hence, it is a very well-sorted sample (Fig. 11D).

Chemostratigraphy

Whole-rock major element compositional data, based on µXRF mapping (Fig. S6), bulk XRF, and bulk ICP-OES, are visualized as stratigraphic plots in Figure 12 and as averaged values for specific stratigraphic levels in Table 1. Trace element compositions, based on bulk ICP-MS and INAA, are displayed as a stratigraphic contour plot and as averaged CI chondrite-normalized spider diagrams in Figure 13.

Bulk CaO (Fig. 12A) and SiO_2 wt% (Fig. 12B) are the most important contributors to the whole-rock major element composition of the suevite sequence (combined >65 wt%) and show a mirrored pattern. The concentration in CaO is, on average, low in the melt rock interval between ~732 mbsf and 716 mbsf (on average, ~18 wt%), with the exception of four samples derived from the green schlieren zones (up to 70 wt%). From ~716 mbsf upwards, the CaO content significantly increases (19–58 wt% with, on average, ~38 wt%), but it then starts to show very scattered patterns above ~710 mbsf (Fig. 12A). From ~680 mbsf upwards, the CaO content displays a more stable pattern with values varying between ~15 wt% and 25 wt% and not exceeding 30 wt%. From ~621 mbsf upwards, the CaO concentrations exceed 30 wt%, whereas above 617.3 mbsf, these values exceed 50 wt% with a maximum of ~92 wt%.

Most other major element abundances exhibit a pattern mirroring that of CaO, for instance, visible in SiO_2 (Fig. 12B) and Al_2O_3 (Fig. S7A; see footnote 1) with decreasing values between 732 mbsf and 710 mbsf and more stable values throughout the remainder of the suevite sequence. Only K_2O (Fig. 12C) and Na_2O form a slight exception to this rule, as these major elements show consistently low values in the depth interval 710–685 mbsf. The top part of the sequence (620–616.5 mbsf) shows a consistent decrease in all major elements except CaO, MnO, Fe_2O_3, and sulfur. Bulk S values (Fig. S7B) are consistently low in the suevite sequence (on average, <0.5 wt%) with the exception of some outliers that are up to 8 wt%.

Trace element compositions (Fig. 13) show trends similar to those of the major elements. The highest trace element values of the investigated core sequence are found in the depth interval 732–716 mbsf, and this is especially true in terms of the light rare earth elements (LREEs: La, Ce, Pr, Nd, and Sm) with, on average, ~60 times CI chondritic LREE values. This enriched zone is followed by relatively depleted concentrations of trace elements in the depth interval 716–710

Downloaded from http://pubs.geoscienceworld.org/gsa/gsabulletin/article-pdf/doi/10.1130/B36020.1/5365526/b36020.pdf
by Arizona State University user

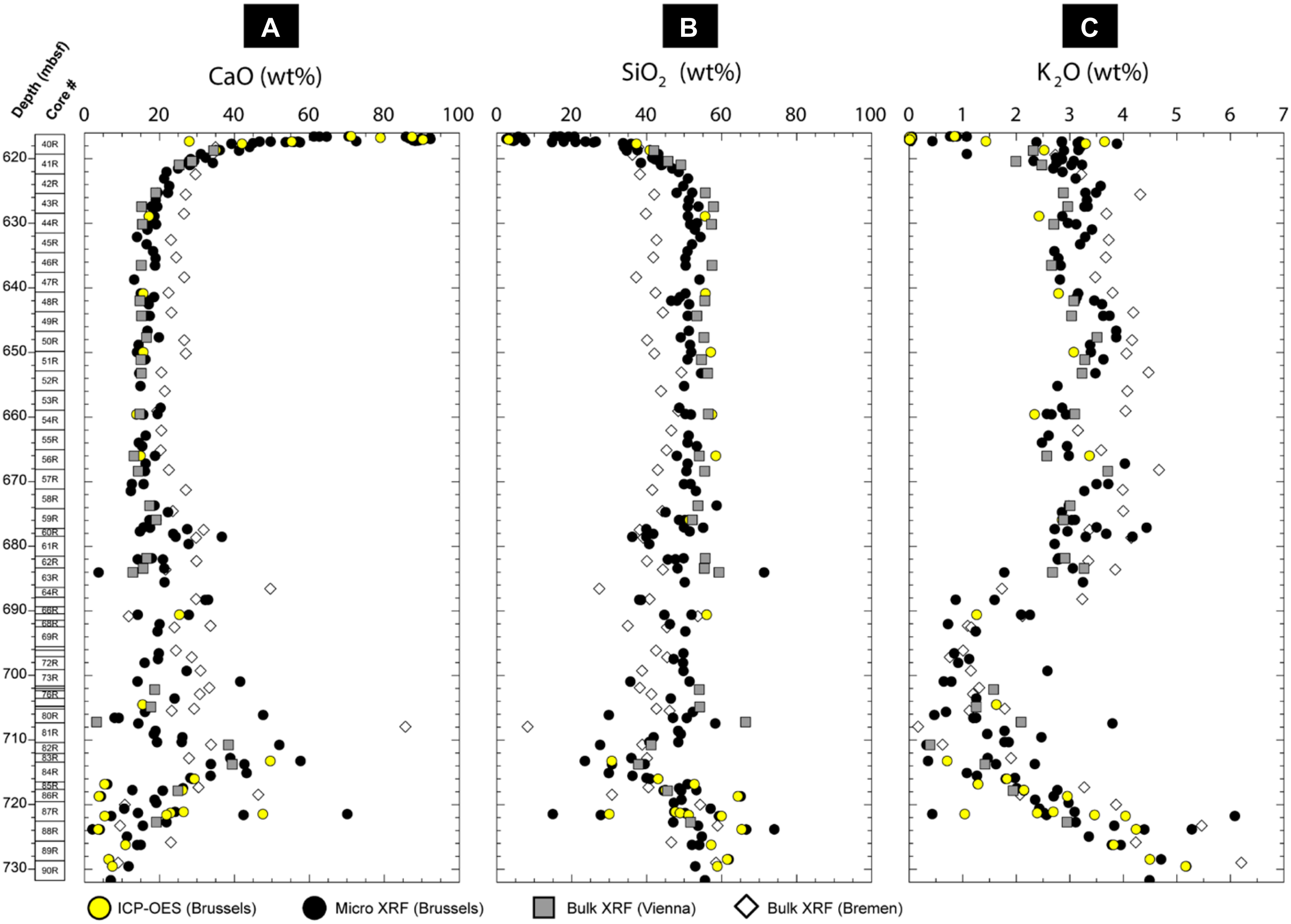

Figure 12. Major element chemostratigraphy of the M0077A suevite sequence with (A) total CaO content, (B) total SiO$_2$ content, and (C) total K$_2$O content (all in whole-rock volatile-free normalized wt%) as a function of depth. ICP-OES—inductively coupled plasma-optical emission mass spectrometry; XRF—X-ray fluorescence.

mbsf, which is especially the case regarding the heavy rare earth elements (HREEs: Eu, Gd, Tb, Dy, Ho, Er, Tm, Yb, Y, and Lu) with, on average, about eight times CI chondritic HREE values. The interval between ~710 mbsf and 620 mbsf shows relatively constant trace element patterns with ~40 and ~13 times CI chondritic values for LREEs and HREEs, respectively. The uppermost 3 m of the suevite sequence (~620–617 mbsf) shows depleted values similar to those in the depth interval 716–710 mbsf, with ~30 and eight times CI chondrite values for LREEs and HREEs, respectively. This uppermost part also displays the highest content in Sr of the entire set of investigated samples with 106 times CI chondritic values for Sr (Fig. 13).

In summary, the bulk geochemical variations in the suevite stratigraphy (Figs. 12–13) largely reflect the stratigraphic variations found in the modal abundances of clast types based on digital image analysis (Fig. 10). In general, a wide diversity of clast groups is found throughout the suevite sequence, and clast populations do not differ significantly with depth. Vitric melt clasts are the most dominant clast group in all intervals (>25 vol%), but they are more abundant in the lowermost and uppermost sample studied (>33 vol%). These two intervals also show a higher proportion of groundmass and higher CaO values for both the groundmass (based on defocused EMPA; Table 1) and the bulk assemblage (based on µXRF mapping, bulk XRF, and bulk ICP-OES). The other suevite interval (between ~710–621 mbsf) shows more diversity in clasts with a higher abundance of, for example, silica mineral clasts, mafic basement clasts, and felsic basement clasts. Bulk X-ray diffraction (XRD) mineral data from Gulick et al. (2017) were used for comparison with the geochemical and modal abundance clast-type data from this study. These XRD data show that there is no clear mineralogic trend in the M0077A impactite sequence with depth (Fig. S7C). Calcite, quartz, feldspar, smectite, mica, and pyroxene are present at more or less all depths throughout the sequence with variations in relative abundances ranging from >5–25 vol%.

DISCUSSION

New Classification of the M0077A Suevite Sequence

The nomenclature of suevite in impact cratering studies remains a topic of considerable debate (e.g., Osinski et al., 2004, 2016, 2020; Stöffler and Grieve, 2007; Reimold et al., 2012; Stöffler et al., 2013). To avoid any confusion regarding the mechanisms for suevite formation, the term suevite is used here solely as a descriptive term,

Downloaded from http://pubs.geoscienceworld.org/gsa/gsabulletin/article-pdf/doi/10.1130/B36020.1/5365526/b36020.pdf
by Arizona State University user

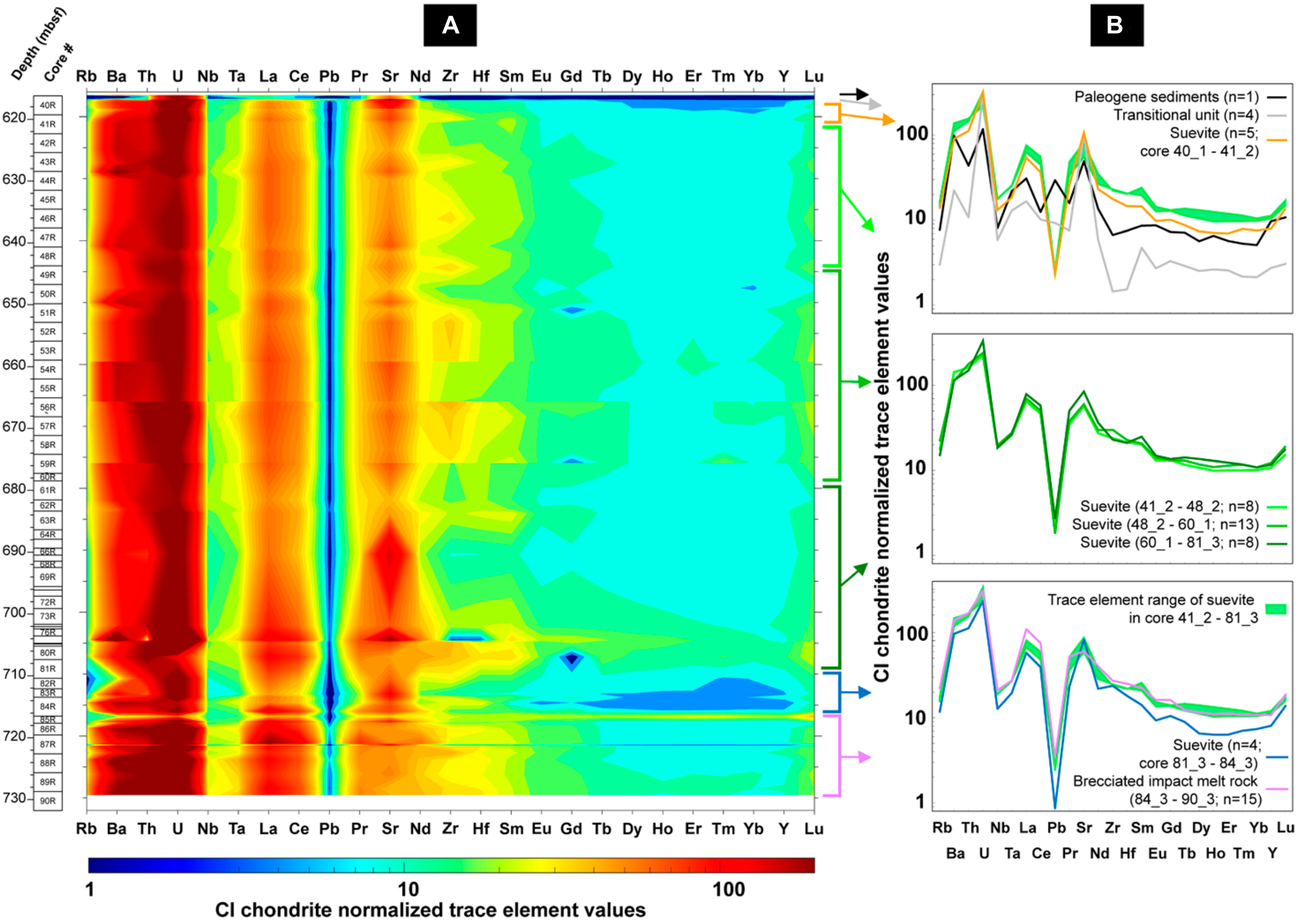

Figure 13. CI chondrite-normalized trace element compositions of the M0077A suevite and adjacent units, based on bulk instrumental neutron activation analysis (INAA) and inductively coupled plasma-mass spectrometry (ICP-MS) (CI chondrite reference values are from Sun and McDonough, 1989). Data are shown as (A) a stratigraphic contourplot with the CI chondrite-normalized values displayed on a logarithmic color scale and as (B) averaged curves for eight stratigraphic intervals similar to the drill core intervals chosen in Table 1.

and any adjectives are based on petrographic and macroscopic observations, e.g., bedded suevite instead of using interpretive terms like “fallback suevite,” “fallout suevite” (Pohl et al., 1977), or “reworked suevite” (Tuchscherer et al., 2004). For Chicxulub, mostly as a result of the lack of outcrop and core material and the use of different criteria by different authors, there is currently no clear consensus on emplacement models for suevite within and outside the crater (e.g., Claeys et al., 2003; Dressler et al., 2004; Goto et al., 2004; Kring et al., 2004; Stöffler et al., 2004; Tuchscherer et al., 2004; Wittmann et al., 2007; Gulick et al., 2019; Osinski et al., 2020). A solid classification of the new continuous impactite sequence of the M0077A core may help solve this conundrum, as it provides a complete record of depositional variations within the crater through time. Therefore, the M0077A core can serve as a reference section to compare with more fragmented (e.g., the Y6 and S1 drill cores) or “slumped” records (e.g., the Yax-1 drill core) elsewhere in the crater (Fig. 1A) and aid in extrapolating lateral changes of the suevite deposit throughout the crater. However, M0077A is the only core located offshore and on the Chicxulub peak ring; thus, it represents the most elevated depositional location of the drill sites (Fig. 1B). This depositional setting, combined with evidence of hydrothermal alteration (e.g., Kring et al., 2020), therefore may be prone to different environmental conditions than the locations of the other drill cores recovered within the Chicxulub structure.

The initial classification of the upper peak ring succession in the M0077A core (Unit 2A-C and 3A-B) was mostly based on macroscopic observations and geophysical data (Gulick et al., 2017). As suevite is defined as an impact melt-bearing polymict breccia with a particulate or clastic matrix containing lithic and mineral clasts of all stages of shock metamorphism, the nature of the groundmass is a key factor in discriminating (clast-rich) impact melt rock (sometimes referred to as “impact melt breccias” or “impact melt rock breccias”) from suevite (Osinski et al., 2004). Other microscopic features, for instance, changes in the modal abundance of different clast groups, and quantitative sedimentary characteristics such as distributions of clast sizes, clast sorting, and clast shapes, are used in this study—together with geochemistry—to differentiate between different types of suevites within the ~100-m-thick sequence on the Chicxulub upper peak ring. We postulate that this approach can be used to better discriminate between the different emplacement scenarios of suevite as petrographic observations can be linked to changes in energy regime over time and specific interactions between impact melt and the atmosphere or seawater.

Downloaded from http://pubs.geoscienceworld.org/gsa/gsabulletin/article-pdf/doi/10.1130/B36020.1/5365526/b36020.pdf
by Arizona State University user

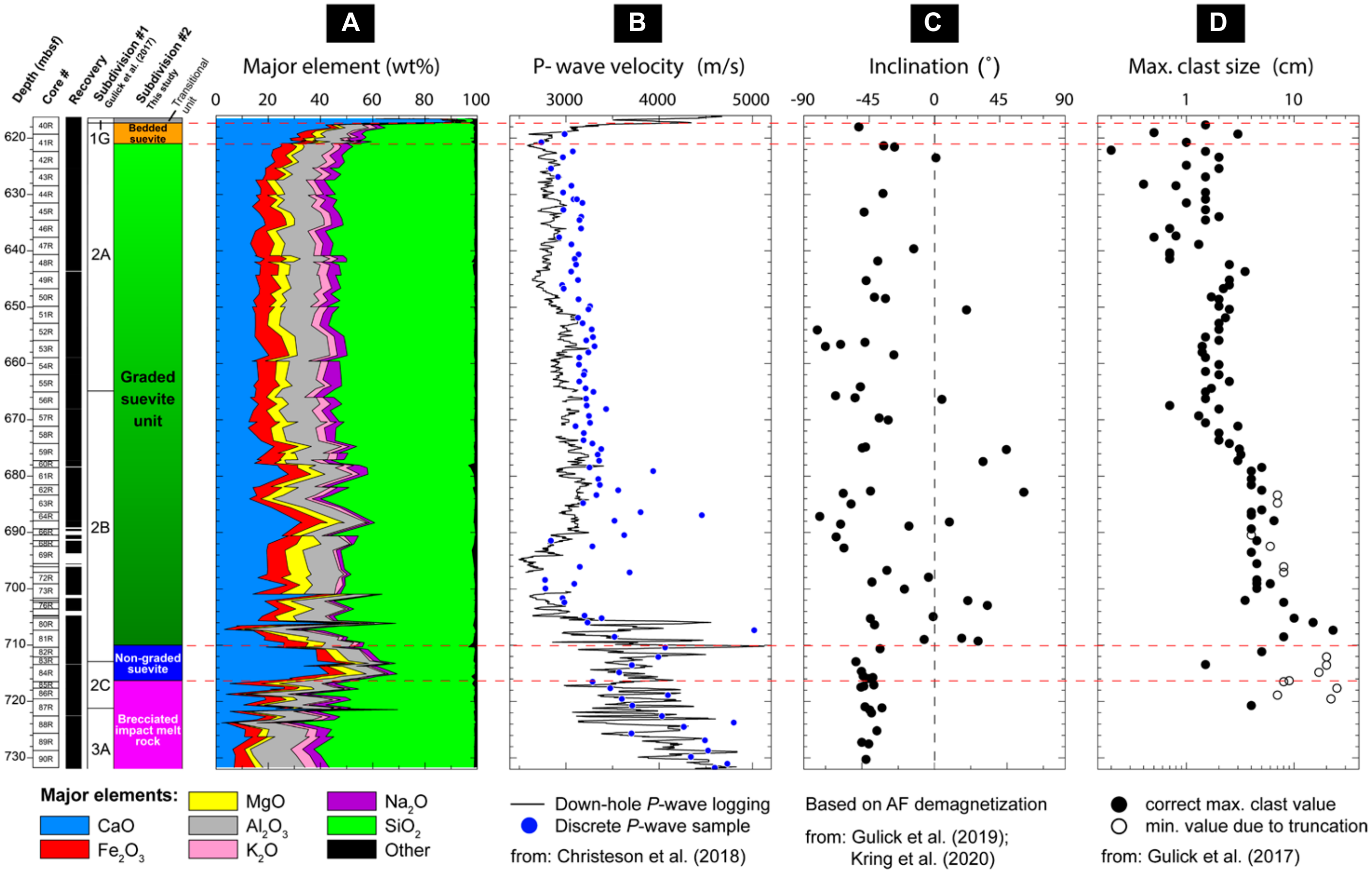

Figure 14. Multi-proxy record of the M0077A suevite stratigraphy. (A) Normalized major element plot with data based on micro-X-ray fluorescence (µXRF) mapping, bulk inductively coupled plasma-optical emission mass spectrometry (ICP-OES), and bulk X-ray fluorescence (XRF). (B) Seismic *P*-wave velocity data from down-hole logging and discrete samples (from Christeson et al., 2018). (C) Magnetic inclination values based on alternating field (AF) demagnetization (from Gulick et al., 2019; Kring et al., 2020). (D) Maximum clast size data, derived from visual core descriptions with top depth of each core section used on the vertical axis (from Gulick et al., 2017).

Furthermore, we combine our quantitative petrographic, sedimentological, and geochemical database with existing independent data sets (Fig. 14) such as geophysical logging data, paleomagnetic data, macroscopic core observations, and computed tomography (CT) data. This helps to extrapolate our discrete sample results with continuous full core width logging data. Petrographic interpretations and image analysis data can be biased by large clasts that cover a large area of the thin section surface. This is especially the case for the coarse-grained intervals between ~710 mbsf and 680 mbsf.

In the paragraphs below, we present a new classification of the M0077A suevite sequence that can be linked to different depositional processes and that is based on the multi-proxy approach described above. We propose that the complete suevite sequence in this core is ~98.3 m thick (715.60–617.33 mbsf) and can be subdivided into three main units (Fig. 2C): the non-graded suevite, graded suevite, and bedded suevite units, which overlie a brecciated impact melt rock unit and underlie the transitional unit. These different suevite units are described from the bottom to the top of the sequence and are compared to the previous classification of Gulick et al. (2017).

Non-Graded Suevite Unit (715.60–710.01 mbsf)

The non-graded suevite unit is a ~5.6-m-thick unit (Fig. 8F; from core level 84_3_78 to 81_3_2) that forms the basal part of the M0077A suevite sequence. This unit is macroscopically characterized as a fine- to coarse-grained, groundmass-supported, non-graded, poorly sorted suevite with a dark-brown groundmass and abundant greenish-bluish melt fragments. The non-graded suevite unit is both petrographically and geochemically distinct from the overlying graded suevite unit and the underlying brecciated impact melt rock.

In their original classification of the M0077A drill core, Gulick et al. (2017) included the core interval between 721.62 mbsf and 715.60 mbsf (core 87_2_90–core 84_3_78) as part of the suevite sequence (classified as Unit 2C). However, this interval effectively fits the criteria of impact melt rock according to the International Union of Geological Sciences Subcommission on the Systematics of Metamorphic Rocks (see Stöffler and Grieve, 2007). This definition states that impact melt rocks are “crystalline, semi-hyaline or hyaline rocks solidified from impact melt and containing variable amounts of clastic debris of different degree of shock metamorphism.” The aphanitic black phase in the interval between 721.62 mbsf and 715.60 mbsf fits this definition, as it consists of a microcrystalline, plagioclase-microlite-dominated melt microtexture with occasional iron oxide minerals. This black melt is not surrounded by a clastic groundmass but by zones of green schlieren that consists of iron-rich clay minerals and sparry calcite

Downloaded from http://pubs.geoscienceworld.org/gsa/gsabulletin/article-pdf/doi/10.1130/B36020.1/5365526/b36020.pdf
by Arizona State University user

(Figs. 6G–6H and Fig. 8G). This green schlieren is similar to the microtextures (Fig. 8H) found in the impact melt rock between 732 mbsf and 721.62 mbsf (classified as impact melt rock Unit 3A according to Gulick et al., 2017), except that the amount of green schlieren is comparatively enhanced. These two intervals are also highly similar in bulk major and trace element composition (Figs. 12, 13, and 14A) with the exception of the REE-depleted sample 87_2_73_75 (721.45 mbsf) that is derived from the center of a 30-cm-thick zone enriched in sparry calcite. This carbonate zone can be interpreted as an interval similar to the CaO dissolution and re-cementation zone described in the brecciated impact melt rock Unit 5 in the Yaxcopoil-1 drill core (Tuchscherer et al., 2004).

Hence, we classify the interval between 721.62 mbsf and 715.60 mbsf as being a continuation of impact melt rock Unit 3A as defined by Gulick et al. (2017). This means that Unit 3A, containing brecciated impact melt rock, is extended by ~6 m (Fig. 2C) with an increasing contribution of green schlieren toward the top. This trend is also reflected in geophysical data, as there is a gradual but distinct decrease of seismic P-wave velocity (from ~4800–3200 m/s) and a slight increase in porosity (from ~15–25%) between ~732–716 mbsf (Christeson et al., 2018), which is indicative of an intensification of brecciation toward the top of the impact melt rock unit (Fig. 14B).

We place the boundary between the brecciated impact melt rock and the non-graded suevite unit at 715.60 mbsf on the basis of multiple lines of evidence. Firstly, two sequential thin sections (84_3_117.5_119.5 and 84_3_27_29.5; 716.00 and 715.09 mbsf, respectively) show distinct variations in the nature of the groundmass, namely a microcrystalline (black melt phase) and macrocrystalline (sparry calcite from the green schlieren) matrix in the lower sample versus a clear clastic groundmass in the upper sample, which is dominated by carbonate fragments and planktic foraminifera and has no green schlieren-related textures. Secondly, a geochemical change is observed in μXRF maps of two samples that are even more closely spaced than the two thin sections described above (i.e., 84_3_104_106 and 84_3_70_72.5; 715.52 and 715.43 mbsf, respectively). The semiquantitative μXRF maps of Ca (Figs. S2 and S6) indicate that the non-graded suevite samples display higher Ca concentrations throughout the entire groundmass area, whereas in the underlying brecciated impact melt rock unit, the Ca is concentrated in the schlieren zones. The μXRF mapping also illustrates that the groundmass is depleted in iron rich mineral phases, in contrast to the impact melt rock interval below (Fig. S2). Thirdly, an abrupt change in CT facies is observed at 715.60 mbsf, as at this depth, the CT number of the matrix increases due to an increase in bulk density (Gulick et al., 2017). This is most probably caused by an increase in the CaO content (Fig. 14A), which may reflect a better cementation of this unit compared to the brecciated impact melt rock unit below. With the macroscopic change visible on the halfcore photograph from this depth, which is reflected by an abrupt increase in small clasts that display a jigsaw texture and a change in groundmass color from green to dark brown, we interpret the termination of the impact melt rock interval and the onset of the suevite sequence to occur at the core depth of 715.60 mbsf (Fig. S2).

Graded Suevite Unit (710.01–620.88 mbsf)

The graded suevite unit is ~89 m thick (Figs. 8C–8E; from core level 81_3_2 to 41_2_13) and represents the main part of the M0077A suevite sequence. This thick unit shows a clear fining-upward trend (Fig. 2C), together with a better sorting (Fig. 11C) and a more groundmass-supported nature toward the top, while being characterized by rather constant roundness values of clast components (Figs. 10B–10D) and whole-rock geochemical composition with depth (Fig. 14A). We place the boundary with the non-graded suevite unit at 710.01 mbsf because at this depth interval the sequence is interrupted by a large (~0.9-m-thick) dark, aphanitic impact melt rock body (Fig. S3). Above this melt rock body, coarse clasts of different origins prevail (including felsic and mafic basement clasts; Fig. 10), and the groundmass is depleted in carbonate fragments and foraminifera (Figs. 8C–8E) compared to the underlying non-graded suevite unit. Moreover, the graded suevite unit is characterized by a lower seismic velocity (~3000 m/s versus ~3500 m/s) (Fig. 14B), lower density (~2.1 g/cm^3 versus ~2.3 g/cm^3), and a higher porosity (~35% versus ~25%) than the non-graded suevite unit (Christeson et al., 2018; Gulick et al., 2019).

In addition, the paleomagnetic signals above and below 710.01 mbsf are clearly distinct. Gulick et al. (2019) and Kring et al. (2020) reported stepwise alternating field demagnetization results for the upper peak ring impactites, which show consistent negative inclination values between −35° and −54° in the non-graded suevite unit and the impact melt rock units below (Units 2C, 3A, and 3B) (Fig. 14C). This implies that these impactites were emplaced above the Curie temperature of magnetite (580 °C) and cooled in situ. Hence, they recorded a full thermal remanent magnetization with an inclination of ~–46°, which is expected for the geographic location of the Chicxulub impact site at ~66 million years ago during reversed magnetic chron 29r (Gulick et al., 2019). In contrast, the graded suevite unit shows heavily scattered (both positive and negative) magnetic inclination values. The first sample that shows a clearly different paleomagnetic signal is 709.27 mbsf (+30.1°), and this signal remains highly variable up to the top of the graded suevite unit (Fig. 14C). This suggests that the components of the graded suevite unit did not experience sufficient heating to thermally reset their pre-depositional magnetization directions following emplacement (Gulick et al., 2019).

The lower part of the graded suevite unit (~710–680 mbsf) shows a high degree of hydrothermal alteration, which causes visual macroscopic and microscopic changes to the texture and components of these rocks especially in vitric melt clasts. The clastic groundmass of the suevites in this interval is commonly obscured by secondary phyllosilicate alteration and desiccation cracks (Fig. 8E). Previous work on the effects of the post-impact, alkaline-intermediate hydrothermal system on the suevites in the M0077A core documented secondary alteration throughout the entire sequence but especially in the lower portion of unit 2B (Simpson et al., 2020). This high-porosity (30%–40%) and high-permeability interval (at depths of 706–689 mbsf) is also marked by the largest amount of core loss in the M0077A suevite sequence (Fig. 2B). Perlitic cracks were observed in this interval by Kring et al. (2020) as well, while Simpson et al. (2020) also documented more abundant Na-dachiardite and analcime zeolites at these depths. At core level 60_1_82 (678.06 mbsf), a gradual transition is visible to a core interval with less core loss and less pervasive hydrothermal alteration features. Macroscopically, this can be seen, for example, in the decrease in red-orange mineralization caused by Na-dachiardite (Simpson et al., 2020). Microscopically, this change is visible as a relatively well-preserved brown groundmass that displays a true clastic nature (Figs. 6C–6D and Fig. 8D).

Besides these variations in hydrothermal alteration, minor grain-size changes were noted in the middle part of the graded suevite unit that are superimposed on the general fining-upward trend of the unit. For example, a slight drop in clast size is visible between core 61_1 and core 60_1 (~678 mbsf) as can be seen in the maximum clast-size curve in Figure 14D. From that depth regime (~678 mbsf) upwards, the suevite shows a general fining-upward sequence until ~659 mbsf (core 54_1). An abrupt drop in clast-size is visible at core level 55_3_11 (664.52 mbsf). Gulick et al. (2017) placed the boundary between units 2A and 2B at this particular depth interval based on an oblique, erosional surface. However, petrographically, samples below and

Downloaded from http://pubs.geoscienceworld.org/gsa/gsabulletin/article-pdf/doi/10.1130/B36020.1/5365526/b36020.pdf
by Arizona State University user

above 664.52 mbsf appear similar in terms of groundmass characteristics and clast population. Macroscopically, the cores show a relatively constant or even a slightly coarsening upward trend in the interval between cores 53_3 and 49_1 (~659–643 mbsf). Midway through core 48_2 at ~642 mbsf, another clear decrease in clast size is visible in thin sections and the halfcore photographs (Figs. 8C and 14D). From this depth regime upwards, the suevite becomes increasingly finer and more well-sorted and shows a higher proportion of groundmass and vitric melt clasts than the rest of the graded suevite unit.

The average whole-rock geochemical composition of the graded suevite unit shows quite constant values with depth, although the variability in the lower portion of this unit is rather high due to the coarse clast size. This lower, coarse-grained interval (~710–680 mbsf) is characterized by highly variable SiO_2 (8–71 wt%, on average, 46 wt%), highly variable CaO (3–86 wt%, on average, 24 wt%), and relatively low K_2O values (0.2–4.4 wt%, on average, 1.9 wt%), although K_2O concentrations start to increase again from ~690 mbsf upwards (Fig. 12C). The major element composition in the depth interval at ~680–621 mbsf is less variable and dominated by relatively high SiO_2 (38–59 wt%, on average, 48.4 wt%), high K_2O (2.3–4.7 wt%, on average, 2.8 wt%), and low CaO (12–32 wt%, on average, 20.7 wt%) values (Table 1; Fig. 12). The trace element concentrations of the graded suevite unit show intermediate values for the LREEs (~40 times CI chondrite) and the HREEs (~13 times CI chondrite), and the enrichment in Sr (~60 times CI chondritic values) is less pronounced than in the non-graded suevite unit (Fig. 13).

Bedded Suevite Unit (620.88–617.33 mbsf)

The bedded suevite unit is a ~3.5-m-thick unit (Fig. 8B; from core level 41_2_13 to 40_1_109) that forms the top of the M0077A suevite sequence. Macroscopically, this unit is classified as a fine-grained, both groundmass- and clast-supported, very well-sorted suevite. A main difference from the underlying graded suevite unit is the distinct bedding of this unit (Fig. 8B) as observed both macroscopically and microscopically. The boundary is placed in the top part of core 41_2 and corresponds with a change in color in the halfcore photograph from a blue-gray color to a more brownish color (Fig. S4). This is possibly linked to the increase in bulk CaO and enhanced cementation in this unit. At 620.88 mbsf, three independent geophysical parameters show an upward trend, with seismic velocity that increases from ~2600–4200 m/s (Fig. 14B), bulk density that increases from ~2.0–2.3 g/cm^3, and porosity that decreases from ~36% to 24% (Christeson et al., 2018). The first thin section that shows clear bedding features is sample 41_1_104_109 (620.34 mbsf). This sample also contains the impact spherule shown in Figure 9.

The bedded suevite unit yields a paleomagnetic signal that is consistent with the ~-46° reported for the non-graded suevite unit and underlying impact melt rock units (Fig. 14C). This signal suggests the bedded suevite unit was formed and deposited during magnetic chron 29r or may reflect the observation that most clasts in the unit are vitric melt clasts, which are interpreted to be quenched melt that should have preserved the same signal as the impact melt rock unit at the base of the impactite sequence.

The vitric melt clasts are the most common clast group in this unit, and there is a small fraction of primary carbonate clasts, silica mineral clasts, felsic basement clasts, and microcrystalline melt clasts. Geochemically, the bedded suevite unit shows a gradual increase in CaO toward the top (28–57 wt%, on average, 40 wt%) and yields low Al_2O_3 (3.9–10.8 wt%), low SiO_2 (15–46 wt%), and low Fe_2O_3 (1.0–8.5 wt%, on average, 3.8 wt%) values compared to the other suevite units (Table 1; Fig. 11). This geochemical signature is indicative of enhanced cementation of this suevite unit. Regarding the trace elements (Fig. 12), the bedded suevite unit has the highest Sr enrichment of all suevite units (106 times CI chondrite values), but it shows both depleted LREE and HREE patterns similar to those of the non-graded suevite unit.

The upper boundary with the transitional unit at 617.33 mbsf is a sharp, stylolitized contact that coincides with a clear drop in grain-size and increase in bulk CaO and MnO abundances. Compared to the transitional unit, the bedded suevite unit is rich in almost all other major elements (e.g., Al, Si, K, and Ti), trace elements (Sr, Rb, Zr, Br, and Ba), and both LREEs and HREEs (Fig. 12).

Petrographic and Geochemical Fingerprinting of the Chicxulub Target Lithologies

The petrographic and geochemical identification of clast types in the M0077A suevite sequence highlights the variability in Chicxulub target lithologies. The extensive geochemical database presented in this study can be summarized in the two ternary diagrams of Figure 15 that display the $Na_2O + K_2O$, $Fe_2O_3^T + MgO$ and CaO variations based on whole-rock analyses (Fig. 15A) and phase-specific analyses (Fig. 15B) complemented with literature data from drill cores M0077A (Units 3 and 4) and Y6. These three geochemical end-members represent the most important Yucatán target lithology groups that constitute the composition of the majority of the Chicxulub impactites: felsic granitoids, mafic dolerites, and carbonates (Kettrup and Deutsch, 2003; de Graaff et al., 2021).

In general, the three suevite units, the upper impact melt rock unit (UIM, after de Graaff et al., 2021), and the lower impact melt rock-bearing unit (LIMB, after de Graaff et al., 2021), show all a relatively constant ratio of $Na_2O + K_2O$ / $Fe_2O_3^T + MgO$. The largest whole-rock variations are caused by differences in the CaO concentrations (Fig. 15A). This suggests that the same types of components are present in all of the impactite units with the exception of the carbonate components in the lower impact melt rock-bearing unit. The common component in all these units is silicate impact melt (possibly as melt particles), and their original composition is a mixture of primarily felsic and mafic components with a small fraction of carbonate (<10 wt% CaO; de Graaff et al., 2021). The CaO dilution is mostly caused by the incorporation of carbonate clasts, cementation features of the groundmass, and/or the occurrence of sparry calcite related to post-impact, CaO-rich fluids flowing through the impactite sequence. The latter explains the large whole-rock CaO variations seen in the upper impact melt rock unit, in which higher values are linked to impact melt rock samples enriched in green schlieren. The graded suevite unit displays chemical compositions with intermediate CaO values despite the scattered values (3.2–49.6 wt%) from samples from the lower part of this unit (~710–680 mbsf) that are caused by the larger clast sizes. The non-graded and bedded suevite units are significantly more enriched in CaO (Table 1 and Fig. 15). These latter two units can be distinguished from each other based on a slightly more mafic ($Fe_2O_3^T + MgO$) contribution in the non-graded suevite unit, which is also seen in the EMPA-based groundmass compositions of both units (Table 1 and Fig. 15B).

The major element chemical variations of the suevite clasts largely follow the patterns of the M0077A whole-rock analyses and literature values from Y6 (Fig. 15B) (Kettrup and Deutsch, 2003; de Graaff et al., 2021). The target rock clasts are interpreted as shocked, brecciated, and comminuted parts of the target stratigraphy that were transported and incorporated into the suevite assemblage. The granitoid and gneiss clasts display mostly felsic compositions but also some alteration linked to phyllosilicates (rich in $Fe_2O_3^T + MgO$) and calcite infill structures. The compositions of the M0077A dolerite clasts plot close to the whole-rock values for doleritic dikes found within the granitoid basement of the M0077A core (de Graaff et al., 2021). The M0077A amphibolite clast compositions also plot close to this field and close to the

Downloaded from http://pubs.geoscienceworld.org/gsa/gsabulletin/article-pdf/doi/10.1130/B36020.1/5365526/b36020.pdf
by Arizona State University user

only known reference value for Chicxulub amphibolite clasts, which was identified within the Y6 core (Kettrup and Deutsch, 2003). The silica mineral clasts show a more scattered geochemical pattern, although this is strongly biased by the high (>99 wt%) SiO_2 values.

As expected, the primary and reacted carbonate clasts have consistently high CaO values (Fig. 15B). The primary carbonate clasts within the M0077A suevite were most probably transported into their present location from original locations that were not subjected to thermal processing during compression and crater excavation (Wittmann, 2020). This is in contrast to the reacted carbonate clasts, which record impact-related thermal processing of carbonate and sulfate target rocks. These target lithologies decomposed and subsequently back-reacted to microcrystalline calcite while also affecting the surrounding suevite groundmass. The presence of these reacted carbonate clasts inside both the non-graded and the graded suevite units but not in the bedded suevite unit (Fig. 10B) indicates immediate rapid deposition until ~621 mbsf (Wittmann, 2020). The bedded suevite unit may have undergone extended reworking because the carbonation reaction of carbonate clasts in this interval did not affect the suevite groundmass.

The vitric melt clasts are interpreted to be impact melt particles that were quickly quenched, in a matter of minutes from >1200 °C to <650 °C, preventing the crystallization of phenocrysts (Engelhardt et al., 1995). They show a cluster of values even more mafic than those of the dolerites. This is either due to severe devitrification and secondary alteration of the glass into Fe-Mg-rich (often smectitic) clays, as had been described for these clasts in the M0077A core by Simpson et al. (2020), or to a lithological component that is still unsampled. The values presented here are produced by μXRF mapping of complete clasts, which would incorporate large fractions of the smectitic alteration rim but also excite the clast area just below the surface. More targeted, phase-specific analyses (e.g., analyses by means of EMPA or Laser Ablation-ICP-MS) are needed to verify the vitric melt clast composition and to better understand the nature and formational mechanisms of these melt products.

The composition of the microcrystalline melt clasts is considered more pristine, as plagioclase microlites are often preserved in the melt microtexture, which would imply a slower cooling process than that of the vitric melt clasts (Engelhardt et al., 1995). However, secondary phyllosilicates have also been observed in the microcrystalline melt clasts (this study and Simpson et al., 2020). The microcrystalline melt clast compositions presented here show a wide variation from felsic compositions to more CaO-enriched values.

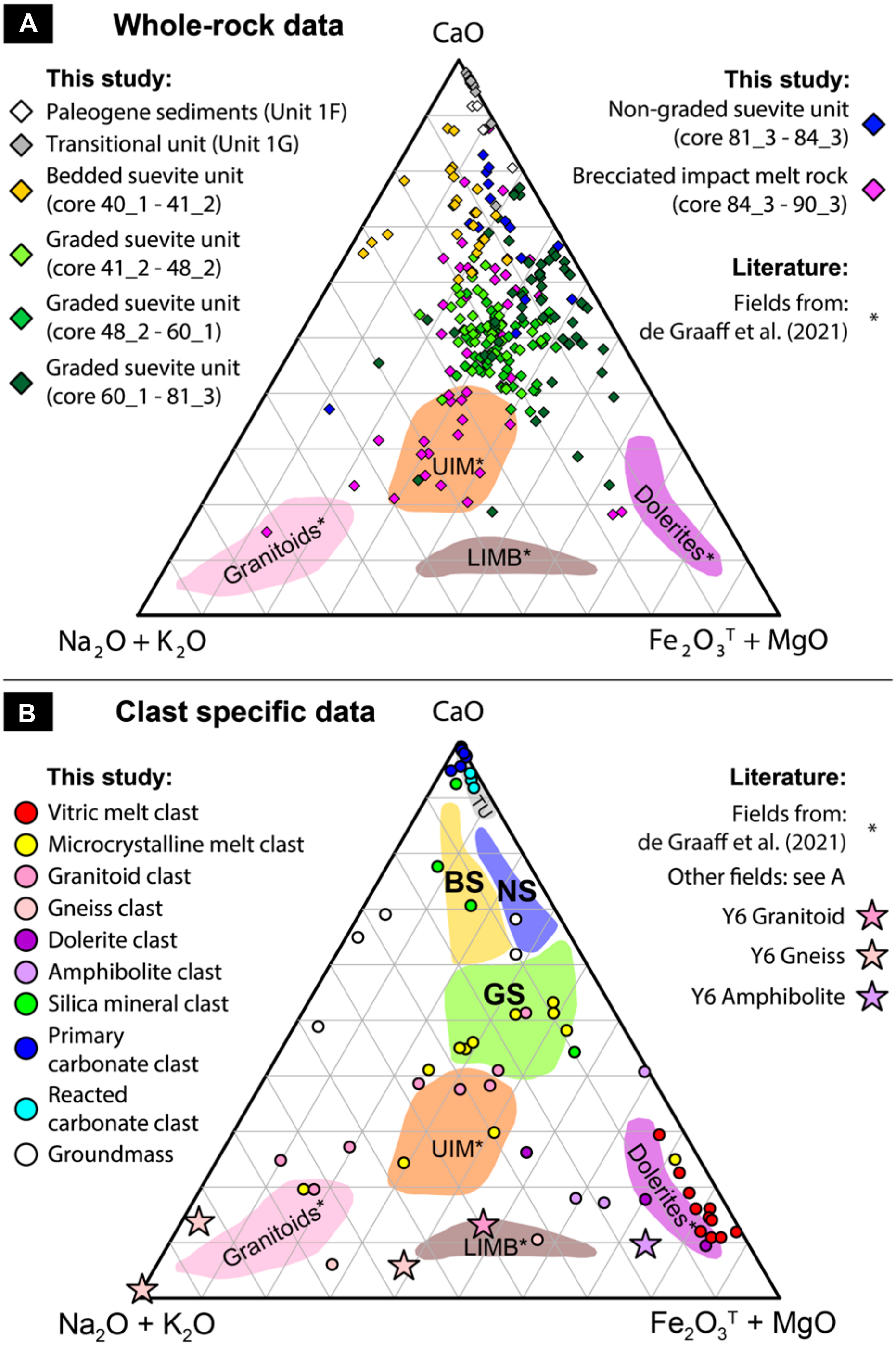

Figure 15. Ternary $Na_2O + K_2O$–$Fe_2O_3^T + MgO$–CaO diagrams for Chicxulub impactites and target rock material. (A) Whole-rock values for the different M0077A suevite and adjacent units based on bulk X-ray fluorescence (XRF), inductively coupled plasma-optical emission mass spectrometry (ICP-OES), and micro-X-ray fluorescence (μXRF). M0077A data fields of the upper impact melt rock unit (UIM), the lower impact melt rock-bearing unit (LIMB), granitoid basement, and dolerite dikes are derived from de Graaff et al. (2021). (B) Clast-specific geochemical data of M0077A suevite components based on μXRF. The data fields of the non-graded suevite unit (NS), graded suevite unit (GS), bedded suevite unit (BS), and transitional unit (TU) are drawn based on the majority of the data points from Figure 15A. Geochemistry of target lithology clasts from the Y6 core is shown for comparison (from Kettrup and Deutsch, 2003).

Downloaded from http://pubs.geoscienceworld.org/gsa/gsabulletin/article-pdf/doi/10.1130/B36020.1/5365526/b36020.pdf
by Arizona State University user

Although the observed variations reflect the variable degree of alteration, the range in values is not as limited as for the vitric melt clasts, and as such we interpret the values for microcrystalline melt clasts to be representative of their initial variations in composition. Therefore, the chemistry of the latter clast group corresponds largely to the original black upper impact melt rock composition (UIM field in Fig. 15A; de Graaff et al., 2021). Chemical variations in the microcrystalline melt clasts are caused primarily by the number, size, and type of entrained crystalline basement clasts and to a lesser degree to hydrothermal alteration (Fig. 15B). We interpret the microcrystalline melt clasts as brecciated and reworked parts from underlying impact melt flows.

Hydrothermal alteration can influence a clast type identification that is based on visual macroscopic properties such as color. Based on granulometric line logging of M0077A halfcore photographs, Ormö et al. (2021) recognized 17 different suevite clast groups, including six different melt clasts of varying colors, a red-orange quartzite clast type, and a red siltstone clast-type. These last two groups have not been identified in this study based on both petrography and μXRF element mapping. Our findings suggest that a siliciclastic sedimentary component, besides the pure silica mineral clasts, is absent in the M0077A core and potentially in this part of the Chicxulub basin. To date, siliciclastic sedimentary components have only been confirmed from drill cores Y1 and Y4 outside of the Chicxulub crater, which lie 150–200 km south and east of the crater center (Koeberl, 1993). Hence, this comparison highlights the importance of a solid petrographic and geochemical analysis on drill core material before conclusions can be drawn about the presence and stratigraphic variation in impactite components based on macroscopic descriptions.

Furthermore, the suevite sequence is devoid of evaporite sulfate minerals such as anhydrite and gypsum. This was already pointed out by Gulick et al. (2019) and is confirmed by the extensive petrographic analysis presented in this study. The μXRF-based, more extended whole-rock sulfur database presented here (Fig. S7C) also follows the trends presented in Gulick et al. (2017, 2019), with low values (<0.7 wt%) throughout the sequence. The higher S values (up to 8 wt%, but generally <1 wt%) are attributed to intervals with more secondary pyrite and other sulfides and not to any contribution of sulfate evaporites. The apparent absence of these evaporite sulfate minerals in the M0077A core has been interpreted to be due to preferential shock vaporization of evaporites during the excavation stage or to the preferential fracturing of evaporites into larger fragments than carbonates, which results in ejection and deposition of those outside of the peak-ring zone (Gulick et al., 2019).

Emplacement of the Suevite Units

The new classification of the M0077A suevite sequence into three units is the basis for a refined emplacement model of proximal Chicxulub impactites. In the paragraphs below, we link the main observations per suevite unit with an interpretation of the related depositional processes versus (relative) timing and compare these with previous interpretations of the sequence. The buildup of the M0077A suevite succession reflects a decreasing level of energy in the sedimentary system of this crater peak-ring region over time, as is illustrated in the model snapshots of Figure 16.

Non-Graded Suevite Unit and Underlying Impact Melt Rock

During the contact and compression phase, the Chicxulub impactor hit Yucatán following a steeply inclined trajectory from the northeast and generated a shock wave that caused intense compression, vaporization, melting, and brecciation of the target lithologies (Collins et al., 2020). Rarefaction waves following the shock wave initiated an excavation flow that opened a transient cavity and ejected the vaporized, melted, and brecciated target components in a timespan of <1 min (Fig. 16A; Morgan et al., 2016; Riller et al., 2018). This ejected material comprised both solid and melted material (Smit, 1999) and included impact spherules ejected from the crater such as the specimen that was eventually found higher up in the sequence in the bedded suevite unit (Fig. 9). de Graaff et al. (2021) also suggested that during this excavation stage, multiple melt injections took place in the shocked crystalline basement based on the presence of cryptocrystalline and holohyaline impact melt particles and a bulk composition devoid of a carbonate component. These melt injections eventually formed the lower impact melt rock-bearing unit (Fig. 2A) in the M0077A core, as comminution of this melt unit occurred in the early phases of the modification stage (de Graaff et al., 2021).

After the excavation stage, the central part of the transient cavity underwent rapid uplift and subsequent gravitational collapse, which resulted in lateral movement of crustal and impactite material and the formation of a peak ring (Fig. 16B; e.g., Morgan et al., 2016; Riller et al., 2018; Rae et al., 2019). During this modification stage, a ~30-m-thick coherent impact melt sheet was emplaced at Site M0077 that draped the top of the irregular peak ring, which is composed of shocked granitoid basement rock. This melt represents the upper impact melt rock unit, as described by de Graaff et al. (2021), combined with an overlying ~6-m-thick, clast-rich impact melt rock unit. This ~6-m-thick interval consists of abundant clasts of both felsic basement and recrystallized carbonates. Gulick et al. (2019) described a scenario for the emplacement of their Unit 3A-B and 2C (747.02–712.83 mbsf) involving outward-flowing melt and density currents carrying clasts of impact melt rock. These impactoclastic melt flows might have transported the carbonate clasts on top of the peak ring, but as the temperatures were not high enough (<840 °C), the entrained carbonates did not fully melt near the top of the unit (de Graaff et al., 2021) and only recrystallized.

As the Yucatán area was a marine environment upon impact, ocean water from the Gulf of Mexico region was able to flow back into the crater rapidly after the initial proximal vaporization of water and target rock at the impact site and after the formation of outward-moving tsunami waves across the Gulf of Mexico (e.g., Smit et al., 1996; Gulick et al., 2019). Seismic studies showed that the morphology of the Chicxulub structure is slightly asymmetric with a large gap in the inner rim toward the north-northeast, which is interpreted to be connected to the Gulf of Mexico, which had water depths of ~2 km (Fig. 1A; Gulick et al., 2008). This ocean region may be the source area from where the first sea water entered the Chicxulub crater after impact (Gulick et al., 2019). This caused flooding of the crater depression from the north, and this event is recorded on the northwestern peak-ring in the M0077A core in unprecedented detail. When the sea water rushed back into the crater (Fig. 16C), at <30 min post impact as estimated based on a simplified one-dimensional "dam-break" model (Gulick et al., 2019), this water came into contact with coherent hot impact melt, which caused abundant melt-water (phreatomagmatic) interactions (Gulick et al., 2019; Osinski et al., 2020), massive steam development, and quench fragmentation of impact melt (Fig. 16C). The green schlieren textures present in the impact melt rock between 737.56–715.60 mbsf are most probably remnants of these brecciated parts of the impact melt rock that were later on replaced by sparry calcite due to the percolating ocean water and associated hydrothermal alteration (Kring et al., 2020). As the schlieren disappear at the boundary of Units 3A and 3B, we conclude that melt brecciation and percolating ocean water did not penetrate deeper than 737.56 mbsf at this location inside the crater. This model agrees with the timing and processes of the final stages of the upper impact melt rock emplacement presented in de Graaff et al. (2021) and Gulick et al. (2019).

Downloaded from http://pubs.geoscienceworld.org/gsa/gsabulletin/article-pdf/doi/10.1130/B36020.1/5365526/b36020.pdf
by Arizona State University user

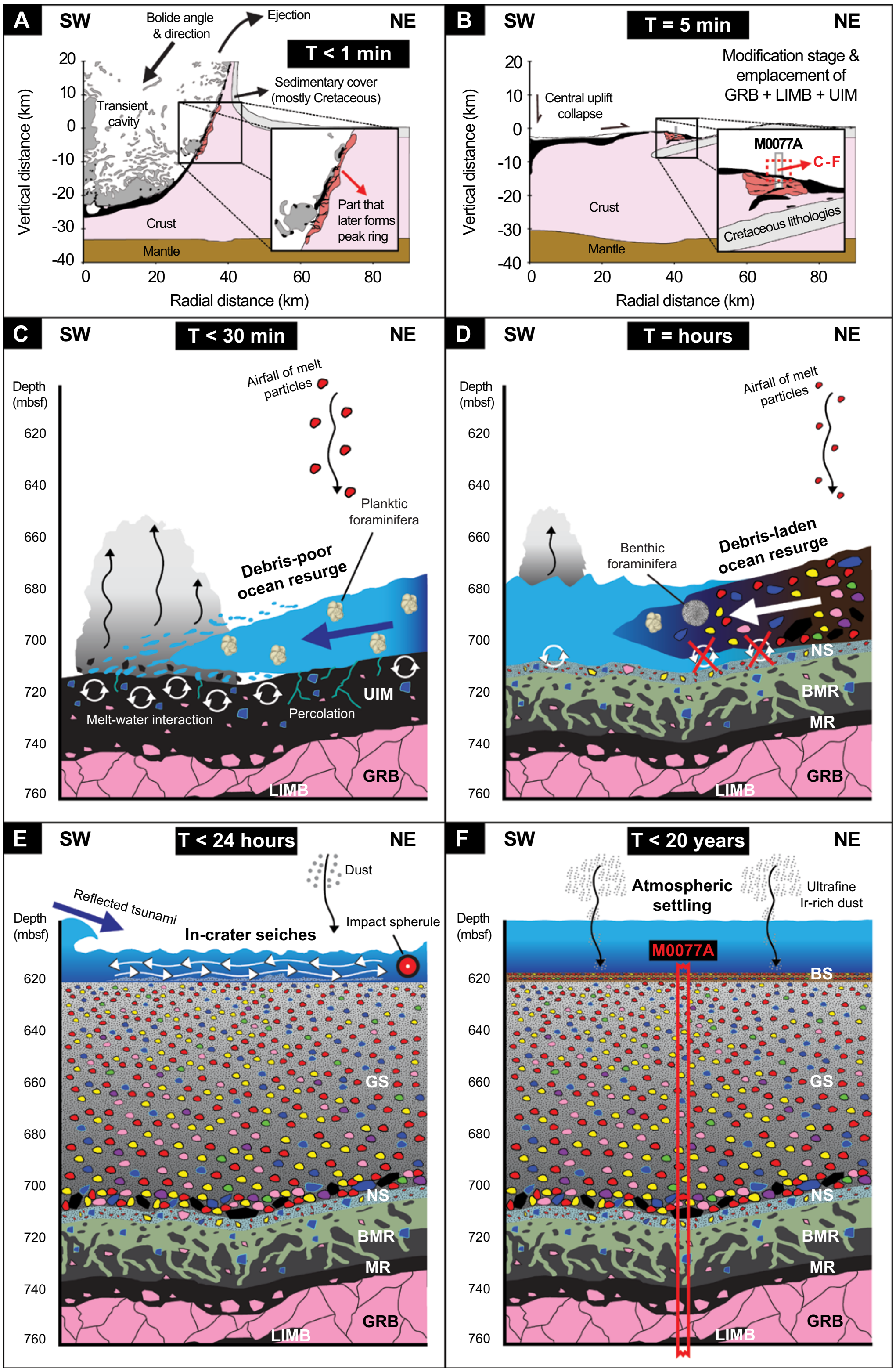

Figure 16. Schematic visualization with key moments in the emplacement of the Chicxulub M0077A suevite sequence and adjacent units. (A) Excavation stage <1 min after the bolide impact, highlighting shock-based brecciation, melting, and vaporization inside the transient cavity and ejection of target rock material from the crater (e.g., Morgan et al., 2016; Collins et al., 2020). (B) After the excavation stage, central uplift occurs with subsequent collapse and peak ring formation (e.g., Morgan et al., 2016; Riller et al., 2018). On this peak ring, granitoid basement (GRB) is emplaced with an injected lower impact melt rock-bearing unit (LIMB) and an upper melt rock unit (UIM) draped on top (following de Graaff et al., 2021). Zoomed-in snapshots of the peak ring location of the M0077A core are highlighted in C–F. (C) Upper peak ring situation <30 min after impact shows the first arrival of debris-poor sea water through a N-NE gap in the crater rim. This ocean water percolates in the coherent hot melt sheet and causes intense quench fragmentation. This results in the brecciation of the upper part of the melt sheet, displayed as green schlieren textures in this unit, and the emplacement of the ~5.6-m-thick, non-graded suevite unit (NS). (D) In the following hours, the crater is being continuously flooded by an ocean resurge rich in rock debris, which ceases the phreatomagmatic processes and forms the ~89-m-thick graded suevite unit (GS). (E) After the energy of the resurge slowly dissipates within the crater, oscillating seiche waves take over the sedimentary regime and form the ~3.5-m-thick reworked bedded suevite unit (BS). Within this unit, a rare impact spherule (Fig. 9) is preserved, which was initially ejected and then flowed back into the crater in the final stage of the ocean resurge. At the top of the bedded suevite unit, a cross-bedded interval is visible, which is linked to the return of a reflected tsunami coming from the nearest landmass. Based on modeling, this return wave is estimated to have arrived in the peak ring region within 24 h after impact (Sanford et al., 2016; Gulick et al., 2019). (F) The final stage of the M0077A impactite sequence is characterized by the deposition of the ~75-cm-thick, fine-grained transitional unit, steered by re-suspension and slow settling. This unit is capped by a 3-cm-thick green marlstone, which yields a positive iridium anomaly. This is indicative of the final atmospheric settling of Chicxulub impactor debris, which is interpreted to have happened within 20 years after impact (Goderis et al., 2021). The color of the clasts within the suevite units corresponds to Figures 10 and S1 (see footnote 1).

Downloaded from http://pubs.geoscienceworld.org/gsa/gsabulletin/article-pdf/doi/10.1130/B36020.1/5365526/b36020.pdf
by Arizona State University user

Following the model mentioned above, the first sea water that rapidly entered the crater <30 min after impact (as highlighted at a depth of ~715.60 mbsf, which represents the base of the non-graded suevite unit; Fig. S2) was most probably depleted in rock debris. The high abundance of isolated planktic foraminifera in the clastic groundmass of the non-graded suevite unit suggests that this incoming sea water most likely ripped up large amounts of uncemented material from the seabed. This material most probably consisted of calcareous ooze rich in planktic foraminifera and not in benthic foraminifera, which may be indicative of the deeper water conditions to the N-NE of the Chicxulub structure. The low quantities of exotic clasts in this unit also suggests that the primary clast components (such as melt particles and carbonate clasts) of the non-graded suevite unit were mostly locally derived on top of the hot impact melt sheet. The abundant vitric melt clasts suggest rapid quenching that was probably caused by a hot impact melt body cooled from the top. The microcrystalline melt clasts most probably derived directly from the impact melt rock unit below, based on comparable microtextures and geochemistry, and were incorporated into the suevite unit as brecciated fragments of impact melt rock. The carbonate clasts in this unit could either have been transported by the first ocean water influx or they represent ripped up carbonate clasts that were entrained in the underlying impact melt.

Both the upper impact melt rock and the non-graded suevite unit show a consistent magnetic inclination of ~-46° (Fig. 14B). This implies that these lithologies were emplaced rapidly and maintained temperatures above the Curie temperature of magnetite (580 °C) for at least a short period of time (Gulick et al., 2019). This short duration of high temperatures may be the reason why the planktic foraminifera in the groundmass of the non-graded suevite unit are partly recrystallized. Importantly, these recrystallization features of the foraminifera have not been identified in the other suevite units.

Based on the paleomagnetic data, in combination with the petrographic characteristics stated above, we suggest that the non-graded suevite unit was emplaced following processes similar to those of a primary hyaloclastite breccia deposit (Watton et al., 2013). Hyaloclastite deposits are normally known from submarine or subglacial volcanoes when magma interacts with water and are characterized by a poorly sorted, groundmass-supported unit enriched in quenched glassy fragments (Greenfield et al., 2020), which is the case for the non-graded suevite unit (Fig. 10E and 11B).

Alternatively, Osinski et al. (2020) considered that Unit 2C (712.83–721.62 mbsf) represents a contact zone between the impact melt rock of Unit 3 (721.62–747.02 mbsf) and the overlying product (>712.83 mbsf) of highly energetic molten fuel-coolant interaction. This last mechanism is to a degree equivalent to the melt-water interaction, hyaloclastite-like interpretation we propose for the formation of the non-graded suevite unit. However, Osinski et al. (2020) also state that these phreatomagmatic deposits are well-sorted, which does not agree with the poorly sorted nature of the non-graded suevite unit (Fig. 11B).

Graded Suevite Unit

The petrographic, geochemical, and paleomagnetic change observed at ~710 mbsf (Figs. 14 and S3) corresponds to the onset of the ~89-m-thick graded suevite unit. From this depth upwards there is a gradational fining and increased sorting visible up to ~621 mbsf. The wide spread in magnetic inclination values (Fig. 14C) suggests that the incorporated target rock clasts inside the graded suevite unit were most probably transported from outside the peak ring region as they reflect a diverse population of target lithologies (López-Ramos, 1975; Kring, 2005). The relatively constant bulk major and trace element compositions and modal clast group distributions throughout the graded suevite unit (e.g., Figs. 10, 12, 13, and 14A) also indicate the mixing of a wide range of similar components throughout this part of the suevite sequence. Compared to the non-graded suevite unit, this ~89-m-thick interval also displays lower seismic velocity (Fig. 14B), lower density, and a higher porosity, which implies rapid deposition and limited cementation.

Hence, we interpret the graded suevite unit to have been deposited by a forceful event that occurred in the crater rapidly after impact and showed a decrease in energy level over time. A powerful ocean resurge into the Chicxulub crater as depositional mechanism is a likely scenario in this case, as the sea water that rushed back into the crater acted as an efficient sorting agent (Gulick et al., 2019). This emplacement model has also been suggested for a ~60-m-thick deposit in the ~14-km-sized marine-target Lockne impact crater in Sweden that shows a fining upward and a more well-sorted upward trend (Ormö et al., 2007).

In addition, the late Eocene Chesapeake Bay impact structure in southeastern Virginia (USA) may be an interesting candidate to compare with the Chicxulub M0077A impactite sequence, as the Chesapeake Bay structure, with a diameter of ~85 km, is the largest marine target crater known so far on Earth after Chicxulub and potentially Sudbury (Gohn et al., 2008; Grieve et al., 2010; Vermeesch and Morgan, 2008). In 2006, ICDP and USGS extracted two continuous drill cores (Eyreville A and B) from the annular moat that lies ~9 km to the NE of the center of the Chesapeake Bay structure. The 1766-m-thick recovered section consists (from base to top) of: basement-derived blocks of crystalline rocks (215 m); a section of suevite, impact melt rock, lithic impact breccia, and cataclasites (154 m); a thin interval of quartz sand and lithic blocks (26 m); a granite megablock (275 m); and a complex breccia interval known as the Exmore bed section (652 m) that is followed by post-impact Eocene to Pleistocene sediments (444 m) (Gohn et al., 2008). The Exmore bed section is composed of sediment blocks and boulders at the base; polymict, sediment-clast dominated breccias with rare impact melt particles in the middle part; and a thin upper section of stratified sediments (Gohn et al., 2008; Edwards et al., 2009; Dypvik et al., 2018). The upper 30 m of this Exmore breccia sequence may show similarities to the graded and bedded suevite unit from M0077A, as Ormö et al. (2009) found a fining-upward sequence based on granulometric line-logging and concluded that there was evidence for potentially multiple ocean resurge pulses as well as a transition into oscillating resurge (i.e., seiches). Reimold et al. (2009) and Dypvik et al. (2018) reported rare planktic foraminifera in the fine-grained groundmass of this graded part of the Exmore beds, which is indicative of marine (reworking) processes. However, they also found two distinct zones enriched in sub-millimeter impact melt shards in the generally melt-poor graded sequence (Reimold et al., 2009), which is not a feature of the more homogeneous, more melt-rich, and coarser-grained M0077A graded suevite. The uppermost stratified member of the Exmore beds consists of sandstone and laminated siltstone and claystone (Edwards et al., 2009) and may have been deposited as the result of oscillating in-crater seiches followed by suspension (Ormö et al., 2009; Dypvik et al., 2018). However, this stratified member is not enriched in CaO (Schmitt et al., 2009) in comparison to the underlying graded unit, as we observed in the M0077A bedded suevite unit. The different positions within the crater of the Eyreville cores (annular moat) versus the M0077A core (peak ring), together with variations in target stratigraphy and paleo water depths, are most probably key in explaining these main lithological variations. However, a more in-depth, crater-wide study of both crater fill records is needed to better understand the differences and similarities in large-scale marine impact processes between Chicxulub and Chesapeake Bay.

Whereas the deposition of the non-graded suevite unit in the M0077A core is linked to

Downloaded from http://pubs.geoscienceworld.org/gsa/gsabulletin/article-pdf/doi/10.1130/B36020.1/5365526/b36020.pdf
by Arizona State University user

the resurge of debris-poor ocean water, the ocean water related to the deposition of the graded suevite unit transported much rock debris (Fig. 16D), probably due to the settling and subsequent turbulent mixing of proximal ejecta in a slightly later stage than the initial sea water ingress. This change in sedimentary regime can be inferred from the wide variety in clast types in this unit and the nature of the basal part of the graded suevite unit, which is clast-supported and shows the presence of up to 0.9-m-thick impact melt rock clasts (Fig. 16E).

Gulick et al. (2019) suggested that the anomalously low seismic velocities encountered in the depth interval 706–697 mbsf were caused by flooding of the peak ring by ocean resurge. However, we interpret that the arrival of a debris-rich resurge had already taken place at 710 mbsf based on the petrographic, geochemical, and paleomagnetic changes at this depth. This lowermost part of the graded suevite unit (~710–705 mbsf: cores 81 and 80) shows some elevated seismic velocity values, but we attribute these peaks directly to the presence of thick and dense impact melt rock bodies inside this part of the suevite.

The sudden influx of debris-laden ocean water most probably stopped the growth of a large phreatomagmatic system that was initiated on top of the upper melt rock sequence for a short period of time (Fig. 16D). With the increasing water volume on the peak ring during this phase, the magma-water ratio was no longer sufficiently high enough to sustain phreatomagmatic activity (Németh and Kósik, 2020). This suggestion of short-lived melt-water interactions is in line with the sequence of events proposed in Gulick et al. (2019) but differs from the model of Osinski et al. (2020), which suggests that phreatomagmatic processes were responsible for the deposition of Unit 2B (712.83–664.52 mbsf) and the majority of Unit 2A (664.52–617.33 mbsf).

The vitric melt clasts are the most abundant clast types throughout the suevite sequence, but microcrystalline melt clasts are found throughout the suevite interval as well. This shows that from 710 mbsf and up, these melt rock particles were brought in from elsewhere by ocean resurge rather than from phreatomagmatic processes on the peak-ring as proposed by Osinski et al. (2020). The microcrystalline melt clasts and large vitric melt clasts in the graded suevite unit were probably ejected as part of the proximal ejecta curtain during the excavation stage (Fig. 16A) and then transported back into the crater by the surging ocean. Small vitric melt clasts are either fragmented larger vitric melt clasts that were ejected or produced during the brief phreatomagmatic phase, or they are light melt particles that stayed longer in the atmosphere and fell back in a later stage of the resurge. In addition, the presence but overall low abundance of shock metamorphic features throughout the suevite sequence (e.g., PDFs in quartz) may be explained by the dilution effect of a large ocean resurge event that brings in a wide range of unshocked material from different parts within and outside of the transient crater cavity.

Based on a one-dimensional “dam-break” flooding model, Gulick et al. (2019) estimated that the flooding of the crater up to the depth of the peak ring (estimated at 500 m above the crater floor) took from ~30 min to 1 h. This timing corresponds to the deposition of the complete non-graded suevite unit and the lower clast-supported part of the graded suevite unit (Figs. 16C–16D). The remaining part of the graded suevite unit was likely deposited in the following hours due to settling of the clasts out of the water column. Superimposed on the general fining-upward trend of the graded suevite unit are some smaller-scale trends that could indicate slight changes in the energy level of the sedimentary system. For instance, between cores 55_3 and 53_1 (~665–656 mbsf), an abrupt fining-upward sequence changes into a coarsening-upward trend. We interpret these small offsets as minor slumping events that occurred inside the small depression on the peak ring while the resurge in the crater continued. These mass wasting events could be triggered by post-impact earthquakes remobilizing coarser material already deposited on the higher topographic areas of the Chicxulub peak ring. In core 48_2 (~642 mbsf), a general drop in clast-size is apparent, both on the half-core photographs (Fig. 14D) and in thin sections. The thin sections also show a more well-sorted behavior (Fig. 11) that increases toward the top of the unit. We interpret this unit to still be part of the ocean resurge, but the energy is clearly decreasing while the peak ring region is continuously submerged. Approximately 25 normally graded beds observed in CT core scan data between 627 mbsf and 617.34 mbsf (the top part of the graded suevite unit together with the bedded suevite unit) support this interpretation (Gulick et al., 2019).

Bedded Suevite Unit and Transitional Unit

The transition from core 41_2 to 41_1 (at 620.88 mbsf; Fig. S4) corresponds with well-developed bedding, an increase in bulk CaO content, an increase in seismic velocity, an increase in bulk density, and a decrease in porosity (Fig. 14; Christeson et al., 2018), all of which are indicative of a better-cemented unit and a more prolonged depositional mechanism than is interpreted for the underlying impactite intervals. The bedded suevite unit contains levels depleted or enriched in vitric melt clasts and isolated planktic and benthic foraminifera, which suggests water movements that washed up, brought together, but also winnowed down the various suevite components (Fig. 16E). This reworking can be caused by repetitive hydrodynamic processes, which, in an impact cratering context, may be interpreted to be triggered by in-crater seiches (Smit et al., 1996; Gulick et al., 2019). There is a general consensus (Gulick et al., 2019; Whalen et al., 2020) that the top part of the M0077A suevite was deposited by means of seiche waves; however, the exact moment when the sedimentary regime within the crater transitioned from resurge to seiche is still poorly constrained. Here, we interpret that the transition at 620.88 mbsf marks the end of the resurge deposit in the M0077A core and represents the onset of oscillating seiche waves within the Chicxulub crater after its initial flooding.

In the basal part of the bedded suevite unit (41_1_105_109; 620.34 mbsf), a unique silicate, glassy, 1.2-mm-diameter impact spherule was identified (Fig. 9). Morphologically, this spherule is well-preserved (Figs. 9A–9C) and resembles well-known impact glass spherules from the proximal K-Pg sites of Beloc in Haiti or El Mimbral in NE México (e.g., Smit, 1999; Belza et al., 2015). However, the primary silicate impact melt composition is altered to palagonite and a phyllosilicate smectite phase (Figs. 9D–9F). Such impact spherules have not been encountered in any other stratigraphic position within the M0077A core and have also not been reported, as far as we are aware, from elsewhere within the Chicxulub crater either. However, similar impact spherules have been reported to occur within the Ries structure (Graup, 1981) and in reworked upper suevite units within the Bosumtwi (Koeberl et al., 2007) and El’gygytgyn impact craters (Wittmann et al., 2013). Therefore, we interpret this spherule to represent a melt droplet that was quenched and ejected from the crater into the proximal Gulf of Mexico region within the first minutes after the impact (Fig. 16A). It was then brought back in the final stage of the resurge into the crater and became part of the movement of the first seiches (Fig. 16E). Eventually it settled as part of one of the first layers within the bedded suevite unit within a few hours after the impact. Although more spherules may be expected to have been brought back into the crater, the admixture and dilution with other clasts most probably inhibits our ability to find more of these spherules inside the graded suevite. Alternatively, most of these delicate glassy spherules could also be fractured due to the force of the powerful resurge event and are currently indistinguishable from vitric melt clasts. The first seiche layers may reveal more preserved Chicxulub spherules. A more

Downloaded from http://pubs.geoscienceworld.org/gsa/gsabulletin/article-pdf/doi/10.1130/B36020.1/5365526/b36020.pdf
by Arizona State University user

in-depth spherule study is needed to unravel the mechanisms and timing of these impact melt processes and subsequent deposition.

The uppermost 20 cm of the bedded suevite unit (617.53–617.33 mbsf) is characterized by a cross-bedded nature of more coarse-grained, sand- to fine gravel-sized material, which implies more rapid sedimentation. In addition, vertical sedimentary structures have been found in this top part (Fig. 2C) that have been interpreted as either dewatering pipes or fluid and vapor channels that are associated with the hydrothermal system (Gulick et al., 2019; Kring et al., 2020). Such features are commonly observed in density current deposits or turbidites and indicate high energetic conditions (Gulick et al., 2019). This interval also coincides with an apparent increase in terrestrial biomarkers (such as polycyclic aromatic hydrocarbons) and charcoal particles (Gulick et al., 2019). Their presence has been interpreted to be indicative of the return of a tsunami that was reflected from the nearest continental landmass, most probably the central Mexican highlands at 800 km W-SW of the newly formed crater (Gulick et al., 2019). Based on extensive mapping of the K-Pg boundary deposit in the Gulf of Mexico based on seismic and borehole data, Sanford et al. (2016) modeled the post-impact megatsunami travel times in the region to the north of the Chicxulub crater. The first arrival time of tsunami waves at the paleo-Florida and paleo-Texas coasts was estimated to be within 1–2 h after impact, and the time of arrival at the central Mexican highlands would most probably be similar (Sanford et al., 2016). The reflections of the tsunami waves that came from the west, across the Mexican paleoshelf, most likely took hours to arrive again at the impact site (Fig. 16E; Gulick et al., 2019). Hence, these reflected turbid tsunami waves are interpreted to have re-entered the Chicxulub impact basin within 24 h after impact (Gulick et al., 2019), which gives a vital upper time constraint for the deposition of the entire M0077A suevite succession.

This tsunami event at the end of the deposition of the M0077A suevite sequence results in a slight increase in the energy of the sedimentary system before resuspension and slow settling take over and the ~75-cm-thick transitional unit (Lowery et al., 2018; Bralower et al., 2020; Whalen et al., 2020) is deposited (Figs. 16F and S5). The transitional unit (Unit 1G) is capped by a 3-cm-thick green marlstone (basal part of Unit 1F) that shows an unequivocal positive iridium anomaly (~1.0 ppb Ir; Goderis et al., 2021), which is similar to Ir values found at other proximal K-Pg boundary sites around the Gulf of Mexico (Smit, 1999). This Ir anomaly is interpreted to represent the final atmospheric settling of ultrafine meteoritic matter and, based on e.g., atmospheric modelling, this deposition is estimated to have happened <20 years after the Chicxulub impact (Figs. 1C and 16F) (Goderis et al., 2021). This peak in Ir concentration captures the cessation of deposition of the complete proximal impactite sequence in the M0077A core, which, in general, shows a decreasing trend in energy level of the peak-ring sedimentary system in the aftermath of the Chicxulub impact.

In summary, the presence of isolated planktic foraminifera in the clastic groundmass of the entire 98.3-m-thick M0077A suevite sequence suggests an important influence of marine depositional processes throughout the complete buildup of the succession (Figs. 16C–16F). The non-graded suevite and bedded suevite units are clearly enriched in isolated foraminifera compared to the graded suevite unit, and they also have a distinct geochemical composition and seismic velocity signal (Fig. 14). The non-graded suevite and bedded suevite units indicate therefore better cementation and emplacement by different impact-triggered marine processes compared to the graded suevite unit. Hence, we interpret that the suevite sequence in M0077A is composed of a basal, 5.6-m-thick hyaloclastite deposit (non-graded suevite unit) that was generated from the interaction of seawater with hot impact melt and followed by an 89.2-m-thick, fining-upward succession (graded suevite unit) deposited by means of a powerful debris-loaded ocean resurge inside the peak ring region in the following hours. The top 3.5 m of the suevite (bedded suevite unit) is composed of reworked material as a consequence of oscillating seiche waves. The final 20 cm of this suevite sequence represents a slight energy increase caused by the return of tsunami waves reflected within the Gulf of Mexico (Smit et al., 1996), which indicates that the entire suevite sequence most probably was deposited within a day after impact (Gulick et al., 2019).

CONCLUSIONS

The continuous suevite sequence from the IODP-ICDP Expedition 364 Hole M0077A, encountered between 715.60 mbsf and 617.33 mbsf depth, provides unique insights into impact cratering processes that were responsible for the melting, brecciation, and subsequent deposition of more or less shocked target lithologies under marine conditions. Based on an extensive petrographic, geochemical, and sedimentological data set, we subdivide this almost 100-m-thick sequence into three distinct units that can be linked to specific emplacement mechanisms that took place in the first hours to a day after the Chicxulub impact. The identification of isolated Cretaceous planktic foraminifera within the groundmass of all these three units indicates that marine processes were involved in the deposition of the entire M0077A suevite sequence. The secluded position of Site M0077 on a small depression on the northern Chicxulub peak ring, with access to the open ocean from a gap in the N-NE inner rim, enabled the preservation of an exceptional record of marine cratering processes: from the initial seawater ingress after the impact to a powerful debris-laden ocean resurge that transitioned into oscillating seiche wave activity.

In contrast to a previous subdivision of the M0077A core that placed the boundary between impact melt rock and suevite at 721.62 mbsf, the first suevite is observed at ~715.6 mbsf. The interval between these two depths (721.62–715.60 mbsf) is deduced here as a brecciated impact melt rock that displays more green, sparry calcite schlieren toward the top. The overlying 5.6-m-thick, non-graded suevite unit has higher bulk CaO values (~40 wt%) compared to the unit below and is characterized by a poorly sorted, clastic groundmass that yields abundant isolated, partly recrystallized planktic (and not benthic) foraminifera and predominantly impact melt particles (both vitric and microcrystalline) as well as carbonate clasts (primary and reacted). This poorly sorted unit also yields a paleomagnetic signal that is consistent with the impact melt rock below and therefore resembles a hyaloclastite breccia deposit formed within the first 30 min after impact due to the rapid return of ocean water depleted in rock debris. Although this unit was subjected to heating from the melt substrate below, which caused melt-water (phreatomagmatic) interactions, it was also rapidly cooled by seawater from above, which resulted in an exposure to high temperatures that was short enough to preserve foraminiferal textures.

The boundary with the overlying graded suevite unit (at ~710 mbsf) is sharp and corresponds to the arrival of a powerful resurge of debris-laden ocean water inside the Chicxulub crater. This caused the cessation of hyaloclastite and phreatomagmatic processes and initiated the buildup of a large 89-m-thick, graded, fining-upward and increasingly well-sorted suevite sequence that was deposited within hours after impact. The more clast-supported nature and high porosity of the basal part of the graded suevite unit suggest poor cementation and support the rapid deposition of this unit. The target rock clast population of this unit is diverse and ranges from both felsic basement clasts (granitoid and gneiss) and mafic basement clasts (rare dolerite and amphibolite) to silica mineral clasts, carbonate clasts, and impact melt clasts. The bulk major and trace element geochemistry is relatively similar throughout this thick unit with, on average, lower CaO values (~20 wt%) and

Downloaded from http://pubs.geoscienceworld.org/gsa/gsabulletin/article-pdf/doi/10.1130/B36020.1/5365526/b36020.pdf
by Arizona State University user

more enriched rare earth element patterns than the other two suevite units.

The boundary with the 3.5-m-thick bedded suevite unit (at ~621 mbsf) is relatively sharp and is emphasized by a horizontally bedded and imbricated nature in contrast to the suevite below that lacks imbrication of components. This observation coincides with an increase in bulk density and CaO content (~40 wt%), abundant well-preserved planktic and benthic foraminifera, and the identification of a large impact spherule embedded in the groundmass of this unit. These characteristics suggest slower deposition, reworking, settling, and cementation steered by seiche movements after the resurge into the crater ended. The upper part of this seiche succession is characterized by cross-beds and the presence of terrestrial biomarkers, which are indicative of the return of a reflected tsunami within 24 h after impact and therefore a slight increase in energy (Gulick et al., 2019). The bedded suevite unit is capped by the 75-cm-thick transitional unit dominated by micrite and claystone depleted in melt particles. The top part of this unit is characterized by an iridium-rich layer that is indicative of atmospheric fallout containing the final ultrafine meteoritic matter, which was deposited within ~20 years after the impact (Goderis et al., 2021). Cumulatively, the M0077A suevite sequence from the Chicxulub impact site preserved a high-resolution record that provides an unprecedented window for unravelling the dynamics and timing of proximal marine cratering processes in the direct aftermath of a large impact event.

ACKNOWLEDGMENTS

We appreciate the constructive reviews from David King and Ralf Thomas Schmitt that have strengthened this manuscript. We also thank associate editor Wolf Uwe Reimold for his review and editorial handling. This research is financially supported by the Belgian Federal Science Policy (BELSPO) Project Chicxulub and the Research Foundation–Flanders (FWO) Project G0A6517N. Pim Kaskes thanks FWO for the awarded Ph.D. fellowship (Project 11E6619N, 11E6621N), and Philippe Claeys thanks the FWO–Hercules Program for financing the μXRF instrument at the Vrije Universiteit Brussel, Belgium. Steven Goderis, Vinciane Debaille, Nadine Matielli, and Philippe Claeys thank the Excellence of Science Project “ET-HoME” for support. Vinciane Debaille also thanks FRS-FNRS for support. We are grateful to Quinten van Gaever (Ghent University), Sander op de Beeck (Katholieke Universiteit Leuven), and Ruben Vandijck (Katholieke Universiteit Leuven) for petrographic, μXRF, and bulk geochemical analysis as part of their Masters’ theses. Robin Francotte (Vrije Universiteit Brussel) is thanked for processing of μXRF maps of thin sections. Wendy Debouge and Sabrina Cauchies (both Université Libre de Bruxelles) are thanked for their assistance with sample preparation and analytical procedures for bulk ICP-OES and ICP-MS analysis at Laboratoire G-Time, Université Libre de Bruxelles. We thank Priya Laha (Vrije Universiteit Brussel, Belgium) and Dan Topa (Natural History Museum, Vienna) for access to and assistance with scanning electron microscope and microprobe analyses. Partial funding in Vienna was provided by the University of Vienna doctoral school IK-1045 (P.I.: Christian Koeberl). We also thank Peter Nagl and Dieter Mader (both at University of Vienna) for help with bulk XRF and INAA work, respectively. Axel Wittmann received funding from National Science Foundation grant OCE-1737087. This research used samples and data provided by International Ocean Discovery Program Expedition 364, which was jointly funded by the European Consortium for Ocean Research Drilling and International Continental Scientific Drilling Program, with contributions and logistical support from the Yucatán State Government and National Autonomous University of Mexico. This is University of Texas Institute for Geophysics Contribution #3781 and Center of Planetary Systems Habitability #0029.

REFERENCES CITED

Alegret, L., and Thomas, E., 2001, Upper Cretaceous and lower Paleogene benthic foraminifera from northeastern Mexico: Micropaleontology, v. 47, no. 4, p. 269–316, https://doi.org/10.2113/47.4.269.

Alvarez, L.W., Alvarez, W., Asaro, F., and Michel, H.V., 1980, Extraterrestrial cause for the Cretaceous-Tertiary extinction: Science, v. 208, p. 1095–1108, https://doi.org/10.1126/science.208.4448.1095.

Artemieva, N.A., Wünnemann, K., Krien, F., Reimold, W.U., and Stöffler, D., 2013, Ries crater and suevite revisited—Observations and modeling Part II: Modeling: Meteoritics & Planetary Science, v. 48, p. 590–627, https://doi.org/10.1111/maps.12085.

Artemieva, N., and Morgan, J., 2017, Quantifying the release of climate-active gases by large meteorite impacts with a case study of Chicxulub: Geophysical Research Letters, v. 44, p. 10,180–10,188, https://doi.org/10.1002/2017GL074879.

Belza, J., Goderis, S., Keppens, E., Vanhaecke, F., and Claeys, P., 2012, An emplacement mechanism for the mega-block zone within the Chicxulub crater, (Yucatán, Mexico) based on chemostratigraphy: Meteoritics & Planetary Science, v. 47, p. 400–413, https://doi.org/10.1111/j.1945-5100.2012.01345.x.

Belza, J., Goderis, S., Smit, J., Vanhaecke, F., Baert, K., Terryn, H., and Claeys, P., 2015, High spatial resolution geochemistry and textural characteristics of “microtektite” glass spherules in proximal Cretaceous-Paleogene sections: Insights into glass alteration patterns and precursor melt lithologies: Geochimica et Cosmochimica Acta, v. 152, p. 1–38, https://doi.org/10.1016/j.gca.2014.12.013.

Bralower, T.J., Cosmidis, J., Fantle, M.S., Lowery, C.M., Passey, B.H., Gulick, S.P.S., Morgan, J.V., Vajda, V., Whalen, M.T., Wittmann, A., Artemieva, N., Farley, K., Goderis, S., Hajek, E., Heaney, P.J., Kring, D.A., Lyons, S.L., Rasmussen, C., Sibert, E., Rodríguez Tovar, F.J., Turner-Walker, G., Zachos, J.C., Carte, J., Chen, S.A., Cockell, C., Coolen, M., Freeman, K.H., Garber, J., Gonzalez, M., Gray, J.L., Grice, K., Jones, H.L., Schaefer, B., Smit, J., and Tikoo, S.M., 2020, The habitat of the nascent Chicxulub crater: AGU Advances, v. 1, p. 1–27, https://doi.org/10.1029/2020av000208.

Chanou, A., Osinski, G.R., and Grieve, R.A.F., 2014, A methodology for the semi-automatic digital image analysis of fragmental impactites: Meteoritics & Planetary Science, v. 49, p. 621–635, https://doi.org/10.1111/maps.12267.

Christeson, G.L., Gulick, S.P.S., Morgan, J.V., Gebhardt, C., Kring, D.A., Le Ber, E., Lofi, J., Nixon, C., Poelchau, M., Rae, A.S.P., Rebolledo-Vieyra, M., Riller, U., Schmitt, D.R., Wittmann, A., Bralower, T.J., Chenot, E., Claeys, P., Cockell, C.S., Coolen, M.J.L., Ferrière, L., Green, S., Goto, K., Jones, H., Lowery, C.M., Mellett, C., Ocampo-Torres, R., Perez-Cruz, L., Pickersgill, A.E., Rasmussen, C., Sato, H., Smit, J., Tikoo, S.M., Tomioka, N., Urrutia-Fucugauchi, J., Whalen, M.T., Xiao, L., and Yamaguchi, K.E., 2018, Extraordinary rocks from the peak ring of the Chicxulub impact crater: P-wave velocity, density, and porosity measurements from IODP/ICDP Expedition 364: Earth and Planetary Science Letters, v. 495, p. 1–11, https://doi.org/10.1016/j.epsl.2018.05.013.

Claeys, P., 2006, Chicxulub, anatomy of a large impact structure: From impactite to ejecta distribution, *in* Proceedings of the 40th ESLAB Symposium “First International Conference on Impact Cratering in the Solar System”: Noordwijk, The Netherlands, European Space Agency, European Space and Technology Centre, p. 81–92.

Claeys, P., Heuschkel, S., Lounejeva-Baturina, E., Sanchez-Rubio, G., and Stöffler, D., 2003, The suevite of drill hole Yucatàn 6 in the Chicxulub impact crater: Meteoritics & Planetary Science, v. 38, p. 1299–1317, https://doi.org/10.1111/j.1945-5100.2003.tb00315.x.

Collins, G.S., Patel, N., Davison, T.M., Rae, A.S.P., Morgan, J.V., Gulick, S.P.S., and Expedition, I.O.D.P.-I.C.D.P., 364 Science Party, and Third-Party Scientists, 2020, A steeply-inclined trajectory for the Chicxulub impact: Nature Communications, v. 11, p. 1–10, https://doi.org/10.1038/s41467-020-15269-x.

de Graaff, S.J., Kaskes, P., Déhais, T., Goderis, S., Debaille, V., Ross, C.H., Gulick, S.P.S., Feignon, J.-G., Ferrière, L., Koeberl, C., Smit, J., Matielli, N., and Claeys, P., 2021, New insights into the formation and emplacement of impact melt rocks within the Chicxulub impact structure, following the 2016 IODP-ICDP Expedition 364: Geological Society of America Bulletin, https://doi.org/10.1130/B35795.1.

de Winter, N.J., and Claeys, P., 2017, Micro X-ray fluorescence (μXRF) line scanning on Cretaceous rudist bivalves: A new method for reproducible trace element profiles in bivalve calcite: Sedimentology, v. 64, p. 231–251, https://doi.org/10.1111/sed.12299.

Dressler, B.O., Sharpton, V.L., Morgan, J., Buffler, R., Moran, D., Smit, J., Stöffler, D., and Urrutia-Fucugauchi, J., 2003, Investigating a 65-Ma-old smoking gun: Deep drilling of the Chicxulub impact structure: Eos (Transactions, American Geophysical Union), v. 84, https://doi.org/10.1029/2003EO140001.

Dressler, B.O., Sharpton, V.L., Schwandt, C.S., and Ames, D., 2004, Impactites of the Yaxcopoil-1 drilling site, Chicxulub impact structure: Petrography, geochemistry, and depositional environment: Meteoritics & Planetary Science, v. 39, p. 857–878, https://doi.org/10.1111/j.1945-5100.2004.tb00935.x.

Dunham, R.J., 1962, Classification of carbonate rocks according to depositional textures, *in* Ham, W.E. ed., Classification of Carbonate Rocks—A Symposium: Tulsa, Oklahoma, Memoir of the American Association of Petroleum Geologists, v. 1, p. 108–121.

Dypvik, H., Gohn, G.S., Edwards, L.E., Horton, J.W., Jr., Powars, D.S., and Litwin, R.J., 2018, Chesapeake Bay impact structure—Development of “brim” sedimentation in a multilayered marine target: Geological Society of America Special Paper 537, p. 1–68, https://doi.org/10.1130/SPE537.

Edwards, L.E., Powars, D.S., Gohn, G.S., and Dypvik, H., 2009, Chapter 3, Geologic columns for the ICDP-USGS Eyreville A and B cores, Chesapeake Bay impact structure: Sediment-clast breccias, 1096 to 444 m depth, *in* Gohn, G.S., Koeberl, C., Miller, K.G., and Reimold, W.U., eds., The ICDP-USGS Deep Drilling Project in the Chesapeake Bay Impact Structure: Results from the Eyreville Core Holes: Geological Society of America Special Paper 458, https://doi.org/10.1130/2009.2458(03).

Engelhardt, W.V., Arndt, J., Fecker, B., and Pankau, H.G., 1995, Suevite breccia from the Ries crater, Germany: Origin, cooling history and devitrification of impact glasses: Meteoritics & Planetary Science, v. 30, p. 279–293, https://doi.org/10.1111/j.1945-5100.1995.tb01126.x.

Feignon, J.-G., Ferrière, L., Leroux, H., and Koeberl, C., 2020, Characterization of shocked quartz grains from Chicxulub peak ring granites and shock pressure estimates: Meteoritics & Planetary Science, v. 55, p. 2206–2223, https://doi.org/10.1111/maps.13570.

Ferrière, L., Koeberl, C., and Reimold, W.U., 2009a, Characterisation of ballen quartz and cristobalite in

Downloaded from http://pubs.geoscienceworld.org/gsa/gsabulletin/article-pdf/doi/10.1130/B36020.1/5365526/b36020.pdf
by Arizona State University user

impact breccias: New observations and constraints on ballen formation: European Journal of Mineralogy, v. 21, p. 203–217, https://doi.org/10.1127/0935-1221/2009/0021-1898.

Ferrière, L., Koeberl, C., Reimold, W.U., Hecht, L., and Bartosova, K., 2009b, The origin of "toasted" quartz in impactites revisited: Houston, Texas, Lunar and Planetary Institute, Fortieth Lunar and Planetary Science Conference, abstract 1751.

French, B.M., 1998, Traces of Catastrophe: A Handbook of Shock-Metamorphic Effects in Terrestrial Meteorite Impact Structures: Houston, Texas, Lunar and Planetary Institute, Lunar and Planetary Institute Contribution no. 954, 120 p.

Goderis, S., Tagle, R., Belza, J., Smit, J., Montanari, A., Vanhaecke, F., Erzinger, J., and Claeys, P., 2013, Reevaluation of siderophile element abundances and ratios across the Cretaceous-Paleogene (K-Pg) boundary: Implications for the nature of the projectile: Geochimica et Cosmochimica Acta, v. 120, p. 417–446, https://doi.org/10.1016/j.gca.2013.06.010.

Goderis, S., Soens, B., Huber, M.S., McKibbin, S., van Ginneken, M., Van Maldeghem, F., Debaille, V., Greenwood, R.C., Franchi, I.A., Cnudde, V., Van Malderen, S., Vanhaecke, F., Koeberl, C., Topa, D., and Claeys, P., 2020, Cosmic spherules from Widerøefjellet, Sør Rondane Mountains (East Antarctica): Geochimica et Cosmochimica Acta, v. 270, p. 112–143, https://doi.org/10.1016/j.gca.2019.11.016.

Goderis, S., Sato, H., Ferrière, L., Schmitz, B., Burney, D., Kaskes, P., Vellekoop, J., Wittmann, A., Schulz, T., Chernonozhkin, S.M., Claeys, P., de Graaff, S.J., Déhais, T., de Winter, N.J., Elfman, M., Feignon, J-G., Ishikawa, A., Koeberl, C., Kristiansson, P., Neal, C.R., Owens, J.D., Schmieder, M., Sinnesael, M., Vanhaecke, F., Van Malderen, S.J.M., Bralower, T.J., Gulick, S.P.S., Kring, D.A., Lowery, C.M., Morgan, J.V., Smit, J., Whalen, M.T., and IODP-ICDP Expedition 364 Scientists, 2021, Globally distributed iridium layer preserved within the Chicxulub impact structure: Science Advances, v. 7, no. 9, article no. eabe3647, https://doi.org/10.1126/sciadv.abe3647.

Gohn, G.S., Koeberl, C., Miller, K.G., Reimold, W.U., Browning, J.V., Cockell, C.S., Horton, J.W., Kenkmann, T., Kulpecz, A.A., Powars, D.S., and Sanford, W.E., 2008, Deep drilling into the Chesapeake Bay impact structure: Science, v. 320, p. 1740–1745, https://doi.org/10.1126/science.1158708.

Goto, K., Tada, R., Tajika, E., Bralower, T.J., Hasegawa, T., and Matsui, T., 2004, Evidence for ocean water invasion into the Chicxulub crater at the Cretaceous/Tertiary boundary: Meteoritics & Planetary Science, v. 39, p. 1233–1247, https://doi.org/10.1111/j.1945-5100.2004.tb01139.x.

Graup, G., 1981, Terrestrial chondrules, glass spherules and accretionary lapilli from the suevite, Ries Crater, Germany: Earth and Planetary Science Letters, v. 55, p. 407–418, https://doi.org/10.1016/0012-821X(81)90168-0.

Greenfield, L., Millett, J.M., Howell, J., Jerram, D.A., Watton, T., Healy, D., Hole, M.J., and Planke, S., 2020, The 3D facies architecture and petrophysical properties of hyaloclastite delta deposits: An integrated photogrammetry and petrophysical study from southern Iceland: Basin Research, v. 32, p. 1081–1104, https://doi.org/10.1111/bre.12415.

Grieve, R.A.F., Ames, D.E., Morgan, J.V., and Artemieva, N., 2010, The evolution of the Onaping Formation at the Sudbury impact structure: Meteoritics & Planetary Science, v. 45, p. 759–782, https://doi.org/10.1111/j.1945-5100.2010.01057.x.

Gulick, S.P.S., Barton, P.J., Christeson, G.L., Morgan, J.V., McDonald, M., Mendoza-Cervantes, K., Pearson, Z.F., Surendra, A., Urrutia-Fucugauchi, J., Vermeesch, P.M., and Warner, M.R., 2008, Importance of pre-impact crustal structure for the asymmetry of the Chicxulub impact crater: Nature Geoscience, v. 1, p. 131–135, https://doi.org/10.1038/ngeo103.

Gulick, S.P.S., Morgan, J., Mellett, C.L., Green, S.L., Bralower, T., Chenot, E., Christeson, G., Claeys, P., Cockell, C., Coolen, M.J.L., Ferrière, L., Gebhardt, C., Goto, K., Jones, H., Kring, D., Lofi, J., Lowery, C., Ocampo-Torres, R., Perez-Cruz, L., Pickersgill, A.E., Poelchau, M., Rae, A., Rasmussen, C., Rebolledo-Vieyra, M., Riller, U., Sato, H., Smit, J., Tikoo, S., Tomioka, N., Urrutia-Fucugauchi, J., Whalen, M., Wittmann, A., Yamaguchi, K., Xiao, L., and Zylberman, W., 2017, Site M0077: Upper Peak Ring, *in* Morgan, J., Gulick, S., Mellett, C.L., Green, S.L., and the Expedition 364 Scientists, Chicxulub: Drilling the K-Pg Impact Crater: College Station, Texas, Proceedings of the International Ocean Discovery Program, v. 364, p. 1–23, https://doi.org/10.14379/iodp.proc.364.106.2017.

Gulick, S.P.S., Bralower, T.J., Ormö, J., Hall, B., Grice, K., Schaefer, B., Lyons, S., Freeman, K.H., Morgan, J.V., Artemieva, N., Kaskes, P., de Graaff, S.J., Whalen, M.T., Collins, G.S., Tikoo, S.M., Verhagen, C., Christeson, G.L., Claeys, P., Coolen, M.J.L., Goderis, S., Goto, K., Grieve, R.A.F., McCall, N., Osinski, G.R., Rae, A.S.P., Riller, U., Smit, J., Vajda, V., Wittmann, A., and the Expedition 364 Scientists, 2019, The first day of the Cenozoic: Proceedings of the National Academy of Sciences of the United States of America, v. 116, no. 39, p. 19342–19351, https://doi.org/10.1073/pnas.1909479116.

Haschke, M., 2014, Laboratory micro-X-ray fluorescence spectroscopy: Instrumentation and applications: Springer Series in Surface Sciences, v. 55, p. 1–367, https://doi.org/10.1007/978-3-319-04864-2.

Hildebrand, A.R., Penfield, G.T., Kring, D.A., Pilkington, M., Camargo Z., A., Jacobsen, S.B., and Boynton, W.V., 1991, Chicxulub crater—a possible Cretaceous/Tertiary boundary impact crater on the Yucatan Peninsula, Mexico: Geology, v. 19, p. 867–871, https://doi.org/10.1130/0091-7613(1991)019<0867:CCAPCT>2.3.CO;2.

Hull, P.M., Bornemann, A., Penman, D.E., Henehan, M.J., Norris, R.D., Wilson, P.A., Blum, P., Alegret, L., Batenburg, S.J., Bown, P.R., Bralower, T.J., Cournede, C., Deutsch, A., Donner, B., Friedrich, O., Jehle, S., Kim, H., Kroon, D., Lippert, P.C., Loroch, D., Moebius, I., Moriya, K., Peppe, D.J., Ravizza, G.E., Röhl, U., Schueth, J.D., Sepúlveda, J., Sexton, P.F., Sibert, E.C., Śliwińska, K.K., Summons, R.E., Thomas, E., Westerhold, T., Whiteside, J.H., Yamaguchi, T., and Zachos, J.C., 2020, On impact and volcanism across the Cretaceous-Paleogene boundary: Science, v. 367, p. 266–272, https://doi.org/10.1126/science.aay5055.

Kaskes, P., Déhais, T., de Graaff, S.J., Goderis, S., and Claeys, P., 2021, Micro–X-ray fluorescence (μXRF) analysis of proximal impactites: High-resolution element mapping, digital image analysis, and quantifications, *in* Reimold, W.U., and Koeberl, C., eds., Large Meteorite Impacts and Planetary Evolution VI: Geological Society of America Special Paper 550, p. 171–206, https://doi.org/10.1130/2021.2550(07).

Kenkmann, T., Wittmann, A., and Scherler, D., 2004, Structure and impact indicators of the Cretaceous sequence of the ICDP drill core Yaxcopoil-1, Chicxulub impact crater, Mexico: Meteoritics & Planetary Science, v. 39, p. 1069–1088, https://doi.org/10.1111/j.1945-5100.2004.tb01129.x.

Kettrup, B., and Deutsch, A., 2003, Geochemical variability of the Yucat`an basement: Constraints from crystalline clasts in Chicxulub impactites: Meteoritics & Planetary Science, v. 38, p. 1079–1092, https://doi.org/10.1111/j.1945-5100.2003.tb00299.x.

Koeberl, C., 1993, Chicxulub Crater, Yucatan: Tektites, impact glasses, and the geochemistry of target rocks and breccias: Geology, v. 21, p. 211–214, https://doi.org/10.1130/0091-7613(1993)021<0211:CCYTIG>2.3.CO;2.

Koeberl, C., Brandstätter, F., Glass, B.P., Hecht, L., Mader, D., and Reimold, W.U., 2007, Uppermost impact fallback layer in the Bosumtwi crater (Ghana): Mineralogy, geochemistry, and comparison with Ivory Coast tektites: Meteoritics & Planetary Science, v. 42, p. 709–729, https://doi.org/10.1111/j.1945-5100.2007.tb01069.x.

Kring, D.A., 2005, Hypervelocity collisions into continental crust composed of sediments and an underlying crystalline basement: Comparing the Ries (∼24 km) and Chicxulub (∼180 km) impact craters: Chemie der Erde, v. 65, p. 1–46, https://doi.org/10.1016/j.chemer.2004.10.003.

Kring, D.A., 2007, The Chicxulub impact event and its environmental consequences at the Cretaceous-Tertiary boundary: Palaeogeography, Palaeoclimatology, Palaeoecology, v. 255, p. 4–21, https://doi.org/10.1016/j.palaeo.2007.02.037.

Kring, D.A., Hörz, F., Zurcher, L., and Urrutia Fucugauchi, J., 2004, Impact lithologies and their emplacement in the Chicxulub impact crater: Initial results from the Chicxulub Scientific Drilling Project, Yaxcopoil, Mexico: Meteoritics & Planetary Science, v. 39, p. 879–897, https://doi.org/10.1111/j.1945-5100.2004.tb00936.x.

Kring, D.A., Claeys, P., Gulick, S.P.S., Morgan, J.V., Collins, G.S., and the IODP-ICDP Expedition 364 Science Party, 2017, Chicxulub and the exploration of large peak-ring impact craters through scientific drilling: GSA Today, v. 27, p. 4–8, https://doi.org/10.1130/GSATG352A.1.

Kring, D.A., Tikoo, S.M., Schmieder, M., Riller, U., Rebolledo-Vieyra, M., Simpson, S.L., Osinski, G.R., Gattacceca, J., Wittmann, A., Verhagen, C.M., Cockell, C.S., Coolen, M.J.L., Longstaffe, F.J., Gulick, S.P.S., Morgan, J.V., Bralower, T.J., Chenot, E., Christeson, G.L., Claeys, P., Ferrière, L., Gebhardt, C., Goto, K., Green, S.L., Heather, J., Lofi, J., Lowery, C.M., Ocampo-Torres, R., Perez-Cruz, L., Pickersgill, A.E., Poelchau, M.H., Rae, A.S.P., Rasmussen, C., Sato, H., Smit, J., Tomioka, N., Urrutia-Fucugauchi, J., Whalen, M.T., Xiao, L., and Yamaguchi, K.E., 2020, Probing the hydrothermal system of the Chicxulub impact crater: Science Advances, v. 6, no. 22, article no. eaaz3053, https://doi.org/10.1126/sciadv.aaz3053.

López-Ramos, E., 1975, Geological summary of the Yucatán Peninsula, *in* Nairn, A.E.M., and Stehli, F.G., eds., The Gulf of Mexico and the Caribbean: New York, Plenum Press, p. 257–282, https://doi.org/10.1007/978-1-4684-8535-6_7.

Lowery, C.M., Bralower, T.J., Owens, J.D., Rodríguez-Tovar, F.J., Jones, H., Smit, J., Whalen, M.T., Claeys, P., Farley, K., Gulick, S.P.S., Morgan, J.V., Green, S., Chenot, E., Christeson, G.L., Cockell, C.S., Coolen, M.J.L., Ferrière, L., Gebhardt, C., Goto, K., Kring, D.A., Lofi, J., Ocampo-Torres, R., Perez-Cruz, L., Pickersgill, A.E., Poelchau, M.H., Rae, A.S.P., Rasmussen, C., Rebolledo-Vieyra, M., Riller, U., Sato, H., Tikoo, S.M., Tomioka, N., Urrutia-Fucugauchi, J., Vellekoop, J., Wittmann, A., Xiao, L., Yamaguchi, K.E., and Zylberman, W., 2018, Rapid recovery of life at ground zero of the end-Cretaceous mass extinction: Nature, v. 558, p. 288–291, https://doi.org/10.1038/s41586-018-0163-6.

Mader, D., and Koeberl, C., 2009, Using Instrumental Neutron Activation Analysis for geochemical analyses of terrestrial impact structures: Current analytical procedures at the University of Vienna Geochemistry Activation Analysis Laboratory: Applied Radiation and Isotopes, v. 67, p. 2100–2103, https://doi.org/10.1016/j.apradiso.2009.04.014.

Morgan, J., Gulick, S., Mellett, C.L., Green, S.L., and the Expedition 364 Scientists, 2017, Chicxulub: Drilling the K-Pg impact crater: Proceedings of the International Ocean Discovery Program, v. 364, https://doi.org/10.14379/iodp.proc.364.2017.

Morgan, J.V., Gulick, S.P.S., Bralower, T., Chenot, E., Christeson, G., Claeys, P., Cockell, C., Collins, G.S., Coolen, M.J.L., Ferrière, L., Gebhardt, C., Goto, K., Jones, H., Kring, D.A., Le Ber, E., Lofi, J., Long, X., Lowery, C., Mellett, C., Ocampo-Torres, R., Osinski, G.R., Perez-Cruz, L., Pickersgill, A., Poelchau, M., Rae, A., Rasmussen, C., Rebolledo-Vieyra, M., Riller, U., Sato, H., Schmitt, D.R., Smit, J., Tikoo, S., Tomioka, N., Urrutia-Fucugauchi, J., Whalen, M., Wittmann, A., Yamaguchi, K.E., and Zylberman, W., 2016, The formation of peak rings in large impact craters: Science, v. 354, no. 6314, p. 878–882, https://doi.org/10.1126/science.aah6561.

Nagl, P., and Mader, D., 2019, X-ray fluorescence (XRF) and instrumental neutron activation analysis (INAA) for the geochemical analysis of rocks, presented on in-house control samples: Mitteilungen der Österreichischen Mineralogischen Gesellschaft, v. 165, p. 67.

Németh, K., and Kósik, S., 2020, Review of explosive hydrovolcanism: Geosciences, v. 10, p. 1–27, https://doi.org/10.3390/geosciences10020044.

Nisbet, E.G., Dietrich, V.J., and Esenwein, A., 1979, Routine trace-element determination in silicate minerals and

Downloaded from http://pubs.geoscienceworld.org/gsa/gsabulletin/article-pdf/doi/10.1130/B36020.1/5365526/b36020.pdf
by Arizona State University user

rocks by x-ray fluorescence: Fortschritte der Mineralogie, v. 57, p. 264–279.

Ocampo, A.C., Pope, K.O., and Fischer, A.G., 1996, Ejecta blanket deposits of the Chicxulub crater from Albion Island, Belize, *in* Ryder, G., Fastovsky, D., and Gartner, S. eds., The Cretaceous-Tertiary Event and Other Catastrophes in Earth History: Geological Society of America Special Paper 307, p. 75–88, https://doi.org/10.1130/0-8137-2307-8.75.

Ormö, J., Sturkell, E., and Lindström, M., 2007, Sedimentological analysis of resurge deposits at the Lockne and Tvären craters: Clues to flow dynamics: Meteoritics & Planetary Science, v. 42, p. 1929–1943, https://doi.org/10.1111/j.1945-5100.2007.tb00551.x.

Ormö, J., Sturkell, E., Horton, J.W., Jr., Powars, D.S., and Edwards, L.E., 2009, Comparison of clast frequency and size in the resurge deposits at the Chesapeake Bay impact structure (Eyreville A and Langley cores): Clues to the resurge process, *in* Gohn, G.S., Koeberl, C., Miller, K.G., and Reimold, W.U., eds., The ICDP-USGS Deep Drilling Project in the Chesapeake Bay Impact Structure: Results from the Eyreville Core Holes: Geological Society of America Special Paper 458, p. 617–632, https://doi.org/10.1130/2009.2458(27).

Ormö, J., Gulick, S.P.S., Whalen, M.T., King Jr, D.T., Sturkell, E. and Morgan, J., 2021, Assessing event magnitude and target water depth for marine-target impacts: Ocean resurge deposits in the Chicxulub M0077A drill core compared: Earth and Planetary Science Letters, v. 564, no. 116915, https://doi.org/10.1016/j.epsl.2021.116915.

Ortega-Gutiérrez, F., Elías-Herrera, M., Morán-Zenteno, D.J., Solari, L., Weber, B., and Luna-González, L., 2018, The pre-Mesozoic metamorphic basement of Mexico, 1.5 billion years of crustal evolution: Earth-Science Reviews, v. 183, p. 2–37, https://doi.org/10.1016/j.earscirev.2018.03.006.

Osinski, G.R., Grieve, R.A.F., and Spray, J.G., 2004, The nature of the groundmass of surficial suevite from the Ries impact structure, Germany, and constraints on its origin: Meteoritics & Planetary Science, v. 39, p. 1655–1683, https://doi.org/10.1111/j.1945-5100.2004.tb00065.x.

Osinski, G.R., Grieve, R.A.F., Chanou, A., and Sapers, H.M., 2016, The "suevite" conundrum, Part 1: The Ries suevite and Sudbury Onaping Formation compared: Meteoritics & Planetary Science, v. 51, p. 2316–2333, https://doi.org/10.1111/maps.12728.

Osinski, G.R., Grieve, R.A.F., Hill, P.J.A., Simpson, S.L., Cockell, C., Christeson, G.L., Ebert, M., Gulick, S., Melosh, H.J., Riller, U., Tikoo, S.M., and Wittmann, A., 2020, Explosive interaction of impact melt and seawater following the Chicxulub impact event: Geology, v. 48, no. 2, p. 108–112, https://doi.org/10.1130/G46783.1.

Pittarello, L., and Koeberl, C., 2013, Clast size distribution and quantitative petrography of shocked and unshocked rocks from the El'gygytgyn impact structure: Meteoritics & Planetary Science, v. 48, p. 1325–1338, https://doi.org/10.1111/maps.12070.

Pohl, J., Stöffler, D., Gall, H., and Ernstson, K., 1977, The Ries impact crater, *in* Roddy, D.J., Pepin, R.O., and Merrill, R.B. eds., Impact and Explosion Cratering: New York, Pergamon Press, p. 343–404.

Pope, K.O., Ocampo, A.C., Fischer, A.G., Vega, F.J., Ames, D.E., King, D.T., Jr., Fouke, B.W., Wachtman, R.J., and Kletetschka, G., 2005, Chicxulub impact ejecta deposits in southern Quintana Roo, México, and central Belize, *in* Kenkmann, T., Hörz, F., and Deutsch, A., eds., Large Meteorite Impacts III: Geological Society of America Special Paper 384, p. 171–190, https://doi.org/10.1130/0-8137-2384-1.171.

Quitté, G., Robin, E., Levasseur, S., Capmas, F., Rocchia, R., Birck, J.-L., and Allègre, C.J., 2007, Osmium, tungsten, and chromium isotopes in sediments and in Ni-rich spinel at the K-T boundary: Signature of a chondritic impactor: Meteoritics & Planetary Science, v. 42, p. 1567–1580, https://doi.org/10.1111/j.1945-5100.2007.tb00591.x.

Rae, A.S.P., Collins, G.S., Poelchau, M., Riller, U., Davison, T.M., Grieve, R.A.F., Osinski, G.R., Morgan, J.V., and IODP-ICDP Expedition 364 Scientists, 2019, Stress-strain evolution during peak-ring formation: A case study of the Chicxulub impact structure: Journal of Geophysical Research: Planets, v. 124, p. 396–417, https://doi.org/10.1029/2018JE005821.

Rebolledo-Vieyra, M., Urrutia-Fucugauchi, J., Marín, L.E., Trejo-García, A., Sharpton, V.L., and Soler-Arechalde, A.M., 2000, UNAM scientific shallow-drilling program of the Chicxulub impact crater: International Geology Review, v. 42, p. 928–940, https://doi.org/10.1080/00206810009465118.

Rebolledo-Vieyra, M., and Urrutia-Fucugauchi, J., 2004, Magnetostratigraphy of the impact breccias and post-impact carbonates from borehole Yaxcopoil-1, Chicxulub impact crater, Yucatán, Mexico: Meteoritics & Planetary Science, v. 39, p. 821–829, https://doi.org/10.1111/j.1945-5100.2004.tb00932.x.

Reimold, W.U., Bartosova, K., Schmitt, R.T., Hansen, B., Crasselt, C., Koeberl, C., Wittmann, A., and Powars, D.S., 2009, Petrographic observations on the Exmore breccia, ICDP-USGS Drilling at Eyreville, Chesapeake Bay impact structure, USA, *in* Gohn, G.S., Koeberl, C., Miller, K.G., and Reimold, W.U., eds., The ICDP-USGS Deep Drilling Project in the Chesapeake Bay Impact Structure: Results from the Eyreville Core Holes: Geological Society of America Special Paper 458, https://doi.org/10.1130/2009.2458(29).

Reimold, W.U., Hansen, B.K., Jacob, J., Artemieva, N.A., Wünnemann, K., and Meyer, C., 2012, Petrography of the impact breccias of the Enkingen (SUBO 18) drill core, southern Ries crater, Germany: New estimate of impact melt volume: Bulletin of the Geological Society of America, v. 124, p. 104–132, https://doi.org/10.1130/B30470.1.

Renne, P.R., Deino, A.L., Hilgen, F.J., Kuiper, K.F., Mark, D.F., Mitchell, W.S., Morgan, L.E., Mundil, R., and Smit, J., 2013, Time scales of critical events around the Cretaceous-Paleogene boundary: Science, v. 339, p. 684–687, https://doi.org/10.1126/science.1230492.

Riller, U., Poelchau, M.H., Rae, A.S.P., Schulte, F.M., Collins, G.S., Melosh, H.J., Grieve, R.A.F., Morgan, J.V., Gulick, S.P.S., Lofi, J., Diaw, A., McCall, N., Kring, D.A., and IODP–ICDP Expedition 364 Science Party, 2018, Rock fluidization during peak-ring formation of large impact structures: Nature, v. 562, p. 511–518, https://doi.org/10.1038/s41586-018-0607-z.

Sanford, J.C., Snedden, J.W., and Gulick, S.P.S., 2016, The Cretaceous-Paleogene boundary deposit in the Gulf of Mexico: Large-scale oceanic basin response to the Chicxulub impact: Journal of Geophysical Research: Solid Earth, v. 121, p. 1240–1261, https://doi.org/10.1002/2015JB012615.

Schmitt, R.T., Bartosova, K., Reimold, W.U., Mader, D., Wittmann, A., Koeberl, C., and Gibson, R.L., 2009, Geochemistry of impactites and crystalline basement-derived lithologies from the ICDP-USGS Eyreville A and B drill cores, Chesapeake Bay impact structure, Virginia, USA, *in* Gohn, G.S., Koeberl, C., Miller, K.G., and Reimold, W.U., eds., The ICDP-USGS Deep Drilling Project in the Chesapeake Bay Impact Structure: Results from the Eyreville Core Holes: Geological Society of America Special Paper 458, https://doi.org/10.1130/2009.2458(22).

Schulte, P., Alegret, L., Arenillas, I., Arz, J.A., Barton, P.J., Bown, P.R., Bralower, T.J., Christeson, G.L., Claeys, P., Cockell, C.S., Collins, G.S., Deutsch, A., Goldin, T.J., Goto, K., Grajales-Nishimura, J.M., Grieve, R.A.F., Gulick, S.P.S., Johnson, K.R., Kiessling, W., Koeberl, C, Kring, D.A., MacLeod, K.G., Takafumi, M., Melosh, J., Montanari, A., Morgan, J.V., Neal, C.R., Nichols, D.J., Norris, R.D., Pierazzo, E., Ravizza, G., Rebolledo-Vieyra, M., Reimold, W.U., Robin, E., Salge, T., Speijer, R.P., Sweet, A.R., Urrutia-Fucugauchi, J., Vajda, V., Whalen, M.T., and Willumsen, P.S., 2010, The Chicxulub asteroid impact and mass extinction at the Cretaceous-Paleogene boundary: Science, v. 327, no. 5970, p. 1214–1218, https://doi.org/10.1126/science.1177265.

Sharpton, V.L., Marín, L.E., Carney, J.L., Lee, S., Ryder, G., Schuraytz, B.C., Sikora, P., and Spudis, P.D., 1996, A model of the Chicxulub impact basin based on evaluation of geophysical data, well logs, and drill core samples, *in* Ryder, G., Fastovsky, D., and Gartner, S. eds., The Cretaceous-Tertiary Event and Other Catastrophes in Earth History: Geological Society of America Special Paper 307, p. 55–74, https://doi.org/10.1130/0-8137-2307-8.55.

Sherman, J., 1955, The theoretical derivation of fluorescent X-ray intensities from mixtures: Spectrochimica Acta, v. 7, p. 283–306, https://doi.org/10.1016/0371-1951(55)80041-0.

Shukolyukov, A., and Lugmair, G.W., 1998, Isotopic evidence for the Cretaceous-Tertiary impactor and its type: Science, v. 282, p. 927–929, https://doi.org/10.1126/science.282.5390.927.

Simpson, S.L., Osinski, G.R., Longstaffe, F.J., Schmieder, M., and Kring, D.A., 2020, Hydrothermal alteration associated with the Chicxulub impact crater upper peak-ring breccias: Earth and Planetary Science Letters, v. 547, no. 116425, https://doi.org/10.1016/j.epsl.2020.116425.

Smit, J., 1982, Extinction and evolution of planktonic foraminifera at the Cretaceous/Tertiary boundary after a major impact, *in* Silver, L.T., and Schultz, P.H., eds., Geological Implications of Impacts of Large Asteroids and Comets on the Earth: Geological Society of America Special Paper 190, p. 329–352, https://doi.org/10.1130/SPE190-p329.

Smit, J., 1999, The global stratigraphy of the Cretaceous-Tertiary boundary impact ejecta: Annual Review of Earth and Planetary Sciences, v. 27, p. 75–113, https://doi.org/10.1146/annurev.earth.27.1.75.

Smit, J., and Hertogen, J., 1980, An extraterrestrial event at the Cretaceous-Tertiary boundary: Nature, v. 285, p. 198–200, https://doi.org/10.1038/285198a0.

Smit, J., Roep, T.B., Alvarez, W., Montanari, A., Claeys, P., Grajales-Nishimura, J.M., and Bermudez, J., 1996, Coarse-grained, clastic sandstone complex at the K/T boundary around the Gulf of Mexico: Deposition by tsunami waves induced by the Chicxulub impact?, *in* Ryder, G., Fastovsky, D., and Gartner., S. eds., The Cretaceous-Tertiary Event and Other Catastrophes in Earth History: Geological Society of America Special Paper 307, p. 151–182, https://doi.org/10.1130/0-8137-2307-8.151.

Stöffler, D., 1977, Research drilling Nördlingen 1973: Polymict breccias, crater basement, and cratering model of the Ries impact structure: Geologica Bavaria, v. 75, p. 443–458.

Stöffler, D., Artemieva, N.A., Ivanov, B.A., Hecht, L., Kenkmann, T., Schmitt, R.T., Tagle, R.A., and Wittmann, A., 2004, Origin and emplacement of the impact formations at Chicxulub, Mexico, as revealed by the ICDP deep drilling at Yaxcopoil-1 and by numerical modeling: Meteoritics & Planetary Science, v. 39, p. 1035–1067, https://doi.org/10.1111/j.1945-5100.2004.tb01128.x.

Stöffler, D., and Grieve, R.A.F., 2007, Impactites, *in* Fettes, D., and Desmons, J., eds., Metamorphic Rocks: A Classification and Glossary of Terms, Recommendations of the International Union of Geological Sciences: Cambridge, UK, Cambridge University Press, p. 82–92, p. 111–125, and p. 126–242.

Stöffler, D., Artemieva, N.A., Wünnemann, K., Reimold, W.U., Jacob, J., Hansen, B.K., and Summerson, I.A.T., 2013, Ries crater and suevite revisited—Observations and modeling Part I: Observations: Meteoritics & Planetary Science, v. 48, p. 515–589, https://doi.org/10.1111/maps.12086.

Sun, S.S., and McDonough, W.F., 1989, Chemical and isotopic systematics of oceanic basalts: Implications for mantle composition and processes, *in* Saunders, A.N., and Norry, M.J., eds., Magmatism in the Ocean Basins: Geological Society, London, Special Paper 42, p. 313–345, https://doi.org/10.1144/GSL.SP.1989.042.01.19.

Trinquier, A., Birck, J.L., and Allègre, C.J., 2006, The nature of the KT impactor. A ^{54}Cr reappraisal: Earth and Planetary Science Letters, v. 241, p. 780–788, https://doi.org/10.1016/j.epsl.2005.11.006.

Tuchscherer, M.G., Reimold, W.U., Koeberl, C., Gibson, R.L., and de Bruin, D., 2004, First petrographic results on impactites from the Yaxcopoil-1 borehole, Chicxulub structure, Mexico: Meteoritics & Planetary Science, v. 39, p. 899–930, https://doi.org/10.1111/j.1945-5100.2004.tb00937.x.

Downloaded from http://pubs.geoscienceworld.org/gsa/gsabulletin/article-pdf/doi/10.1130/B36020.1/5365526/b36020.pdf
by Arizona State University user

Urrutia-Fucugauchi, J., Marin, L., and Trejo-Garcia, A., 1996, UNAM scientific drilling program of Chicxulub impact structure—Evidence for a 300 kilometer crater diameter: Geophysical Research Letters, v. 23, p. 1565–1568, https://doi.org/10.1029/96GL01566.

Urrutia-Fucugauchi, J., Morgan, J., Stöffler, D., and Claeys, P., 2004, The Chicxulub Scientific Drilling Project (CSDP): Meteoritics & Planetary Science, v. 39, p. 787–790, https://doi.org/10.1111/j.1945-5100.2004.tb00928.x.

Urrutia-Fucugauchi, J., Pérez-Cruz, L., Campos-Arriola, S.E., Escobar-Sánchez, E., and Velasco-Villarreal, M., 2014, Magnetic susceptibility logging of Chicxulub proximal impact breccias in the Santa Elena borehole: Implications for emplacement mode: Studia Geophysica et Geodaetica, v. 58, p. 100–120, https://doi.org/10.1007/s11200-013-0803-0.

Vermeesch, P.M., and Morgan, J.V., 2008, Structural uplift beneath the Chicxulub impact structure: Journal of Geophysical Research: Solid Earth, v. 113, p. 1–10, https://doi.org/10.1029/2007JB005393.

Ward, W.C., Keller, G., Stinnesbeck, W., and Adatte, T., 1995, Yucatan subsurface stratigraphy: Implications and constraints for the Chicxulub impact: Geology, v. 23, p. 873–876, https://doi.org/10.1130/0091-7613(1995)023<0873:YNSSIA>2.3.CO;2.

Watton, T.J., Jerram, D.A., Thordarson, T., and Davies, R.J., 2013, Three-dimensional lithofacies variations in hyaloclastite deposits: Journal of Volcanology and Geothermal Research, v. 250, p. 19–33, https://doi.org/10.1016/j.jvolgeores.2012.10.011.

Whalen, M.T., Gulick, S.P.S., Lowery, C.M., Bralower, T.J., Morgan, J.V., Grice, K., Schaefer, B., Smit, J., Ormö, J., Wittmann, A., Kring, D.A., Lyons, S., Goderis, S., and the Expedition 364 Scientists, 2020, Winding down the Chicxulub impact: The transition between impact and normal marine sedimentation near ground zero: Marine Geology, v. 430, no. 106368, https://doi.org/10.1016/j.margeo.2020.106368.

Whitehead, J., Spray, J.G., and Grieve, R.A.F., 2002, Origin of "toasted" quartz in terrestrial impact structures: Geology, v. 30, p. 431–434, https://doi.org/10.1130/0091-7613(2002)030<0431:OOTQIT>2.0.CO;2.

Whitney, D.L., and Evans, B.W., 2010, Abbreviations for names of rock-forming minerals: The American Mineralogist, v. 95, p. 185–187, https://doi.org/10.2138/am.2010.3371.

Wittmann, A., 2020, Component analysis of sorted suevite in the Chicxulub impact crater: Houston, Texas, Lunar and Planetary Institute, Fifty-First Lunar and Planetary Science Conference, Lunar and Planetary Institute, abstract 2211.

Wittmann, A., Kenkmann, T., Hecht, L., and Stöffler, D., 2007, Reconstruction of the Chicxulub ejecta plume from its deposits in drill core Yaxcopoil-1: Geological Society of America Bulletin, v. 119, p. 1151–1167, https://doi.org/10.1130/B26116.1.

Wittmann, A., Goderis, S., Claeys, P., Vanhaecke, F., Deutsch, A., and Adolph, L., 2013, Petrology of impactites from El'gygytgyn crater: Breccias in ICDP-drill core 1C, glassy impact melt rocks and spherules: Meteoritics & Planetary Science, v. 48, p. 1199–1235, https://doi.org/10.1111/maps.12019.

Wouters, B., Makarona, C., Nys, K., and Claeys, P., 2017, Characterization of archaeological metal remains in micromorphological thin sections using μXRF elemental mapping: Geoarchaeology, v. 32, p. 311–318, https://doi.org/10.1002/gea.21591.

Zhao, J., Xiao, L., Gulick, S.P.S., Morgan, J.V., Kring, D., Urrutia-Fucugauchi, J., Schmieder, M., de Graaff, S.J., Wittmann, A., Ross, C.H., Claeys, P., Pickersgill, A., Kaskes, P., Goderis, S., Rasmussen, C., Vajda, V., Ferrière, L., Feignon, J.-G., Chenot, E., Perez-Cruz, L., Sato, H., Yamaguchi, K., and the IODP–ICDP Expedition 364 scientists, 2020, Geochemistry, geochronology and petrogenesis of Maya Block granitoids and dykes from the Chicxulub Impact Crater, Gulf of México: Implications for the assembly of Pangea: Gondwana Research, v. 82, p. 128–150, https://doi.org/10.1016/j.gr.2019.12.003.

SCIENCE EDITOR: ROB STRACHAN
ASSOCIATE EDITOR: W.U. REIMOLD

MANUSCRIPT RECEIVED 22 DECEMBER 2020
REVISED MANUSCRIPT RECEIVED 21 APRIL 2021
MANUSCRIPT ACCEPTED 17 MAY 2021

Printed in the USA

Downloaded from http://pubs.geoscienceworld.org/gsa/gsabulletin/article-pdf/doi/10.1130/B36020.1/5365526/b36020.pdf
by Arizona State University user